الجمهورية الجزائرية الديمقراطية الشعبية

LA REPUBLIQUE ALGERIENNE DEMOCRATIQUE ET POPULAIRE

وزارة التعليم العالي والبحث العلمي

Ministry of Higher Education and Scientific Research

Saad Dahlab University Blida 1

Institute of Aeronautics and Space Studies

Department of Space Studies

End-of-Study Thesis

In fulfillment of the requirements for the degree of

Master in Aeronautics

Option : Space Propulsion

THEME

Aerodynamics of Over-Expanded Supersonic Nozzles :

Simulation and Experimental Study of Flow Parameters and Side Loads.

Proposed and Supervised by:

Dr. HAMAIDIA Walid

Dr. KHALI El-Hadi

Realized by:

Mr. BAOUCHI Ahmed

Defended before the Jury composed of:

Dr. KBAB Hakim	*MCA*	*President*
Dr. HALIMI Akila	*MCB*	*Examiner*
Dr. HAMAIDIA Walid	*MCA*	*Promoter*
Dr. KHALI El-Hadi	*MCA*	*Co-Promoter*

Promotion : 2024 / 2025

Dedication

I dedicate this work to the cherished memory of our exceptional teacher, Dr. Boukraa Saleh. His profound contributions and remarkable ability to impart knowledge were harmoniously matched by his extraordinary character. He was a truly kind, respectful, and genuinely helpful person, one of the greatest men I have ever known. I sincerely hope this work stands as a testament and tribute to his legacy and his invaluable diligence. May your soul rest in peace.

***

To my family, whose unwavering love and belief in me made this journey possible.

***

This work is dedicated to all individuals and institutions who tirelessly contribute to the advancement and dissemination of knowledge across the globe.

***

"The teacher who walks in the shadow of the temple, among his pupils, gives not of his wisdom but rather of his faith and his lovingness.", Khalil Gibran.

"Develop a passion for learning. If you do, you will never cease to grow.", Anthony J. D'Angelo.

"The only true wisdom is in knowing you know nothing.", Socrates.

ACKNOWLEDGMENTS

اولا وقبل كل شيء, اود ان اشكر الله تعالى الذي يسر لنا هذا العمل واعاننا على اتمامه في اكمل صوره, الحمد لله الذي وفقنا الى ما نحن عليه ورضي لنا هذا, الحمد لله الذي كان وليا و ناصرا لنا في جميع الاوقات, الحمد لله الذي اعطى لنا نعمة العلم والعقل والصحة, الحمد والشكر لله رب العالمين.

The successful completion of this thesis would not have been possible without the invaluable support, guidance, and contributions of numerous individuals and institutions.

First, I extend my deepest gratitude to my supervisors, Professor Hamaidia Walid and Professor Khali Elhadi, for their unwavering mentorship, insightful critiques, and profound patience throughout every stage of this research. Their expertise and dedication were instrumental in shaping the direction and quality of this work. I am also profoundly grateful to my thesis committee members for their constructive feedback, challenging questions, and the time they generously dedicated to reviewing this manuscript.

I would like to express my sincere gratitude to the Higher School of Aeronautical Technics (ESTA), Dar El Beida, Algeria, for their generous welcome and the invaluable support they provided throughout my work. I am deeply thankful for the access to their facilities and the material resources made available to me, which greatly contributed to the success of my project. A special note of appreciation goes to the directors and staff, whose openness, professionalism, and readiness to assist made every interaction straightforward and pleasant. Their collaborative spirit and willingness to facilitate my efforts did not go unnoticed and are genuinely appreciated.

I am especially grateful to the head of the library of our department for its commitment to accessibility and continued assistance. Its efforts in facilitating book acquisition and ensuring convenient use of the library's resources were instrumental in supporting my research.

Finally, I wish to express immense gratitude to my family for their boundless love, unwavering emotional support, and constant encouragement, which sustained me through the demanding periods of this endeavor. Their understanding and belief in me were truly invaluable.

Baouchi Ahmed.
15/06/2025

TABLE OF CONTENTS

LIST OF TABLES

LIST OF FIGURES

Nomenclature

$\dot{m}$: mass flow rate.
ρ : density.
U : Uniform axial velocity.
A : cross-sectional area.
P : Pressure.
h : static enthalpy per unit mass, height.
T : temperature, full stress tensor.
R : gas constant, residuals.
e : internal energy per unit mass.
c_p : specific heat capacity at constant pressure.
c_v : specific heat capacity at constant volume.
s : specific entropy, normalized distance.
q : heat energy per unit mass, heat flux.
c : sound celerity.
M : Mach number.
γ : heat capacities ratio.
F : thrust force.
Isp : specific impulse.
V : speed, volume.
C_T : thrust coefficient.
X : shock position.
η : efficiency.
ε : section area ratio, turbulent dissipation.
t : time.
x, y, z : cartesian space coordinates, distances.
r : radial coordinate component.
M_w : molecular weight.
τ : viscous stress tensor.
δ : boundary layer thickness, Kronecker tensor.
S : strain tensor.
μ : dynamic viscosity.
λ : second viscosity coefficient, thermal conductivity.
μ_v: bulk viscosity.
E : total energy.
Pr : Prandtl number.
k : kinetic turbulent energy.
μ_t : turbulent viscosity.
Re : Reynolds number.
u_τ : frictional velocity.
τ_w : wall shear stress.
l : characteristic length scale.
Ω : rotation tensor.

Subscripts

"o" : stagnation conditions.
" $*$ " : throat conditions.
"$irrev$" : irreversible process.
"rev" : reversible process.
"lim" : limit value.
"s" : isentropic.
"p" : propellant, plateau point.
"e" : exit conditions.
"a" : ambient conditions.
"ad" : adapted conditions.
"eq" : equivalent.
"c" : chamber conditions.
"geo" : geometrical.
"$shock$" : normal shock.
"i" : origin of interaction point.
"s" : separation point, isentropic.
"$char$" : characteristic.
"x, y, z" : spatial partial derivatives.
"t" : turbulent.

Superscripts

"$sonic$" : conditions for a sonic throat and subsonic nozzle flow.
"sup" : supersonic divergent with an exit normal shock wave.

Abbreviations

TEG : Turbine Exhaust Gas Injection.
CDN : Convergent-Divergent Nozzle.
CN : Convergent Nozzle.
NPR : Nozzle Pressure Ratio (P_0/P_e).
MOC : Method of Characteristics.
$SWBLI$: Shock Wave Boundary Layer Interaction.
FSS : Free Shock Separation.
RSS : Restricted Shock Separation.
FIT : Free Interaction Theory.
CFD : Computational Fluid Dynamics.

ABSTRACT

This investigation presents a rigorous experimental, numerical, and analytical study of flow separation and its associated interactions in over-expanded supersonic nozzles. An experimental conical Laval nozzle is used to measure the axial static pressure evolution at various nozzle pressure ratios (NPR). This empirical data is meticulously supplemented by detailed numerical simulations employing three distinct and commonly used turbulence models. Furthermore, the study incorporates an analysis of a typical analytical engineering model and a widely used semi-empirical shock wave boundary layer interaction (SWBLI) criterion.

Key Words: Conical Nozzle, Over-Expanded, Supersonic, Experiment, SWBLI, k-ω, SST k-ω, Spalart-Allmaras, Free Interaction Theory.

Cette investigation présente une étude expérimentale, numérique et analytique rigoureuse du phénomène de séparation d'écoulement et de ses interactions associées dans les tuyères supersoniques sur-détendues. Une tuyère de Laval conique expérimentale est utilisée pour mesurer l'évolution de la pression statique axiale à travers la tuyère à différents rapports de pression de tuyère (NPR). Cette fondation empirique est méticuleusement complétée par des simulations numériques détaillées employant trois modèles de turbulence distincts et couramment utilisés. En outre, l'étude intègre une analyse d'un modèle d'ingénierie analytique typique et d'un critère semi-empirique largement utilisé pour l'interaction onde de choc-couche limite (IOCCL).

Mots-clés : tuyère conique, sur-détendue, supersonique, expérience, IOCCL, k-ω, SST k-ω, Spalart-Allmaras, théorie d’interaction libre.

يقدم هذا البحث دراسة تجريبية، عددية، وتحليلية دقيقة لظاهرة انفصال التدفق وتفاعلاتها المصاحبة ضمن الفوهات الأسرع من الصوت مفرطة التوسع. يتضمن الجانب التجريبي استخدام فوهة لافال ذات تصميم مخروطي، حيث يتم قياس تطور الضغط الساكن المحوري عبر الفوهة عند نسب ضغط مختلفة (NPR). تُستكمل هذه المعطيات التجريبية بدقة من خلال محاكاة عددية تفصيلية تُوظّف ثلاثة نماذج اضطراب متميزة وشائعة الاستخدام. علاوة على ذلك، يتضمن البحث تحليلًا لنموذج هندسي تحليلي تقليدي ومعيار شبه تجريبي واسع الانتشار خاص بتفاعل موجة الصدمة مع الطبقة الحدودية (SWBLI) .

الكلمات المفتاحية: فوهة مخروطية، التمدد الزائد، فوق صوتي، تجربة، SWBLI، k-ω، SST k-ω، Spalart-Allmaras، نظرية التفاعل الحر.

INTRODUCTION

The space sector is a rapidly evolving frontier, encompassing everything from satellite technology and scientific exploration to burgeoning commercial ventures, all pushing the boundaries of human ingenuity and our understanding of the universe. Governments and private companies are collaboratively developing cutting-edge spacecraft and launch systems that facilitate global communication, Earth monitoring, and ambitious missions to distant celestial bodies like Mars, fundamentally shaping the future of interplanetary travel and space-based industries [1].

At the core of this expansion is the relentless pursuit of more efficient and cost-effective space access, which has redefined the very paradigm of space launch systems. The industry is currently witnessing a dramatic shift towards reusability, moving away from the historically expensive and resource-intensive expendable rocket model [1]. This new approach heavily emphasizes cost reduction, increased launch cadence, and enhanced flexibility. While this paradigm prioritizes multi-stage reusable rockets, the long-standing aspiration for Single Stage to Orbit (SSTO) technology remains. SSTO promises ultimate simplicity and aircraft-like operational efficiency by eliminating stage jettison [2]. However, achieving it is profoundly challenging due to the "tyranny of the rocket equation," which demands an exceptionally high propellant mass fraction [2]. This necessitates incredibly lightweight, robust structures, and propulsion systems capable of maintaining high efficiency across vastly different atmospheric and vacuum conditions [2]. Overcoming these hurdles requires revolutionary advancements in materials science, such as high-strength composites and advanced thermal protection, alongside propulsion innovations like altitude-compensating nozzles or complex combined-cycle engines that can seamlessly transition from air-breathing to rocket mode. Despite decades of research, ensuring a viable payload fraction, guaranteeing reliability, and managing complex aerodynamic and thermal loads, both ascent and reentry continue to present formidable engineering obstacles, solidifying the current paradigm's pragmatic reliance on reusable multi-stage designs [1] [2].

Beyond reusability, the commercial viability of space flight is intrinsically linked to the quotient of system performance and system weight, with system costs primarily driven by this ratio. Historically, efforts focused on reducing system weight and pushing the limits of mechanical load capacities. The current aim is to further enhance the thrust-to-weight ratio for rocket nozzles by reducing the divergent length and increasing specific momentum [3].

The optimum thrust on rocket launchers is achieved when the nozzle exit pressure perfectly matches the ambient pressure (an adapted or ideally expanded nozzle). Conversely, Under-Expansion, where exit pressure exceeds ambient pressure, leads to thrust loss due to inefficient gas expansion and suboptimal exit velocity [3].

A more critical challenge arises from Over-Expansion, which occurs when the exit pressure is lower than the ambient pressure. In such cases, the exit flow adapts to the higher ambient pressure through a complex shock-wave system. Critically, if the exit pressure becomes too low, the boundary layer at the nozzle wall can no longer withstand the adverse pressure gradient, leading to nozzle flow separation. The inherent unsteadiness of this flow separation induces significant side loads on the nozzle wall, which can be of dimensioning concern, meaning they dictate the required size and strength, for both the nozzle and the broader rocket structure, including the payload. For sea-level launchers like Ariane 5 and the Space Shuttle, which traverse a wide range of ambient pressures during their ascent, ideally adapting the nozzle's expansion ratio would maximize thrust. However, as such adaptive nozzles are not yet readily available, current designs frequently operate in off-design conditions (under- or over-expanded) for much of their flight [3].

Extensive studies over the years have been dedicated to understanding the complex phenomenon of flow separation in over-expanded rocket nozzles. A deeper comprehension of this behavior could lead to more effective prevention or even active control of flow separation. Furthermore, a reliable separation model is essential for accurately predicting the side-loads experienced during engine start-up and shut-down phases. While Computational Fluid Dynamics (CFD) offers a means to determine separation points and pressure distribution, these calculations are often highly time-consuming, sometimes taking days or even weeks, and their accuracy is significantly influenced by the chosen turbulence model. Given these computational demands, there is a clear desirability for faster predictive methods, thus necessitating the development and use of a semi-empirical model [3].

Compressible flows in supersonic rocket-engine nozzles have been the subject of a considerable amount of experimental and numerical study since the second half of the twentieth century, after the first operational application of the famous German V2 missile in 1943, following the work of the German Werner Von Braun. This research work has continued and intensified until today in specific research laboratories in different countries, a complete review can be found on [4].

Figure 1 : European CRISTAL research group [4].

Objective and Motivation of this Work

The primary objective of this work is to provide a comprehensive insight into the complex phenomenon of flow separation in over-expanded nozzles. We leverage the unique capabilities of the experimental facility at the Laboratory of Aerodynamics and Heat Transfer, Higher School of Aeronautical Technics, Dar El Beida, Algeria, which enables direct observation of this critical flow behavior. Our experimental findings are rigorously complemented by extensive numerical investigations employing a range of widely used turbulence models, along with analytical and semi-empirical separation criteria. This multifaceted approach is designed to elucidate the full impact and various facets of flow separation from multiple perspectives, offering detailed comparisons and revealing intrinsic characteristics.

The significance of this research extends well beyond its direct application to supersonic nozzles, holding profound relevance for a broad spectrum of supersonic flow applications. These include but are not limited to, the design of supersonic diffusers and air intakes for advanced propulsion systems such as ramjets and scramjets, the aerodynamic optimization of transonic blades in jet engine compressors and turbines, and the fundamental understanding of external supersonic aerodynamics around flight bodies. Consequently, this work holds considerable importance and makes a meaningful contribution to the advancement of aerospace engineering.

CHAPTER 1. INSIGHT INTO SUPERSONIC NOZZLES

Nozzles constitute a crucial part of every propulsion system, thanks to their ability to convert the internal energy of a working fluid, such as the hot gaseous products of a combustion reaction, into kinetic energy. This process accelerates the fluid, generating the momentum required for the thrust force. Nozzles are primarily regarded as continuous ducts with variable cross-sectional areas. The basic theory of nozzles is well-established, straightforward to apply, and provides satisfactory predictions of the flow field and its performance. All these aspects are found in more detail through subsequent readings.

Based on their geometrical configuration, two basic types of nozzles can be distinguished:

- **Convergent nozzles (CN):** They are primarily used in subsonic and low-speed flow applications. These nozzles are commonly found in industrial machinery, such as jet engines operating at subsonic speeds, gas turbines, and chemical processing equipment, where controlled flow and pressure are essential. Convergent nozzles accelerate the fluid or gas to the desired velocity without reaching supersonic speeds, making them ideal for applications where the flow remains below the speed of sound.
- **Convergent-Divergent nozzles (CDN):** First proposed by Gustaf de Laval at the end of the 19th century (hence they are often referred to as Laval nozzles), these nozzles form the foundational model for supersonic nozzle concepts. Their unique characteristics have made them the workhorse in rocket, missile, and supersonic aircraft propulsion applications. Typically, they consist of a convergent section where the flow is accelerated in the subsonic regime to reach sonic conditions at the throat (the minimum cross-sectional area of the nozzle). The flow then expands in the divergent section, accelerating to supersonic speeds. The well-known Area-Mach relation mathematically describes this behavior.

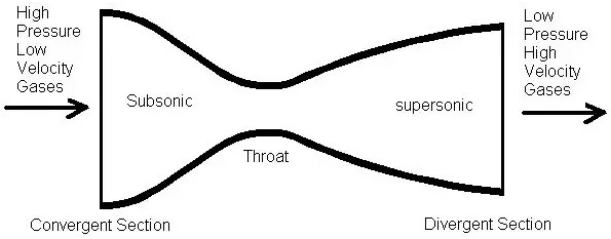

Figure 1.2 : Schematic description of supersonic CD nozzle.

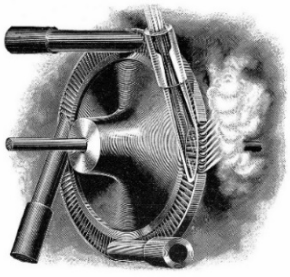

Figure 1.1 : De Laval Steam Engine (Wikipedia).

Figure 1.3 : Gustave de Laval (Wikipedia).

1.1 Steady Quasi One-Dimensional Ideal Flow Relations

In this first part, we will assume that the pressure governing the outlet of the nozzle is so small that it doesn't have any influence on the behavior of the flow inside the nozzle. This assumption allows the properties studied in this case to be considered intrinsic to the nozzle. These properties, which are of great importance, include the maximum flow rate and the thrust.

As soon as we give the pressure P_0 and the enthalpy h_0 of the fluid supposed practically at rest at the nozzle inlet, we can demonstrate that all the expansion is determined by the nozzle shape. A first approximation can be obtained by neglecting the effect of viscosity and fluid conductivity, or in other words we consider an Ideal Gas, and by supposing the flow to be uniform at any cross-sectional station in the nozzle, we define the mono-dimensional theory. Now let's get deeper into the equations.

For the assumptions given above and considering a steady-state flow, we can show easily that the governing flow equations reduce to the following,

- Mass Conservation,

$$\dot{m} = \rho U A = \rho^* U^* A^* = constant \tag{1-1}$$

This states that the mass flow rate is conserved at any section on the nozzle. Where the mass flow rate is the product of density, axial velocity (the uniform sectional velocity along the principle axis) into the surface area of the section perpendicular to flow at that position (note that the Asterix notation refers to the throat properties).

- Momentum Conservation,

$$\rho U \, dU + dP = 0 \tag{1-2}$$

This is only an application of Newton's second law to an infinitesimal fixed control volume. Here in this particular example, as the flow is one dimensional, we can correctly speak about an infinitesimal line element without loss of generality and it could be expressed as dx if we denote our principle axis "x" and as all proprieties are only functions of x so any derivative can also be expressed as total differential.

- Energy Conservation,

$$h + \frac{1}{2} U^2 = h_0 = constant \tag{1-3}$$

This is a statement of the principle of conservation of energy. In this particular equation, we can observe that the total energy of the flow is conserved, and no heat or work is exchanged by the gas, so the gas is converting its energy by external influence (continuous shape variation of the nozzle) between kinetic and internal energy as it flows through the nozzle.

In this we can find that the maximum limiting velocity attainable by the flow can be expressed as,

$$U_{lim} = \sqrt{2 \cdot h_0} \tag{1-4}$$

- Thermodynamic State Equations,

$$P = \rho R T \tag{1-5}$$

$$\begin{aligned} e(T) &= c_v T \\ h(T) &= c_p T \end{aligned} \tag{1-6}$$

Here are the last equations needed to close the system and resolve this problem. These are models that describe the relations between state variables of the fluid which are macroscopic properties of the gas, alternatives to the microscopic or molecular description, in the continuum concept. Much more attention should be given to this part as it's essential, it relates the flow to fluid properties.

Eq. (1-5) is the expression of the thermodynamic state equation of a perfect gas, by definition a perfect gas is one in which intermolecular forces are neglected. By ignoring intermolecular forces, this equation can be derived from theoretical concepts of modern statistical mechanics or kinetic theory. In this, we note that:

- $R = \mathbb{R}/M_w$ is the gas constant. where $\mathbb{R} = 8314\, J/(kmol \cdot K)$, and M_w $[Kg/kmol]$ is the molecular weight of the gas.
- T is the gas Temperature.

Returning to our microscopic view of gas as a collection of particles in random motion, the individual kinetic energy of each particle contributes to the overall energy of the gas. Moreover, if the particle is a molecule, its rotational and vibrational motions also contribute to the gas energy. Finally, the motion of electrons in both atoms and molecules is a source of energy. In turn, these energies, summed over all the particles of the gas, constitute the internal energy, E, of the gas. Moreover, if the particles of the gas (called the system) are rattling about in their state of "maximum disorder", the system of particles will be in equilibrium [5].

Return now to the macroscopic view of the gas as a continuum. Here, equilibrium is evidenced by no gradient in velocity, pressure, temperature, and chemical concentrations throughout the system, i.e., the system has uniform properties in a given state conditions. For an equilibrium system of

real gas where intermolecular forces are important, and also for an equilibrium chemically reacting mixture of perfect gases, the internal energy is a function of both temperature and volume [5]. Let e denote the specific internal energy (internal energy per unit mass). Then, enthalpy, h, is defined, per unit mass, as $h = e + pv$, and we have

$$\begin{aligned} e &= e(T, v) \\ h &= h(T, P) \end{aligned} \tag{1-7}$$

For both a real gas and a chemically reacting mixture of perfect gases.

If the gas is not chemically reacting, and if we ignore intermolecular forces, the resulting system is a thermally perfect gas, where internal energy and enthalpy are functions of temperature only, and where the specific heat capacities at constant volume and pressure, c_v and c_p, are also functions of temperature only:

$$\begin{aligned} e &= e(T) \\ h &= h(T) \\ de &= c_v\, dT \\ dh &= c_p\, dT \end{aligned} \tag{1-8}$$

The temperature variation of c_v and c_p is associated with the vibrational and electronic motion of the particles.

Finally, if the specific heats are constant, the system is a calorically perfect gas, where the energies result in Eq. (1-6) (it has been assumed that $h = e = 0$ at $T = 0$). This small sketch of atomic and molecular energies can be enlarged to a massive portrait in [5].

Now let us move to introduce some other important concepts related to compressible flow.

Entropy, or specific entropy denoted "s", is another state variable that is used in combination with the second law of thermodynamics, allows us to predict the direction that nature takes when energy (heat) is transferred across the boundaries of the system. So, by definition,

$$ds = \frac{\delta q_{rev}}{T} \tag{1-9}$$

Where δq_{rev} is an incremental amount of heat added reversibly to the system, and T is the system temperature. Do not be confused by this definition. It defines a change in entropy in terms of a reversible addition of heat. However, entropy can be used in conjunction with any type of process, reversible or irreversible. The quantity δq_{rev} is just an artifice; an effective value of δq_{rev} can always be assigned to relate the initial and end points of an irreversible process, where the actual amount of heat added is δq. Indeed, an alternative and probably more lucid relation is

$$ds = \frac{\delta q}{T} + ds_{irrev} \tag{1-10}$$

This last equation applies in general; it states that the change in entropy during any incremental process is equal to the actual heat added divided by the temperature, $\delta q/T$, plus a contribution from the irreversible dissipative phenomena of viscosity, thermal conductivity, mass diffusion, and shock waves occurring within the system, ds_{irrev}. These dissipative phenomena always increase the entropy:

$$ds_{irrev} \geq 0 \tag{1-11}$$

The equal sign denotes a reversible process, where, by definition, the dissipative phenomena are absent. Hence, a combination of Eqs. (1-9) and (1-10) yields

$$ds \geq \frac{\delta q}{T} \tag{1-12}$$

Furthermore, if the process is adiabatic, $\delta q = 0$, and Eq. (1-11) becomes

$$ds \geq 0 \tag{1-13}$$

Equations (1-12) and (1-13) are forms of the second law of thermodynamics. The second law tells us in what direction a process will take place. A process will proceed in a direction such that the entropy of the system plus its surroundings always increases, or at best stays the same.

In this hypothetical theory, we assumed equilibrium perfect gas neglecting all dissipative phenomena with no heat or work done by the system. So, the system is said to be isentropic, it means no variation in the entropy is made as the gas flows (the limiting case $ds = 0$), this gives important relations that govern the fluid flow properties. These are obtained by combining Eqs. (1-3), (1-5), (1-6), (1-9) along with the definitions of enthalpy and the first principle of energy for a system. The derivation is not given here but they can be found in any textbook of thermodynamics or compressible flow [5] [6]. Before displaying the equations, we need to define some parameters that appear explicitly in the equations.

1.1.1 Mach Number and Sound Velocity

The Mach number (M) is a very important parameter in this study and generally in all compressible flow, it is defined as the ratio between the actual flow velocity to the sound velocity at a given location.

$$M = \frac{U}{c} \tag{1-14}$$

Here the sound speed "c" is another important parameter in compressible flow, it is closely connected with the velocity of propagation of small pressure disturbances, i.e., with the velocity of sound. It can be shown that these pressure waves imply variation in density as they propagate through the flow field [6]. The rate of change of density with respect to pressure is, therefore, related to the sound speed by

$$c^2 = \left(\frac{\partial P}{\partial \rho}\right)_s \quad or \quad c = \sqrt{\left(\frac{\partial P}{\partial \rho}\right)_s} \tag{1-15}$$

The ratio $\partial P/\partial \rho$ is written in Eq. (1-15) as a partial derivative at constant entropy because the variations in pressure and temperature are vanishingly small, and consequently, the process is nearly reversible. Moreover, the comparative rapidity of the process, together with the smallness of the temperature variations, makes the process nearly adiabatic [6]. In the limit, for an infinitesimal wave, the process may be considered both reversible and adiabatic, and, therefore, isentropic [6].

Thus, for a perfect gas the Eq. (1-14) & (1-15) yields,

$$\begin{aligned} c &= \sqrt{\gamma R T} \\ M &= \frac{U}{\sqrt{\gamma R T}} \end{aligned} \tag{1-16}$$

Here γ is the ratio between heat capacities. Important expressions that relate these quantities are,

$$\begin{aligned} \gamma &= c_p/c_v \\ c_p - c_v &= R \\ c_p &= \gamma R/(\gamma - 1) \\ c_v &= R/(\gamma - 1) \end{aligned} \tag{1-17}$$

1.1.2 Isentropic Flow Relations

$$\begin{aligned}
\frac{T_0}{T} &= 1 + \frac{\gamma - 1}{2}\,(M)^2 \\
\frac{P_0}{P} &= \left[1 + \frac{\gamma - 1}{2}\,(M)^2\right]^{\frac{\gamma}{\gamma-1}} \\
\frac{\rho_0}{\rho} &= \left[1 + \frac{\gamma - 1}{2}\,(M)^2\right]^{\frac{1}{\gamma-1}} \\
\frac{U}{U_{lim}} &= \left[\frac{(\gamma - 1)\,M^2}{2 + (\gamma - 1)\,M^2}\right]^{\frac{1}{2}}
\end{aligned} \tag{1-18}$$

These Equations are valid in any isentropic flow, they relate the stagnation conditions "0" to the local flow variables. They are all given explicitly as a function of the local Mach number M and heat capacities ratio γ. In our problem we have supposed that the stagnation conditions are governing our nozzle inlet and sonic conditions ($M = 1$) are those characterizing the flow at the throat so that Eq. (1-18) yields.

$$\begin{aligned}
\frac{T^*}{T_0} &= \frac{2}{\gamma + 1} \\
\frac{P^*}{P_0} &= \left[\frac{2}{\gamma + 1}\right]^{\frac{\gamma}{\gamma-1}} \\
\frac{\rho^*}{\rho_0} &= \left[\frac{2}{\gamma + 1}\right]^{\frac{1}{\gamma-1}} \\
\frac{U^*}{U_{lim}} &= \left[\frac{\gamma - 1}{\gamma + 1}\right]^{\frac{1}{2}}
\end{aligned} \tag{1-19}$$

1.1.3 Area-Mach Relation

Finally, in this section, we will try to express the most important equation the Area-Mach relation. By differentiating the natural logarithm of Eq. (1-1) and substituting Eqs. (1-15), (1-2), (1-16) respectively, we arrive to the result,

$$\begin{aligned}
\frac{dA}{A} = -\frac{d\rho}{\rho} - \frac{dU}{U} = -\left(\frac{\partial \rho}{\partial P}\right)_s \cdot \frac{dP}{\rho} - \frac{dU}{U} = \frac{1}{c^2} \cdot \frac{(\rho\, U^2 dU)}{\rho\, U} - \frac{dU}{U} = \left(\frac{U^2}{c^2} - 1\right) \cdot \frac{dU}{U} \\
\frac{dA}{A} = (M^2 - 1) \cdot \frac{dU}{U}
\end{aligned} \tag{1-20}$$

The equation (1-20) relates the variation in the area of the duct to the internal flow velocity. Here we can see that the Mach number is a proportionality factor and it drives a very interesting result between velocity and area. See Figure 1.4.

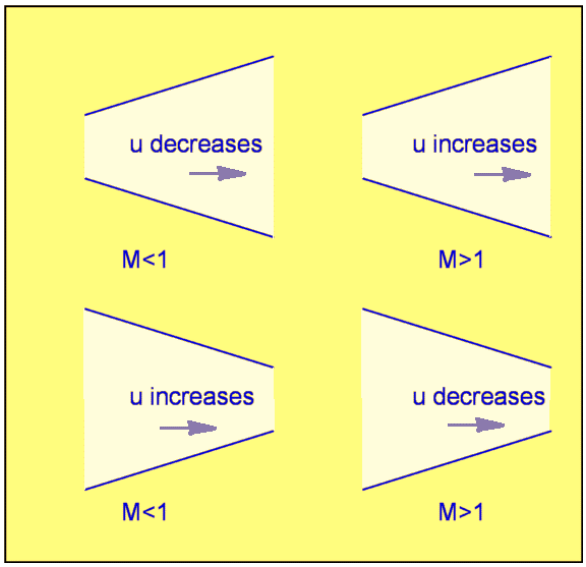

Figure 1.4 : Shematic representation of area velocity relation [12].

By combining Eq. (1-2) with this result we can also obtain a relation between area variation and pressure as pressure behaves in contrast to velocity.

More interestingly, we can obtain an explicit relation between area ratio and Mach number in the form of Eqs. (1-18). Returning to equations (1-1) and (1-18) we can express that,

$$\frac{\dot{m}}{A} = \sqrt{\frac{\gamma}{R}} \cdot \frac{P_0}{\sqrt{T_0}} \cdot \frac{M}{\left(1 + \frac{\gamma - 1}{2} M^2\right)^{\frac{\gamma+1}{2(\gamma-1)}}}$$
$$\left(\frac{\dot{m}}{A}\right)_{max} = \frac{\dot{m}}{A^*} = \sqrt{\frac{\gamma}{R}} \cdot \frac{P_0}{\sqrt{T_0}} \cdot \left(\frac{2}{\gamma + 1}\right)^{\frac{\gamma+1}{2(\gamma-1)}} \tag{1-21}$$

Thus,

$$\frac{A}{A^*} = \frac{1}{M} \cdot \left[\frac{2}{\gamma + 1}\left(1 + \frac{\gamma - 1}{2} M^2\right)\right]^{\frac{\gamma+1}{2(\gamma-1)}} \tag{1-22}$$

In Eq. (1-21), to find the condition of maximum flow rate per unit area, we could compute the derivative $(\dot{m}/A)$ with respect to M and set this derivative equal to zero. At this condition, we would find that it corresponds to $M = 1$. Respectively, the cross-sectional area for an isentropic flow passes through a minimum at Mach Number unity (choked nozzle). Therefore, in Eq. (1-21),

for a given gas, the maximum flow per unit area depends only on the ratio $P_0/\sqrt{T_0}$. While, for specific values of stagnation pressure, stagnation temperature, and a passage with a defined minimum area, the maximum flow that can be passed is relatively large for gases of high molecular weight and relatively small for gases of low molecular weight.

1.1.4 Summery

In this Table, we summarize all the important relations derived from the mono-dimensional theory.

Table 1.1 : Steady Quasi-1D Isentropic Flow Relations

$$\frac{T_0}{T} = 1 + \frac{\gamma - 1}{2}(M)^2$$

$$\frac{P_0}{P} = \left[1 + \frac{\gamma - 1}{2}(M)^2\right]^{\frac{\gamma}{\gamma-1}}$$

$$\frac{\rho_0}{\rho} = \left[1 + \frac{\gamma - 1}{2}(M)^2\right]^{\frac{1}{\gamma-1}}$$

$$\frac{U}{U_{lim}} = \left[\frac{(\gamma - 1)\,M^2}{2 + (\gamma - 1)\,M^2}\right]^{\frac{1}{2}}$$

$$\frac{A}{A^*} = \frac{1}{M} \cdot \left[\frac{2}{\gamma + 1}\left(1 + \frac{\gamma - 1}{2}\,M^2\right)\right]^{\frac{\gamma+1}{2(\gamma-1)}}$$

$$\frac{\dot{m}}{A^*} = \sqrt{\frac{\gamma}{R}} \cdot \frac{P_0}{\sqrt{T_0}} \cdot \left(\frac{2}{\gamma + 1}\right)^{\frac{\gamma+1}{2(\gamma-1)}}$$

An application of these equations to our problem will be for air considered as calorically perfect gas, since, we will perform clod test experiments.

For air at normal conditions $R = 287.034\,\frac{J}{Kg\,K}$ and $\gamma = 1.4$, results are given in Table 1.2 and Figure 1.5.

Table 1.2 : Theory Application to Air

$$\frac{T^*}{T_0} = \frac{5}{6} \approx 0.833$$
$$\frac{P^*}{P_0} = 0.52828$$
$$\frac{\rho^*}{\rho_0} = 0.63394$$
$$\frac{U^*}{U_{lim}} = 0.40825$$
$$\frac{\dot{m}\sqrt{T_0}}{A^* P_0} = 0.040416$$

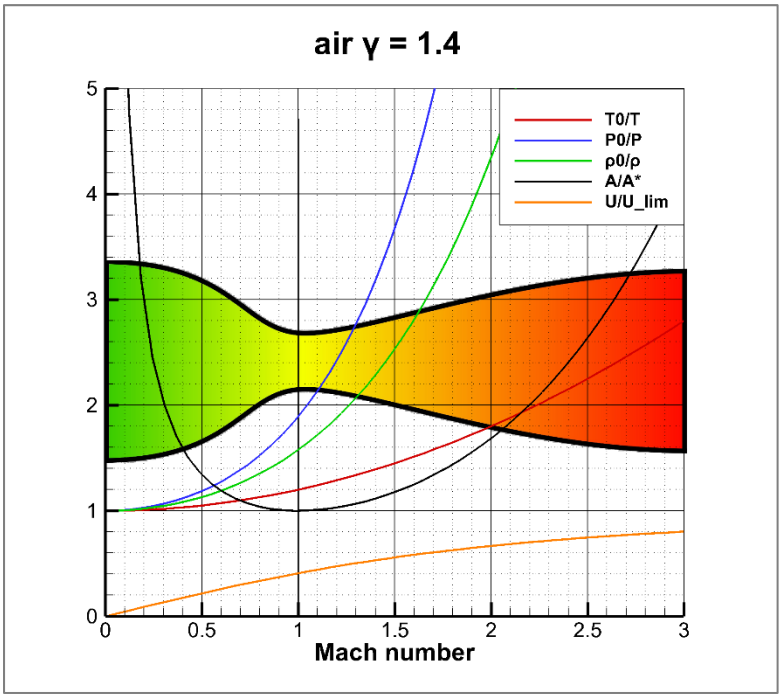

Figure 1.5 : Graphical representation of isentropic relations for air at normal conditions.

1.1.5 The limits associated with the use of the hypothesis of calorically perfect gas

The simplicity of equations derived above allows the use of the hypothesis of perfect gas in first approximation, however, in real cases, for thermally perfect gas and/or dissociative gas such as in combustion (high-temperature gases), these equations would not be such explicit.

The above graphic shows the variation of $\bar{\gamma}$ for air-kerosene combustion gases at diverse mixture ratios. (the overbar denotes a mixture average value).

$$\phi = \frac{kerosens\ (fuel)\ mass\ flow}{air\ mass\ flow} \tag{1-23}$$

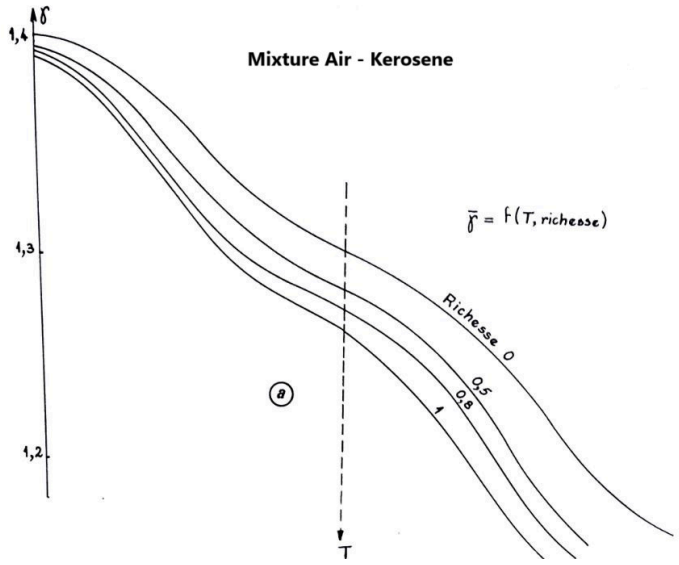

Figure 1.6 : Variation of $\bar{\gamma}$ for air-kerosene mixture with Temperature [7].

We note that:

- For $T < 600\ K$, we can assume without many errors the value $\bar{\gamma} = 1.4$;
- For $600\ K < T < 1600\ K$, the gas behaves in this case as a thermally perfect gas for which $\bar{\gamma}$ becomes highly dependent on T due to the molecular agitation described before;
- For $1600\ K < T$, $\bar{\gamma}$ varies with T and P as a result of dissociations in the gas. In this case, the air can no longer be considered as a perfect gas, and much more precise calculations here are necessary.

However, we notice that in the calculation of the mass flow rate, the variation in temperature between the inlet and the throat is always moderated [7].

$$\frac{T_0 - T^*}{T_0} = \frac{\gamma - 1}{\gamma + 1} \sim 10\%$$

Such that until $T = 2000\ K$, we can use the formula for $\gamma = cst$, where γ is taken as the average value between (P_0, T_0) and (P^*, T^*). But for the other flow parameters, it is not possible as non-negligible errors would be made.

1.2 Rocket Nozzle Performance

1.2.1 The Thrust Force

The application of the general principle of conservation of momentum to the control volume that bounds the nozzle contour would yield, in the steady state, the General Thrust Equation [7].

$$F = \left(\dot{m}_p\, V + P \cdot A\right)_{exit} - \left(\dot{m}_p\, V + P \cdot A\right)_{inlet} \tag{1-24}$$

Here $\dot{m}_p$ denote the mass flow rate of propellants. As in most cases for rocket engines as well in our mono-dimensional theory, the inlet conditions are supposed to be the stagnation conditions, so theoretically, no flow crosses the boundaries at the inlet. The term drops from the equation yielding the Intrinsic (Ideal) Thrust Force for rocket nozzles.

$$\bar{F} = \dot{m}_p\, V_e + P_e \cdot A_e \tag{1-25}$$

The thrust force that is defined here results only from the action of the flow on the nozzle body. This is true as long as the external ambient conditions would not influence the flow, this is the case of supersonic nozzle discharging in a low-pressure atmosphere as at high altitude flight and out space conditions. However, in the general case if we take the effect of ambient pressure P_a yields the equation of the Conventional Thrust Force.

$$F = \dot{m}_p\, V_e + (P_e - P_a) \cdot A_e \tag{1-26}$$

If the conditions are such that $P_e = P_a$, the nozzle is said to be adapted and the resulting adapted conventional thrust force is then,

$$F_{ad} = \dot{m}_p\, V_e \tag{1-27}$$

1.2.2 Effective Exhaust velocity

We know that the velocity profile at the nozzle exit is not one-dimensional for practical situations. It is quite cumbersome to determine the velocity profile at the exit of a rocket nozzle. To tackle this problem, we can define a one-dimensional effective exhaust velocity V_{eq} as,

$$V_{eq} = \frac{F}{\dot{m}_p} = V_e + \frac{P_e - P_a}{\dot{m}_p} \cdot A_e \tag{1-28}$$

1.2.3 The specific impulse

It provides a measure of the efficiency of a rocket engine, defined as the thrust produced per unit of propellant consumed per second (I_{sp}). It is usually expressed in seconds and indicates how effectively the engine uses the propellant.

$$I_{sp} = \frac{F}{\dot{m}_p \, g_0} \tag{1-29}$$

g_0 is the acceleration due to gravity at the earth's sea level.

1.2.4 Total Impulse

Total Impulse I is a measure of the overall performance of a rocket engine. It represents the total amount of momentum change (or thrust) produced over the entire duration of the engine's operation. Mathematically, it is defined as:

$$I = F \cdot t \tag{1-30}$$

Alternatively, if the thrust is not constant, the total impulse is calculated by integrating the thrust over time.

$$I = \int_0^t F \cdot dt \tag{1-31}$$

The total impulse is an essential parameter in evaluating a rocket's performance, as it directly correlates to the ability of the engine to propel a vehicle or payload.

1.2.5 The Thrust coefficient

The thrust coefficient C_T is a dimensionless parameter used to evaluate the efficiency of a nozzle in converting the pressure and momentum of exhaust gases into thrust. It is an important performance metric in rocket engine design and analysis.

Mathematically, the thrust coefficient is defined as:

$$C_T = \frac{F}{P_0 A^*} \tag{1-32}$$

The thrust coefficient depends on factors like:

- The nozzle's geometry (divergence angle and expansion ratio);
- The pressure ratio between the chamber and the ambient;

- Flow conditions (subsonic or supersonic).

It is particularly useful for comparing nozzles of different sizes and configurations, as it normalizes thrust with respect to chamber pressure and nozzle throat area.

1.2.6 Different Losses encountered in nozzles

Performance data for rocket engines are practically always lower than the theoretically attainable values because of imperfections in the mixing, combustion, and expansion of the propellants [8]. Figure 1.7 illustrates the different loss sources in rocket engine nozzles. The examination and evaluation of these loss effects is and has for some time been the subject of research at scientific institutes and in industry.

Table 1.3 summarizes performance losses in the thrust chambers and nozzles of typical high-performance rocket engines: The SSME- and Vulcain 1 engine [8] (Space Shuttle main engine, Rocketdyne hydrogen-oxygen engine and hydrogen-oxygen core engine of European Ariane-5 launcher). Among the important loss sources in thrust chambers and nozzles are viscous effects because of turbulent boundary layers and the nonuniformity of the flow in the exit area, whereas chemical nonequilibrium effects can be neglected in $H_2 - O_2$ rocket engines with chamber pressures above $P_c = 50\ bar$ [8]. Furthermore, the nonadaptation of the exhaust flow to varying ambient pressures induces a significant negative thrust contribution. Ambient pressures that are higher than nozzle wall exit pressures also increase the danger of flow separation inside the nozzle, resulting in the possible generation of side loads. A brief description of state-of-the-art prediction methods for both phenomena is the subject of the next chapter.

Table 1.3 : Performance losses in conventional rocket nozzles [8].

Losses	Vulcain 1, %	SSME,%
Chemical nonequilibrium	0.2	0.1
Friction	1.1	0.6
Divergence, nonuniformity of exit flow	1.2	1.0
Imperfections in mixing and combustion	1.0	0.5
Non-adapted nozzle flow	$0 - 15$	$0 - 15$

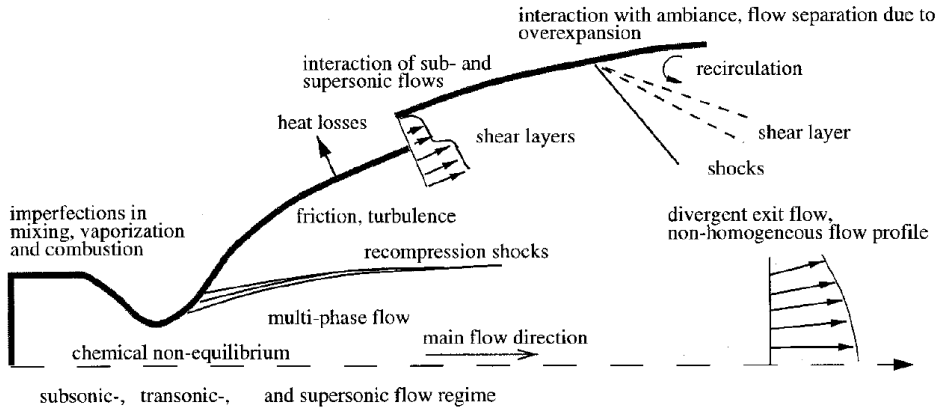

Figure 1.7 : Flow phenomena and loss sources in rocket nozzles [8].

1.3 The behavior of the Nozzle in Atmosphere

The different operating modes for a given CDN in the presence of an adverse pressure, or back pressure (atmospheric effect), can be also described by the mono-dimensional theory for ideal gas. This approach allows us to understand the formation of normal shock wave inside the nozzle. The difference between the generating pressure ($P_c \cong P_0$) upstream and the ambient pressure (P_a) downstream of the nozzle creates the flow (see Figure 1.8). The first regime of flow is subsonic throughout the nozzle. At this stage by continuously decreasing P_a, the mass flow rate increases progressively until it gets to its limit when the flow reaches sonic conditions at the throat. The mass flow rate is then blocked (chocked nozzle) and the pressure downstream will tend to P_a^{sonic}. If the pressure downstream goes below P_a^{sonic}, the throat remains in the chocked state and the flow in the divergent section will start reaching supersonic conditions. However, the adaptation to the ambient pressure will proceed through a normal shock wave positioned at X_{shock}, which is represented by a jump in the evolution of P/P_c . The flow follows the isentropic supersonic solution upstream the shock and downstream side we will get subsonic flow. The normal shock moves downstream the nozzle as the back pressure is reduced and for one specific back pressure $P_a = P_a^{sup}$ we will have a normal shock standing at the nozzle exit plane, while the flow is completely supersonic in the divergent [9].

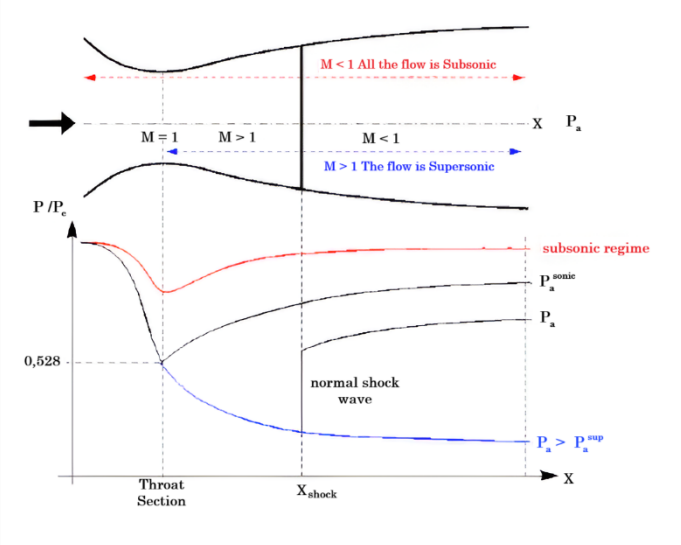

Figure 1.8 : Working principle of a convergent divergent nozzle [9].

Reducing the back pressure further, results in over-expanded conditions leading to the generation of oblique shocks at the nozzle exit going out from the nozzle.

With the further decrease of back pressure, we may reach pressure-matched conditions (adapted nozzle conditions, flow without shocks or expansion waves), and below that, we will get the formation of expansion waves at the nozzle exit. In the latter case, the nozzle is said to be operating at under-expanded conditions.

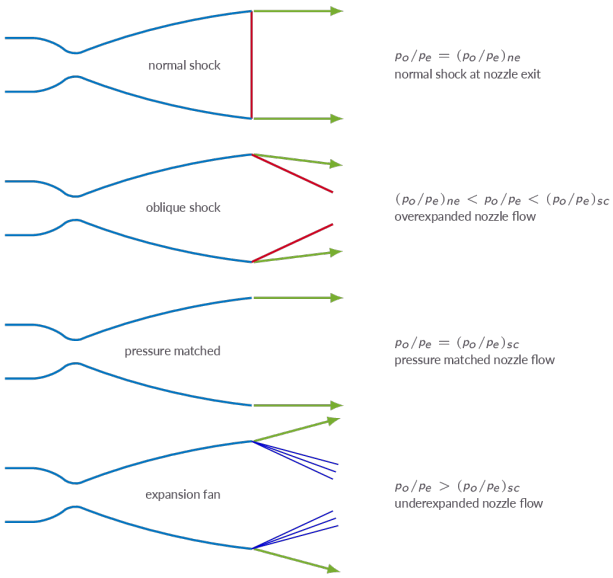

Figure 1.9 : Under-expended and over-expended nozzle flow [10].

Note that all these latter effects (Figure 1.9) will not influence the constrained supersonic flow inside the nozzle, nevertheless, these effects will significantly characterize nozzle performance. To perform such calculations, the quasi-1D theory along with shock and expansion waves relations described in Appendix A are sufficient. An example of such application to the experimental conical nozzle studied here is given in Appendix B.

The introduction of viscosity effects significantly complicates the described flow regimes. One notable consequence is the formation of a boundary layer, caused by non-slip conditions. The

interaction of this boundary layer with the main flow, shock waves, and ambient field can result in transient, non-uniform, and asymmetric flow behavior (see Figures 1.10, 1.11) [11].

Adapted Regime ($P_a = P_e$): In this regime, the flow completes its expansion within the nozzle with final pressure adapted to the ambient. At the nozzle exit, the supersonic jet flow is quasi-uniform, shockless, and an isobaric boundary separates the jet from the surrounding air. Viscous forces (shear layers) at the edges of the plume will cause it to diverge gradually in this case as ambient air is entrained into the high-speed flow.

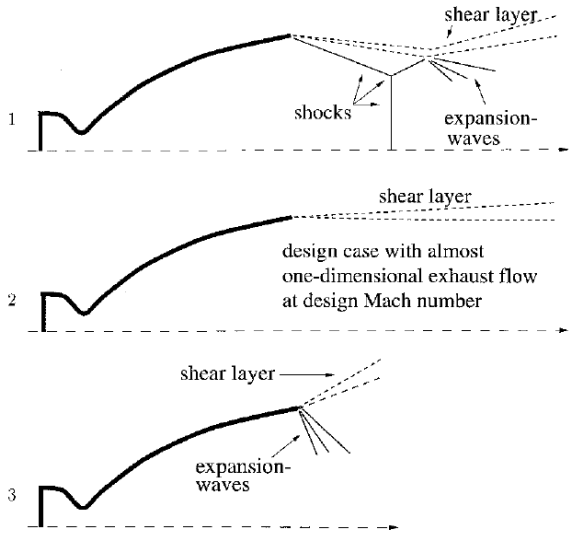

Figure 1.10 : Flow phenomena for a conventional rocket nozzle [8].

Under-Expanded Regime ($P_a < P_e$): Here, the gas does not fully expand within the nozzle and continues expanding at its exit. This results in a series of expansion waves, causing the jet to extend outward. Consequently, the free jet boundary or shear layer takes on a divergent-like shape.

Over-Expended Regime ($P_a > P_e$): At this stage, the boundary layer at the exit of the nozzle is subtended to an adverse pressure gradient forcing it to become thicker. Compression waves, then,

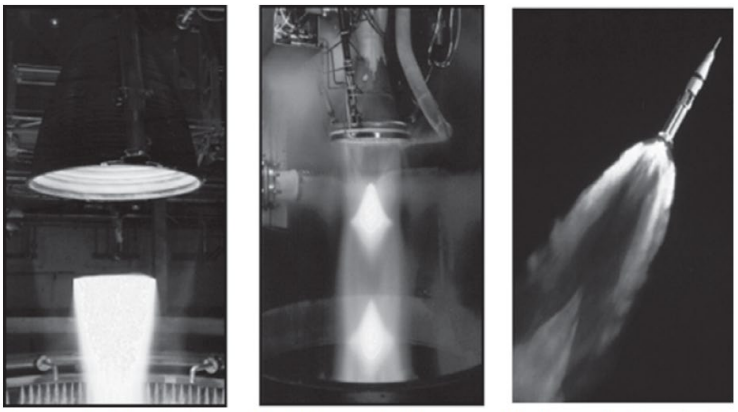

Figure 1.11 : Nozzle plume characteristics at various exit pressure conditions [11].

start forming at the lips of the nozzle leading to the development of a shock wave which, in the first case, doesn't result in boundary layer separation. Further downstream, a system of shocks and expansion waves leads to the characteristic barrel-like form of the exhaust flow.

When the flow is highly over-expanded, there is potential for separation within the nozzle. The separation can occur over just a portion of the circumference (asymmetric separation), or uniformly around the entire circumference. At the separation region, the flow is qualitatively illustrated in Figure 1.12. Point O marks the origin of interaction, where compression waves emerge and converge into an oblique shock at the separation point S, deflecting the flow.

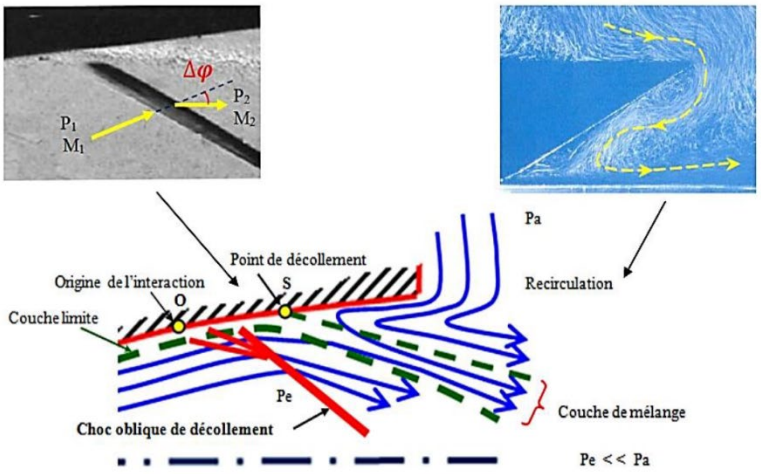

Figure 1.12 : Over-expended nozzle with free shock separation [4].

Downstream of point S, the interaction between the separated turbulent boundary layer and the low-speed flow downstream (commonly referred to as "dead water" flow) generates a viscous and turbulent mixed layer.

Figure 1.13 depicts the impact of separation on the wall pressure distribution. The dotted curve represents the evolution of wall pressure in the adapted regime. In the over-expanded regime without separation, the pressure increases near the nozzle lip and ultimately reaches atmospheric pressure. Conversely, in the over-expanded regime with separation, the pressure initially rises but then asymptotically approaches the pressure in the dead water zone, which is close to ambient pressure, P_a. This evolution in wall pressure influences the nozzle thrust. Therefore, knowing the

position of the separation point S and the pressure jump across the shock is crucial for accurately assessing nozzle performance [9].

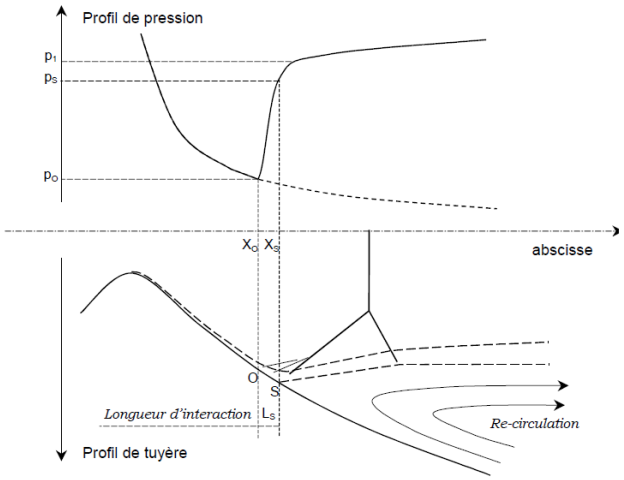

Figure 1.13 : Wall pressure distribution for free shock separation [9].

For a given nozzle pressure ratio ($NPR = P_c/P_a$), it is still difficult to predict whether the over-expansion will cause separation and, if separation occurs, determining the position of the separation point and the evolution of the wall pressure remains challenging. This difficulty arises from the complexity of the physical phenomena encountered in such flows, which are highly compressible and turbulent. The following chapter gives an insight into the phenomenology of flow separation in over-expanded nozzles and some predictive criteria, often derived from experimental data and theoretical models, that have been obtained from researchers in the literature. Lastly, in Figure 1.14 where the thrust ratio between the maximum $P_a = P_e$ (adapted regime) and the actual thrust force for different values of P_a/P_e is plotted. When P_e is less then P_a, there is a drop in the thrust such that in the absence of separation, this loss rises regularly as P_e/P_a is decreasing. The intervention of separation has as effect of limiting the zone of over-expansion in the nozzle, in such a way that the thrust stabilizes practically when the separation occurs [7].

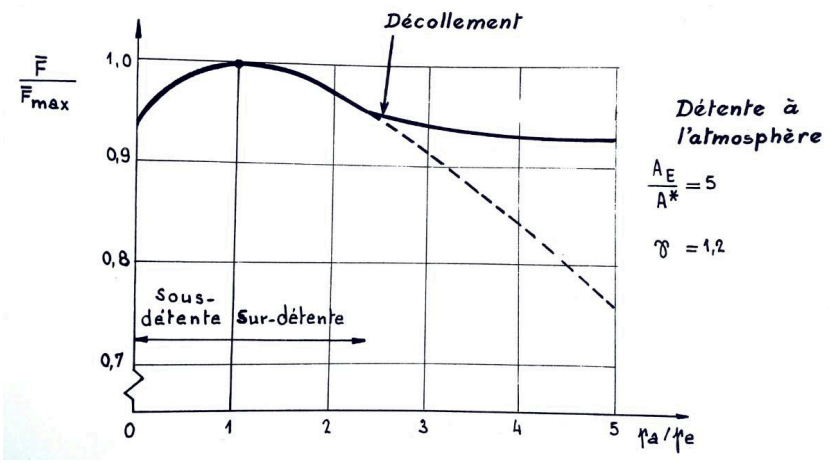

Figure 1.14 : Thrust force variation with pressure ratio P_a/P_e at all operation regimes off- and adapter conditions [7].

1.4 Supersonic Nozzle Designs

1.4.1 Conventional Nozzles

In the design of rocket nozzles, there are several parameters that must be considered, such as performance requirements, maximum acceptable engine mass, limitations on the main dimensions, cooling performance, lifetime considerations, manufacturing methods, etc. Minimizing the weight is one of the main parameters, i.e. keeping the nozzle length and surface area at a minimum. The main gas dynamics problem lies in optimally contouring the nozzle in order to maximize efficiency. From a purely inviscid point of view, nozzles can be classified into different types, each producing its specific internal flow field [3].

The designer must understand these features, since the internal flow field determines the flow separation and side load behavior. Figure 1.15 shows examples of the Mach number distribution in some of the most common nozzle types, which will be discussed below.

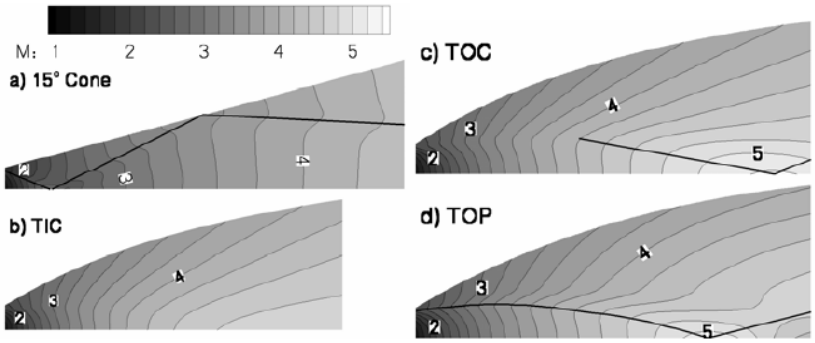

Figure 1.15 : Mach distribution in different nozzles with $\varepsilon = 43.4$. The thick line indicates the approximate position of the internal shock, [13].

The initial expansion region (Kernel)

As it turned out in Figure 1.15, the flow field has a more complex structure than the isentropic 1D flow described in Section 1.1. Currently, the method of characteristics (MOC), discussed subsequently, is the most common calculation method to compute flow fields in rocket nozzles. The calculations of the flow properties downstream of the nozzle are based on the kernel, which is determined by the initial expansion that occurs along the throat contour TN, which is usually designed as a circular arc, see Figure 1.16.

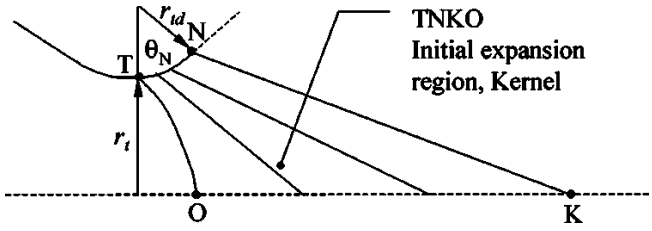

Figure 1.16 : Initial expansion region, kernel, [13].

Conical Nozzle

The conical nozzle has historically been the most common contour for rocket engines since it is simple and usually easy to fabricate. The exhaust velocity of a conical nozzle is essentially equal to the one-dimensional value corresponding to its expansion ratio, except that the flow direction is

not axial all over the exit area. Hence, there is a performance loss due to the flow divergence. Assuming conical flow at the exit, Malina [14] showed that the geometrical efficiency is

$$\eta_{geo} = \frac{1 + \cos(\alpha)}{2} \tag{1-33}$$

Where α denotes the nozzle cone half angle. The length of the conical nozzle can be expressed as

$$L_{\alpha^\circ,cone} = \frac{r_t\left(\sqrt{\varepsilon} - 1\right) + r_{td}\ (\sec(\alpha) - 1)}{\tan\alpha} \tag{1-34}$$

Where:

r_t: Represents the throat radius.

ε: Denotes the expansion ratio.

α: Denotes the half-angle of the divergence.

r_{td}: Denotes the radius contribution at the divergent exit or trailing edge.

$L_{\alpha,cone}$: Overall conical divergent length.

Typically, cone half angles range between 12° to 18°. A common compromise is a half angle of 15°.

Due to its high divergence losses, the conical nozzle is nowadays mainly used in short nozzles like solid rocket boosters and small thrusters, where simple fabrication is preferred over aerodynamic performance.

Ideal (Bell) Nozzle

The ideal nozzle is designed to produce an isotopic flow (i.e. a flow without any internal shocks) and a uniform exit velocity. Figure 1.17 describes the flow field of an ideal nozzle. After the initial section TN, the contour NE turns the flow in the axial direction. TN also defines the Mach number at K, which is equal to the design Mach number obtained at the exit. With the characteristic line NK defined and the condition that the characteristic line KE is a uniform exit characteristic, it is possible to use MOC to construct the streamline between N and E, which patches the flow to become uniform and parallel at the exit.

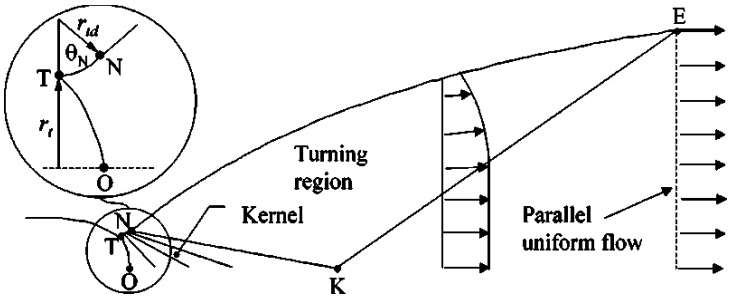

Figure 1.17 : Basic flow structures in an ideal nozzle, [13].

Truncated Ideal Contoured nozzles (TIC and CTIC)

Making the exit flow uniform demands the nozzle to be very long, therefore, the ideal nozzle is not suitable for rocket applications. However, since the thrust contribution in the last part of the nozzle is negligible due to the small wall slope a more effective nozzle is obtained by truncating the contour, i.e. the truncated ideal contoured nozzle (TIC). The exit velocity profile of a TIC nozzle will have a central part that is uniform and parallel, and a divergent part close to the wall, see Figure 1.17. The truncation can be made as far upstream as the kernel, and as long as the kernel is undisturbed, the MOC can be used to calculate the flow field downstream of the nozzle. Figure 1.15(b) illustrates the Mach number distribution. An optimization technique by Ahlberg [15] is used to find the best performances for a nozzle with a certain mass, surface area, exit diameter, length, and thrust coefficient. TIC nozzles are for example used in the European Ariane 4 and the American Saturn-1 launcher.

A version of the TIC nozzle is the compressed TIC nozzle (CTIC). The design method of the CTIC nozzle was developed by the Japanese Gogish in the 60s. The idea is to compress a TIC nozzle linearly in the axial direction to a desired length. The compression causes the area ratio to grow faster which causes the flow to expand more rapidly compared to a TIC nozzle. As a consequence, right-running compression waves will propagate from the compressed contour into the flow field. If the compression is strong enough, the characteristic lines will coalesce and form a right-running oblique shock wave. If the shock wave lies near the nozzle wall, the pressure along the wall is increased, thus, increasing the nozzle thrust. The CTIC nozzle is used on the Japanese H-II launcher (the LE7A nozzle).

Thrust Optimized Contoured nozzles (TOC)

Another design procedure for rocket nozzles today is a modified version of the calculus of variables, developed by Rao [16]. The concept is; to find the exit area and nozzle contour which produces the optimum thrust for a given nozzle length and ambient pressure. The procedure can be divided into two steps. First, the kernel flow (TNKO) is generated with MOC, for a variety of θ_N and a given throat curvature r_{td}, see Figure 1.18. Then by using the calculus of variables for given design parameters (such as Mach number and area ratio or area ratio and nozzle length), the points P and N can be found by satisfying the following conditions;

1) Mass flow across PE equals the mass flow across NP.
2) The resulting nozzle gives the maximum thrust.

Once, P and N are found the kernel line NPE is fixed. The nozzle contour can then be generated by a series of parallel control surfaces $P'E'$, $P''E''$ from N to P (P' and P'' are fixed on the kernel line and E' and E'' are generated), see Figure 1.18. As the turning of the flow (contour) are more drastic compared to an ideal nozzle ($P = K$) it will induce weak compression waves in the region NPE, which will coalesce into a right running shock illustrated in the Mach number distribution, Figure 1.15(c).

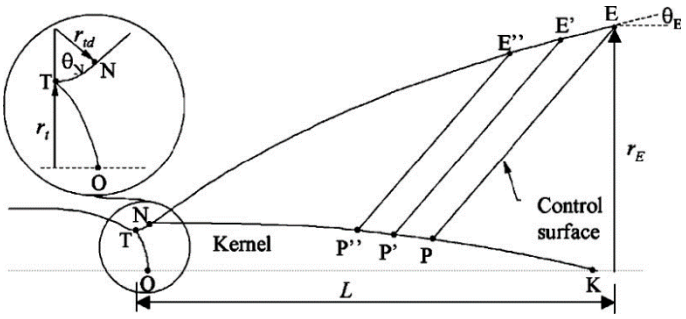

Figure 1.18: Thrust optimized nozzle contour, [13].

Parabolic bell nozzles (TOP)

Rao [16] also developed an approximated version of the TOC nozzles, the Parabolic bell nozzles (TOP). He approximated the TOC nozzles by a skewed parabolic geometry from the inflection point to the nozzle exit.

$$\left(\frac{r}{r_t} + b\frac{x}{r_r}\right)^2 + c\frac{x}{r_r} + d\frac{r}{r_r} + e = 0 \tag{1-35}$$

By freely varying the five independent variables, r_{td}, θ_N, L, r_E, and θ_N, which defines the nozzle contour, any parabolic nozzle can be generated. However, all of these parabolic nozzles are not a faithful approximation to a TOC, and will cause serious performance losses. Comparing the Mach number distribution of the approximated parabolic nozzle (TOP) in Figure 1.15(d) with the proposed TOC nozzle in Figure 1.15(c) it can be seen that the flow conditions along the wall are similar and that the performance is slightly less in the TOP nozzle, but there is a big difference in the shock pattern. The shock in the TOP nozzle is caused by the discontinuity in the contour at point N when the circular arc is continued with a parabolic curve. The discontinuity creates compression waves that coincide with an internal shock. This phenomenon is utilized in sea-level nozzles because it will affect the flow properties at the wall and increase the exit wall pressure, i.e. decrease the overexpansion. The gain to reduce the overexpansion will outweigh the slight loss in performance and that's why the Vulcain 2 (used on the Ariane 5 launcher) and SSME (Space Shuttle Main Engine) are designed as TOP nozzles.

1.4.2 Altitude Adaptative Nozzles

A critical comparison of performance losses shown in Table 1.3 reveals that the most significant improvements in nozzle performance for first-stage or SSTO engines can be achieved through the adaptation of nozzle exit pressures to the variations in ambient pressure during the launcher's ascent through the atmosphere. Various concepts have been investigated for this purpose and can be found in further details at [8].

CHAPTER 2. PHYSICAL PROPERTIES AND PHENOMENOLOGY OF FLOW SEPARATION IN OVER-EXPANDED NOZZLES

As discussed in Chapter 1, the flow issuing from the nozzle is only ideally expanded or adapted to the surrounding flow when the pressure of the surrounding atmosphere is equal to the pressure of the nozzle jet. During most of the operational time of a rocket engine, the supersonic discharge from the nozzle occurs under off-design conditions, where the nozzle exit pressure P_e differs from that of the atmosphere, P_a. It is customary to describe the conditions for off-design supersonic discharge by the degree of departure from the theoretical value, which is given as the ratio between the nozzle design exit pressure to the pressure in the surrounding medium.

$$n = P_e/P_a \tag{2-1}$$

An illustration of the exhaust plume patterns at under-expanded ($n > 1$), adapted ($n = 1$), and at over-expanded—but not separated flow—condition ($n < 1$) is given in Figure 1.8 from Chapter 1. The actual shape of the overexpansion shock pattern depends on the nozzle contour type (internal flow field) and degree of overexpansion as will be seen below.

This chapter will delve into the flow characteristics within over-expanded supersonic nozzles, highlighting the primary phenomenon governing this operational regime: Shock Wave Boundary Layer Interaction (SWBLI). Subsequently, we'll develop the most basic theory describing pressure evolution within the interaction region, known as Chapman's Free Interaction Theory (FIT). Finally, we'll examine the different behaviors encountered in conical over-expanded nozzles.

2.1 Exhaust plume patterns in over-expanded nozzle

Different shock patterns in the plume of over-expanded rocket nozzles have been observed: the classical Mach disc, Figure 2.1(a); the cap-shock pattern, Figure 2.1(b); and the apparent regular shock reflection at the centerline, Figure 2.1(c). In the case of axisymmetric flow, a pure regular reflection at the centerline is not possible. Instead, a very small normal shock exists at the centerline [18].

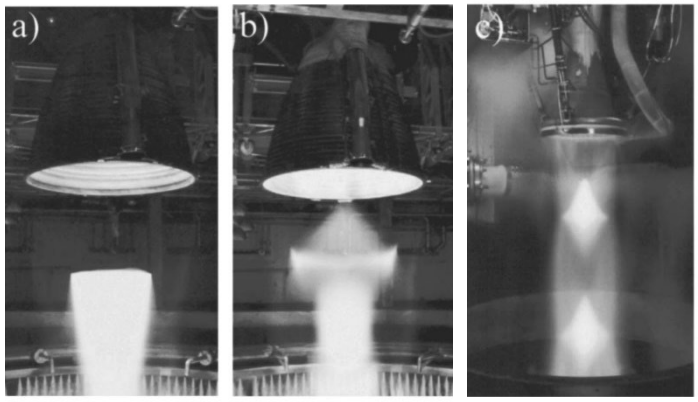

Figure 2.1 : Exhaust plume patterns. Overexpanded flow: (a) Vulcain, with classical Mach disc. (b) Vulcain, with cap-shock pattern. (c) RL10-A5, with apparent regular reflection.; Courtesy photos: SNECMA, CNES, NASA [13].

The observed luminous regions in the over-expanded jet of liquid propellant rocket nozzles at sea level express the thermal radiation of the gases taken to high temperatures as they suddenly decelerated when crossing intense shock waves.

In ideal and TIC nozzles, a transition between the Mach disc and the apparent regular shock reflection can be observed as the degree of overexpansion is decreased [13]. This is because a nozzle flow with a small overexpansion can adapt to the ambient pressure without forming a strong shock system (i.e., the Mach disc).

The difference between the Mach disc and cap-shock pattern is shown schematically in Figure 2.2. The cap-shock pattern is only observed in nozzles featuring an internal shock, such as TOC, TOP, and CTIC nozzles. Figure 2.1(b) proves the existence of the cap-shock pattern in the exhaust plume of the Vulcain nozzle, which has a parabolic contour [13]. This is the pattern that first appears at the nozzle exit during start-up. Upon increasing the combustion chamber pressure, the flow becomes less over-expanded. At some point, the internal shock intersects the centerline and a transition to a Mach disc pattern takes place, see Figure 2.1(a). Recent subscale experiments

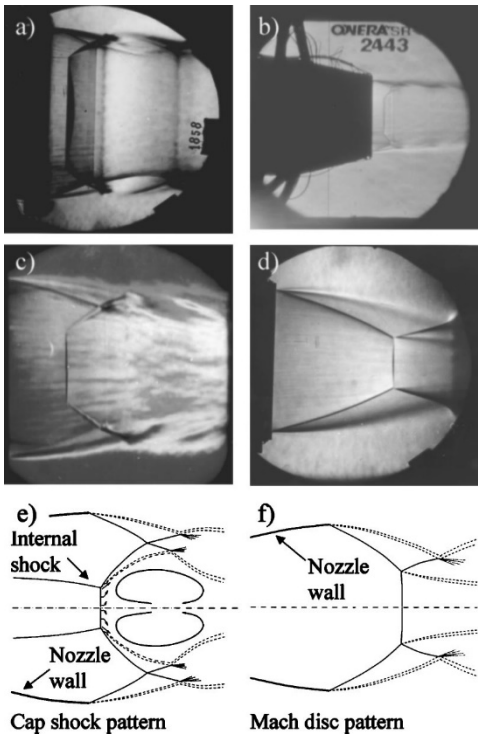

Figure 2.2 : Exhaust plume patterns for subscale nozzles. Parabolic nozzles with cap-shock pattern: (a) VOLVO S1. (b) TOP ONERA. (c) P6 TOP DLR. (d) TIC nozzle with Mach disc: VOLVO S6. (e) sketch of cap-shock pattern. (f) sketch of Mach disc pattern (Courtesy photos: DLR and ONERA). [13]

performed within the European FSCD group also confirmed the stable existence of the cap-shock pattern in the plume of parabolic subscale rocket nozzles [13].

Navier-Stokes calculations of the flow in the Vulcain nozzle [19], operating at expansion rates relatively close to the nominal rate on the ground, have indeed shown that two shock systems can exist (see Figure 2.3). The upper part of Figure 2.3 shows a classic Mach disk structure, formed by the singular reflection of the shock from the nozzle lip on the axis of symmetry. This Mach reflection is in no way disturbed by the internal focusing shock, the regular reflection of which we observe upstream of the Mach disk. However, the structure in the lower part of Figure 2.3 takes a completely different form, resulting from the interaction between the non-matching shock system and the internal focusing shock.

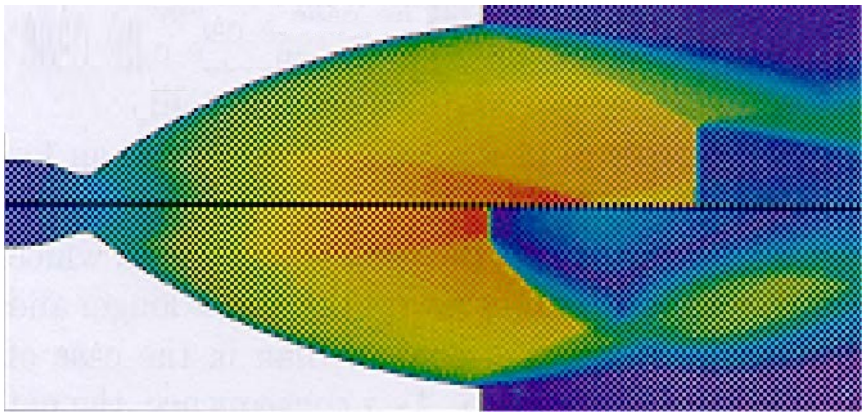

Figure 2.3 : Mach disk structure (top) and cap shock structure (bottom).
Navier-Stokes calculations for expansion rates close to the nominal rate
of the Vulcain engine [19].

The above-described shock patterns are not only an exhaust plume phenomenon; they also exist inside the nozzle at highly over-expanded flow conditions, when the jet is separated from the nozzle wall. As will be shown later in sections. 2.4.1 and 2.4.2, the different shock patterns determine the characteristics of the nozzle separation and side loads.

2.2 The nature of supersonic separation

From the unidimensional flow theory of a perfect fluid, the high over-expanded regime in nozzles was reflected by the apparition of a normal shock wave Figure 2.4(b). The pressure jump through the shock follows a discontinuous evolution which is exclusively dependent on the Mach number upstream.

In reality, the development of a boundary layer allows the pressure signal induced by the shock to propagate into the upstream direction through the subsonic sublayer. Thus, the pressure jump is felt upstream of the point where the shock would occur at the inviscid limit, Figure 2.4(a). Correlatively, thickening the subsonic zone due to the deceleration induced by the compression waves contributes to the enlargement and the weakness of the shock, which becomes generally oblique (Figure 2.4(c)).

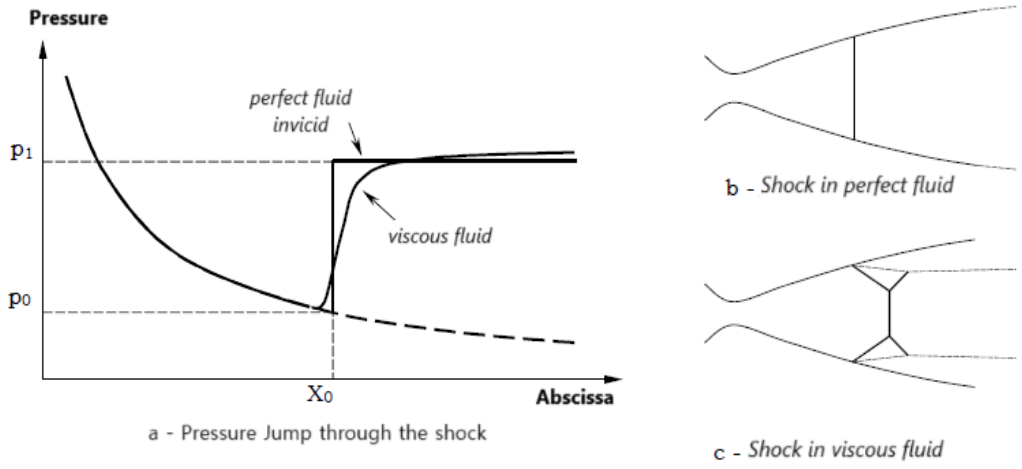

Figure 2.4 : Schematic representations of the over-expanded flow in a nozzle for perfect fluid and viscous fluid [20].

The supersonic nozzle flow separation is always the consequence of the interaction of sufficiently high adverse pressure gradient concentrated on an oblique shock with a boundary layer, namely, a shock wave boundary layer interaction. The word interaction means the reciprocity of the two mechanisms, on the one part, the action of pressure gradient which slows down and stiffens the boundary layer, and, on the other part, the growth of the boundary layer that results in a deviation of the supersonic flow. Thus, from this mechanism and interaction of viscous and inviscid regions, the pressure jump at the wall operates progressively from the upstream undisturbed flow until a downstream level in a distance called the interaction length [20].

2.2.1 Origin and length of the interaction

The origin I of the interaction is defined as the point where the evolution of the wall pressure deviates from that which would have been obtained without interaction (Figure 2.5). This point marks the beginning of the detachment process.

The interaction length L_S is defined as the distance between the origin I of the interaction and the average position S of the detachment point, i.e. $L_S = x_S - x_I$.

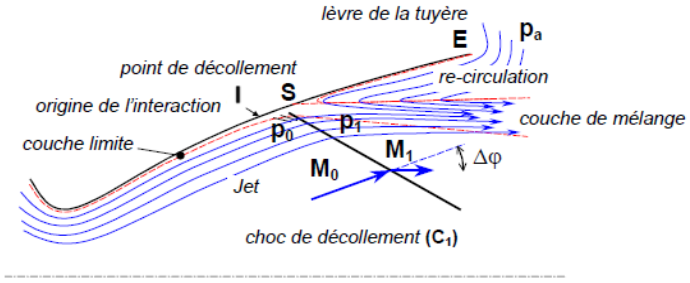

Figure 2.5 : Over-expanded nozzle with free shock separation [20].

2.3 Shock Wave Boundary Layer Interaction

When a supersonic flow is exposed to an adverse pressure gradient, it adapts to the higher-pressure level through a shock wave system. Separation occurs when the turbulent boundary layer cannot withstand the adverse gradient imposed upon it by the inviscid outer flow. Thus, flow separation in any supersonic flow is a process involving complex shock wave boundary layer interactions (SWBLI). SWBLI is an intrinsically unsteady and three-dimensional phenomenon, which may generate large fluctuating forces on the structure. In the following, we will first discuss observations and basic models for determining the mean pressure distribution in the separation zone and, thereafter, some observations concerning the fluctuating pressure field.

2.3.1 Basic interaction

Shock wave boundary layer interaction has been extensively studied in the last 50 years with the help of basic experiments [13]. Three nominally basic configurations involving interaction between a shock wave and a turbulent boundary layer in supersonic flows, which have been studied extensively, are represented schematically in Figure 2.6. In all of these cases, the incoming flow is a uniform stream along a flat plate.

The first and conceptually most simple configuration is the wedge (or ramp) flow. Here, a discontinuity in the wall direction is the origin of a shock wave through which the supersonic flow undergoes a deflection equal to the ramp angle α, Figure 2.6(a).

The second type is separation induced by a step of height h facing the incoming flow, Figure 2.6(b). Such an obstacle provokes separation of the flow at point S. The rapid pressure rise accompanying separation gives rise to a shock wave emanating from a place very close to the separation point S, and a separated zone develops between the separation point S and the step.

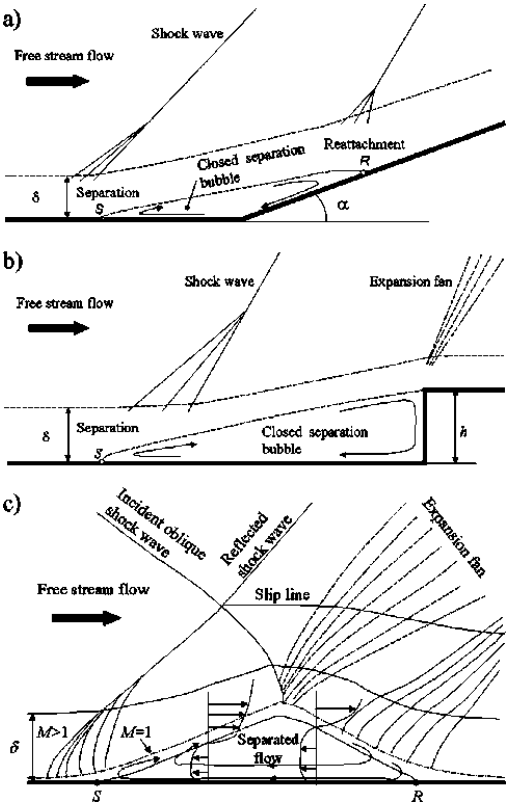

Figure 2.6 : Basic shock/boundary layer interactions in supersonic flow: (a) ramp flow, (b) step-induced separation, and (c) shock reflection (adopted from [53]) [13].

The third type is separation caused by the impingement of an oblique shock on a smooth wall, Figure 2.6(c). The incident shock causes a deflection of the incoming flow, and a reflected shock is formed as the downstream flow tends to become parallel to the wall.

Similarity in supersonic separations

It has been shown in many experiments that the upstream part of the shock/boundary layer interaction is nearly independent of the cause of separation, whether it is a solid obstacle or an incident shock wave [13]. In fact, the features of the static wall pressure for the above different experimental configurations are the same and are illustrated in Figure 2.7. The wall pressure has a steep rise shortly after the beginning of the interaction at I. The flow separates from the wall at

point S, located a distance L_s from I. If the separated flow scale is large enough, the wall pressure then gradually approaches a plateau with almost constant pressure, labeled plateau pressure P_p.

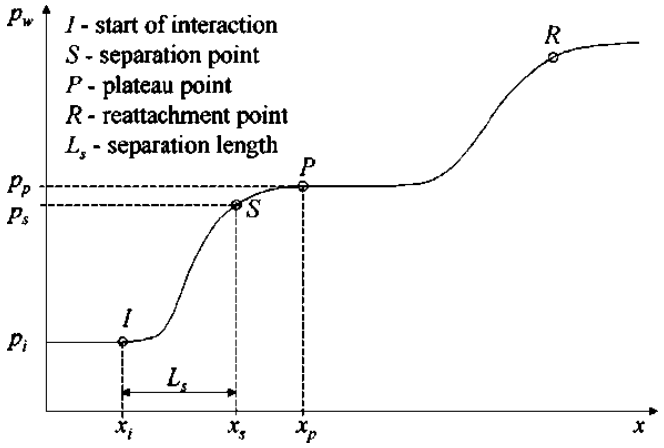

Figure 2.7 : Typical static wall pressure distribution observed in ramp, shock reflection and step flow (adopted from [42,54]) [13].

The extent of this plateau reflects the size of the closed recirculation bubble, and P_p thus corresponds to the wall pressure in the bubble. A second pressure rise can be observed as the reattachment point R is approached. These characteristics are independent of the downstream geometry, as already mentioned; everything happens as if the flow were entirely determined by its properties at the onset of the interaction.

However, experiments have shown three scenarios where we have found a disagreement with this rule of similarity:

- When the boundary layer is laminar or in a transitional state, the pressure in the detached region has a plateau level much lower than the recognized turbulent level.
- When the nozzles have a low divergence, we no longer observe a pressure plateau in the area after effective separation but a choppy evolution of the pressure.
- When the detachment process is close to the nozzle lip, the pressure plateau is not reached before the nozzle exit; this is referred to as the incipient separation.

The incipient Separation

In two-dimensional or axisymmetric mean flow, the notion of incipient separation is linked to the interaction region where the positive wall shear stress decreases abruptly until it is zero at a point. This notion arises from an average representation of the flow. In reality, the locally intermittent nature of the separation acts so that short appearances of separation can occur upstream of this

point where the wall friction coefficient is on average zero. Similarly, the incident flow can remain attached momentarily downstream of this point. In practice, two notions of incipient separation are defined [20]:

The ‘‘true’’ incipient separation point corresponds to the first appearance of a tiny separation bubble, while the ‘‘effective’’ incipient separation corresponds to a stage where the separation bubble has reached a size large enough to produce a significant change in the flow field. The latter is most important for practical applications.

Influence of the nature of the boundary layer

The first experimental and theoretical analysis of supersonic separation [21] highlighted the strong influence of the nature of the boundary layer on the wall pressure profile. Experimental studies undertaken at Onera [7] also showed this influence during separation. In addition to the laminar and turbulent cases, Carrière distinguished two other forms of pressure evolution corresponding to transitional cases (see Figure 2.8).

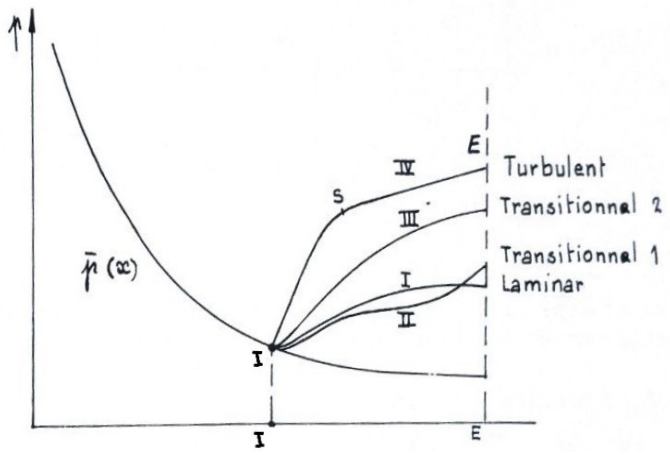

Figure 2.8 : Types of free separation in nozzles, laminar or turbulent [7].

Type I, II, and III curves are primarily relevant for small-scale tests at Reynolds numbers that are too low. We mention them here only as a reminder and to draw the attention of experimenters to the danger of error inherent in using older separation criteria, established before these distinctions were demonstrated [7].

On the scale of real engines, Reynolds numbers are always high enough that only turbulent type IV separations are observed.

Effect of the Reynolds Number

Based on the free interaction theory (that will be described in more detail just after), it can be shown that the critical pressure rise along the interaction length was dependent on the square root of the local friction coefficient at the interaction point *I* (see Eq. (2-18)). Following this result,

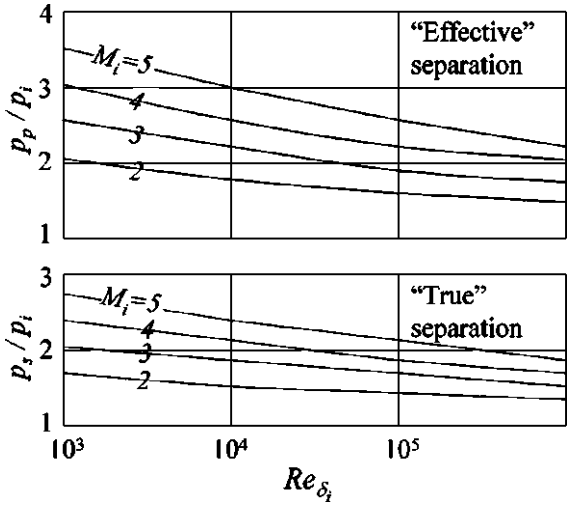

Figure 2.9 : Separation pressure obtained with the free interaction theory for uniform flow. ‘‘Effective separation’’: (point P); ‘‘True separation’’ (point S): (from [56]) [13].

Figure 2.9 shows how the separation pressure reflecting the two distinct incipient separation points varies with the Mach number.

From Figure 2.9, The general conclusion concerning the pressure rise at the separation obtained with the free interaction theory is that:

- The pressure rise increases when the Mach number is increased.
- The pressure rise decreases when the skin friction coefficient decreases (corresponding to an increase in the Reynolds number).

Both of these tendencies have been confirmed by experiments performed at low to moderate Reynolds numbers [13].

However, in several experiments performed at higher Reynolds numbers ($Re_{\delta i} > 10^5$), it has been observed that the pressure rise tends to become independent of the Reynolds number and even slightly increases with it. As an example, Zukoski [22] made a series of experiments on step flows at $Re_{\delta i} > 10^5$ with M_i varying between 1.4 and 6.0, and found that the pressure rise at high Reynolds numbers depended only on the upstream Mach number M_i as

$$\frac{P_s}{P_i} = 1 + 0.73\frac{M_i}{2}$$
$$\frac{P_p}{P_i} = 1 + \frac{M_i}{2} \qquad (2\text{-}2)$$

Hence, there appears to be a change of tendency in both Re and Mach number behavior as these parameters become large. An explanation for this behavior may be that, as the Reynolds number increases, the viscous sublayer occupies a smaller part of the entire boundary layer, and it becomes far thinner than the subsonic layer. These facts combine to make the pressure propagation at the high Reynolds number boundary layer an essentially inviscid process.

Viscous parameters also influence the separation length L_s. Experiments on ramp flows have shown that in turbulent flow, the separation length is very short, L_s/δ_i is of order 1, compared to the laminar case where the separation length is far larger than the incoming boundary layer thickness [13].

For turbulent flow, the influence of the Reynolds number on the separation length can be divided into two regions. For low or moderate Reynolds number ($Re_{\delta_i} < 10^5$), L_s increases with increasing Reynolds and Mach numbers (see Figure 2.10(a)), and agrees with the free interaction theory. Whereas at high Reynolds number ($Re_{\delta_i} > 10^5$), several investigators have found that the separation length tends to become independent of the Reynolds number and even to decrease with it, as indicated in Figure 2.10(b). This change in behavior at $Re_{\delta_i} \approx 10^5$ can be explained by the fact that the shape of the velocity profile is dependent on the Reynolds number and that a fuller velocity profile has a higher resistance against separation. At low to moderate Reynolds numbers, the velocity ‘‘fullness’’ initially decreases with increasing Reynolds numbers, but at higher Reynolds numbers the opposite behavior occurs (see, e.g., Johnson & Bushnell [23]).

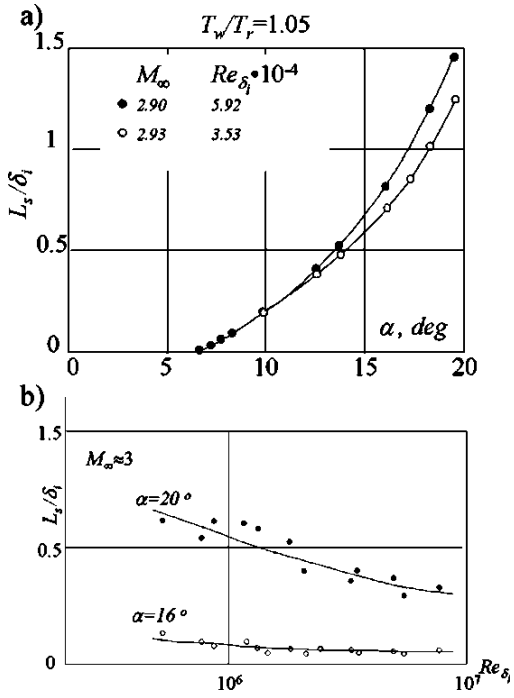

Figure 2.10 : Influence of Reynolds number and ramp angle on separation length (a) at low to moderate Re_{δ_i} , L_s/δ_i increases with Re (data from [43]), (b) at high Re_{δ_i} , L_s/δ_i decreases with Re (data from [39]) [13].

Effect of Wall Temperature

Another parameter that influences the separation length is the heat transfer. The cooling effect can be seen in Figure 2.11, where L_s is plotted versus T_w/T_r based on experimental data from Spaid and Frishett [24]. $\widetilde{L_s}$ is the ratio between L_s/δ_i when heat transfer is present and L_s/δ_i with adiabatic flow evaluated at the same Re_{δ_i}.

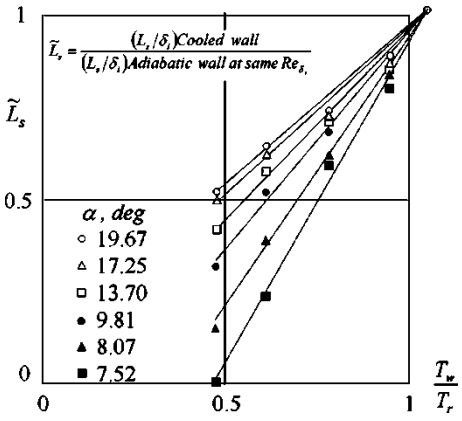

Figure 2.11 : Influence of wall cooling on the separation length in a ramp flow. (data from [43]) [13].

As indicated in the figure, wall cooling decreases the separation distance. This reduction of L_s with decreasing wall temperature can be explained with the help of the free interaction theory. When reducing T_w/T_r (T_r is the wall recovery temperature), the skin friction coefficient will increase and this provokes a decrease of L_s. Another interpretation of the reduction of L_s is that an overall contraction of the interaction domain is obtained due to a thinning of the subsonic layer, as the temperature level and thus the speed of sound near the wall become lower.

Factors influencing the evolution of pressure in the overlap or detachment zone

The pressure recovery zone is the region from downstream of the shock wave boundary layer interaction where the pressure has undergone a strong increase, to the nozzle outlet where the pressure is close to the ambient external pressure. In cases of over-expanded nozzles where there is no free separation, the term pressure recovery may be preferred to that of separation.

The geometry of the divergent is a particularly influential factor on the pressure in the detached zone as has been highlighted by Onera experiments [20] carried out in ideal profiled nozzles and nozzles with a conical divergent.

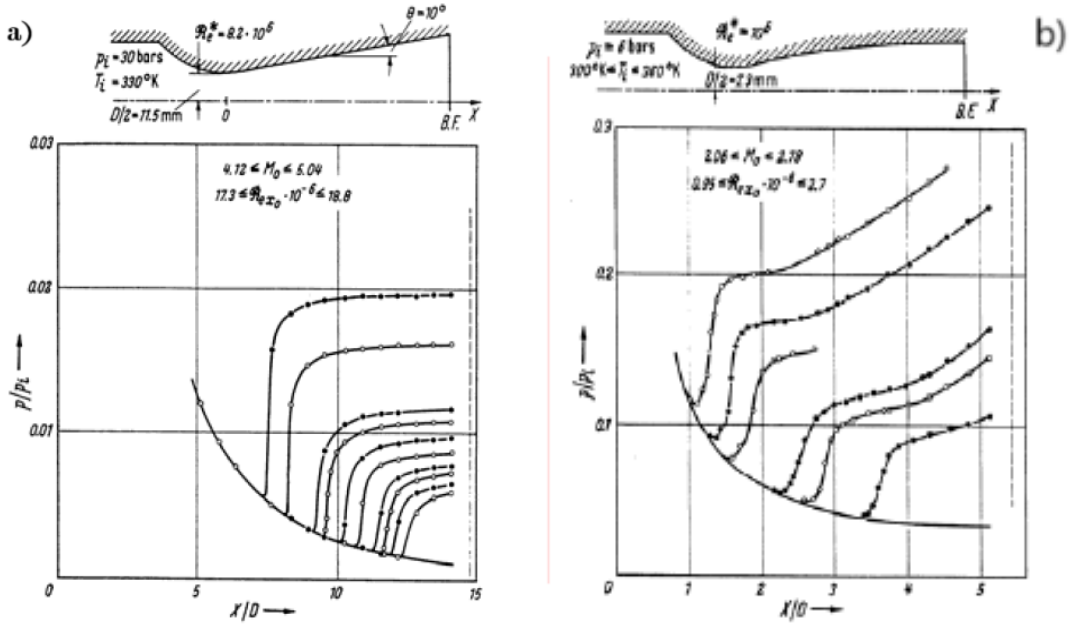

Figure 2.12 : Wall pressure evolution in the detached zone; a)- conical nozzle, b)- ideal bell nozzle, [20].

The pressure profiles obtained in the conical nozzles, Figure 2.12(a), show a very clearly defined pressure plateau. On the other hand, in the ideal nozzles profiled in Figure 2.12(b), there is a significant positive pressure gradient downstream of the separation. As suggested by Carrière et al. [20] the evolution of the pressure after separation is linked to the confinement of the separated region in which the recirculation takes place. This confinement parameter is determined by the proximity of the external boundary of the mixing layer to the wall of the divergent as indicated by Herbert and Herd [25] through the diagrams in Figure 2.13.

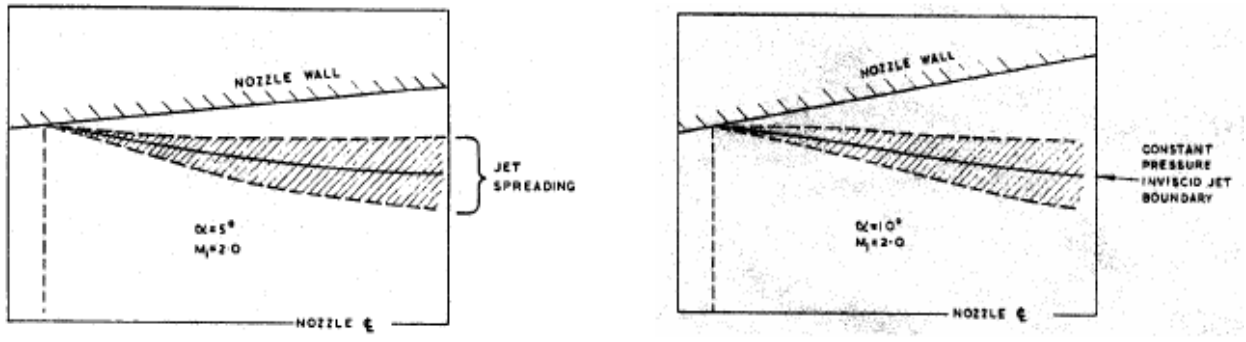

Figure 2.13 : Separated jet boundary, calculated by the MOC method [20].

Thus, when the separation point is located very far upstream of the outlet, the mixing layer develops over a large distance and its expansion means that it will be very close to the wall of the diverging nozzle. In nozzles with low divergence, the flaring of the sheared layer induces a narrow volume in which the reflux must be organized. A smaller volume of the separated zone will cause higher reflux velocities as well as a faster evolution of the separated pressure. The role played by the geometry of the volume in which the fluid recirculation evolves on the jet fluctuations has also been highlighted by Lawrence [20].

Another consequence of the proximity of the detached shear layer to the wall, which can be suggested here, would be an intermittent reattachment process; the phenomenon would be driven by the transport of large-scale coherent structures in the mixing layer that would intermittently impact the diverging wall. This intermittent reattachment would be a source of increased pressure fluctuations, inducing an increase in the measured mean pressure. This idea of "intermittent reattachment" could explain the appearance of the mean pressure profiles obtained in the Hunter Mach 2 nozzle [26] in a range of intermediate expansion ratios (Figure 2.14).

For the lowest expansion rates ($NPR \leq 1.4$) the study [26] specifies that there is no separation, and beyond $NPR = 2$ there is free separation of the jet. Between the two ranges of expansion rates, the author notes that the profiles present an inflection but do not conclude on a physical interpretation, the Strioscopic visualizations being moreover very difficult to read [26].

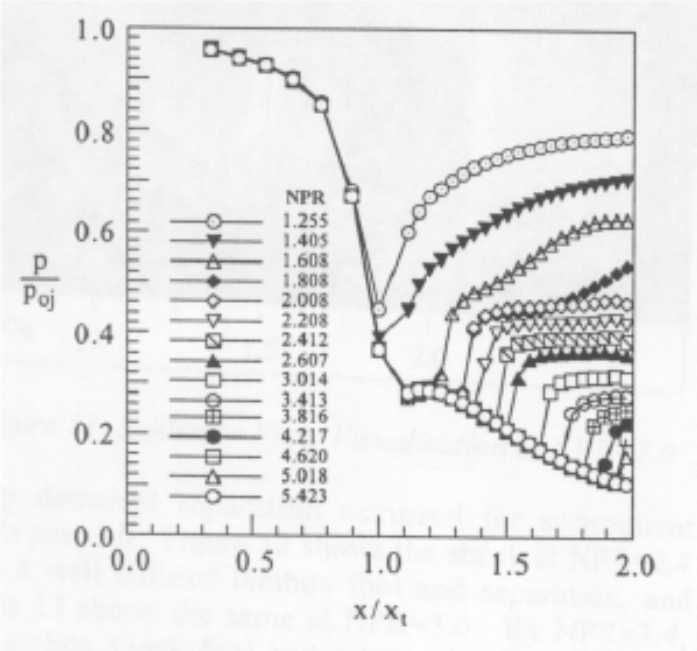

Figure 2.14 : Wall pressure profiles in Mach 2 planar nozzle with half angle of 11°, over-expanded regime [20].

2.3.2 The Free interaction theory

The free interaction theory is based on the notion of free separation. It was Mager [20] who described separations as "free" when the flow downstream of the separation itself is free to adjust in a direction resulting from the shock/boundary layer interaction process. This condition, according to Mager, is respected when reattachment does not occur (case of over-expanded nozzles with free jet separation) or only occurs quite far downstream of the separation (case of rising steps sufficiently high relative to the boundary layer, or of a high-intensity shock reflection).

The striking feature of this free or extended separation is that the wall pressure profiles present a well-marked plateau just after the sudden rise in pressure when crossing the induced shock. The term free separation is no longer really appropriate when a reattachment process occurs quickly after the detachment.

As we have seen earlier, the correspondent pressure evolution is divided into two distinct regions:

- The branch IS, which is called by the Chapman region of the free separation [27], as its shape is independent of the condition operating downstream of S. For example, if we modify simultaneously the profile SE of the nozzle and we adjust P_a such that I is maintained fix, this branch can, at first approximation, be considered invariant.
- The branch SE, in contrast, is highly dependent on the downstream conditions and notably on the form of the nozzle profile.

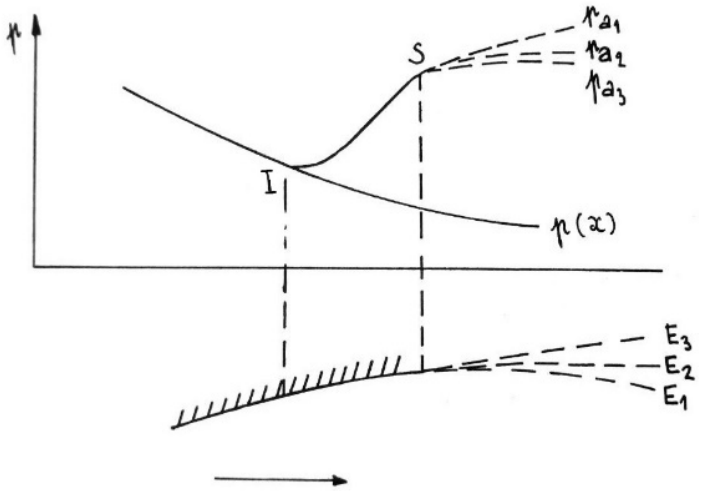

This observation of a general form of the pressure distribution over the interaction region led Chapman et al. [27] to formulate the concept of free interaction. This theory is applicable for two-dimensional uniform flow before the separation (branch IS), it is also valuable for the laminar as well as turbulent cases.

Let's assume that the pressure is uniform at each abscissa x within the boundary layer, and in the separated region, we therefore have $P = P(x)$

If $\delta^*(x)$ represents the displacement thickness of the boundary layer, and ϕ the angle of deflection of the external flow under the displacement effect, we have

$$\phi = \frac{d\delta^*}{dx} \tag{2-3}$$

The linearized PRANDTL-MEYER compression law, applicable to this flow if remains small enough, therefore allows us to write:

$$\frac{P(x) - P_i}{q_i} = \frac{2}{\beta_i}\frac{d\delta^*}{dx} \tag{2-4}$$

Where

$$\begin{aligned} q_i &= \frac{1}{2}\rho_i V_i^2 \\ \beta_i &= \sqrt{M_i^2 - 1} \end{aligned} \tag{2-5}$$

Let us assume, as the experiment suggests, that the phenomenon obeys to similarity law over the length l. If δ_i^* is the displacement thickness at the position I, we have then

$$\frac{d\delta^*}{dx} = \frac{\delta_i^*}{l} \cdot f_1(s) \tag{2-6}$$

Where $s = (x - x_i)/l$, and f_1 is a nondimensional function characterizing the outer streamline deflection.

We can therefore write the variation law of $P(x)$ in the form:

$$\frac{P(x) - P_i}{q_i} = \frac{2}{\beta_i} \cdot \frac{\delta_i^*}{l} \cdot f_1(s) \tag{2-7}$$

Now, let us consider further the momentum equation of the boundary layer:

$$\rho u\frac{\partial u}{\partial x} + \rho v\frac{\partial u}{\partial x} = -\frac{dP}{dx} + \frac{\partial \tau}{\partial y} \tag{2-8}$$

Written at the wall, where $u = v = 0$, it results in:

$$\frac{dP}{dx} = \left(\frac{\partial \tau}{\partial y}\right)_w \tag{2-9}$$

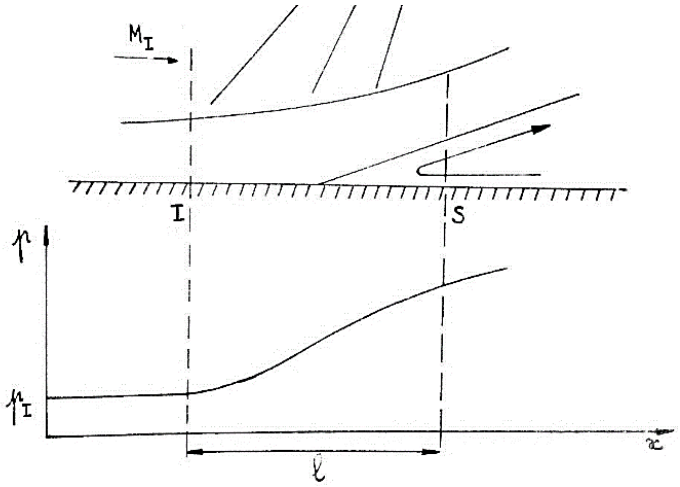

Let us integrate from $x = x_i$ in the IS region, and we obtain:

$$P(x) - P_i = \int_0^x \left(\frac{\partial \tau}{\partial y}\right)_w dx \tag{2-10}$$

Introducing the appropriate reference values by considering the hypothesis of similitude, the equation becomes:

$$\frac{P(x) - P_i}{q_i} = \frac{l\ \tau_{w,i}}{q_i\ \delta_i^*} \int_0^s \left(\frac{\partial \left(\frac{\tau}{\tau_{w,i}}\right)}{\partial \left(\frac{y}{\delta_i^*}\right)} \right) ds \tag{2-11}$$

Where $\tau_{w,i}$ is the partial friction at I, expressed using the friction coefficient, we write $\tau_{w,i} = q_i \cdot c_{f,i}$.

The integral, by hypothesis, is uniquely dependent on s, thus we get:

$$\frac{P(x) - P_i}{q_i} = \frac{l\ c_{f,i}}{\delta_i^*} \cdot f_2(s) \tag{2-12}$$

Where f_2 is a function, similar to f_1, which characterizes the pressure rise.

Multiplying members by the member (2-7) and (2-12), we eliminate l/δ_i^* and we obtain:

$$F(s) = \sqrt{f_1(s) \cdot f_2(s)} = \frac{P(x) - P_i}{q_i} \cdot \sqrt{\frac{\beta_i}{2 \cdot c_{f,i}}} \tag{2-13}$$

Or

$$F(s) = \frac{P(x) - P_i}{q_i} \cdot \sqrt{\frac{\sqrt{M_i^2 - 1}}{2 \cdot c_{f,i}}} \tag{2-14}$$

The function $F(s)$ is assumed to be a universal function, independent of Mach number and Reynolds number, to be determined from experiments [13]. Figure 2.15 shows the generalized wall pressure correlation function $F(s)$ obtained by Erdos and Pallone [28]. The axial distance from the onset of the interaction has been normalized with the separation length, i.e., $l = L_s = x_s - x_i$. In the original work by Erdos and Pallone, the distance to the pressure plateau of the extended separated flow was used as the characteristic length scale, i.e., $l = L_p = x_p - x_i$. From the figure, the following particular values of F can be found: $F_s = F(s = 1) = 4.22$ at the separation point (S), and $F_p = F(s = 4) = 6.00$ at the plateau point (P) [13].

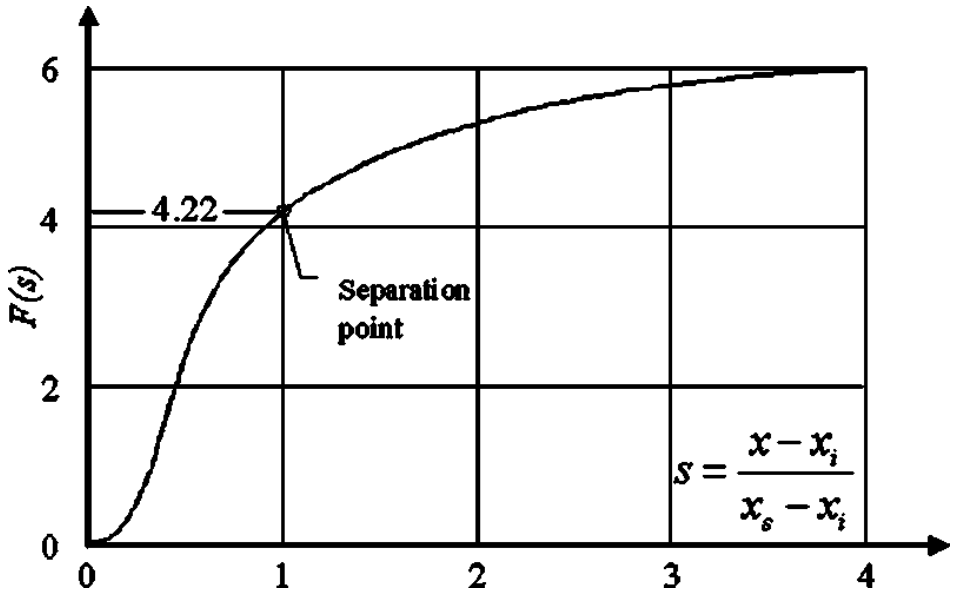

Figure 2.15 : Generalized wall pressure correlation function F(s) for uniform turbulent flow, by Erdos and Pallone [28].

Chapman also showed that the characteristic length l could be expressed as

$$\frac{l}{\delta_i^*} = \sqrt{\frac{2}{c_{f,i}\sqrt{M_i^2 - 1}}}\sqrt{\frac{f_1(s)}{f_2(s)}} \tag{2-15}$$

At the separation point S ($s = 1$), this relation can be evaluated as,

$$\frac{l}{\delta_i^*} = k\sqrt{\frac{2}{c_{f,i}\sqrt{M_i^2 - 1}}} \tag{2-16}$$

Here, k is the value of $\sqrt{f_1/f_2}$ evaluated at $s = 1$. From different experiments, an average value of $k = 0.37$ has been obtained [13]. However, the experimental data have a significant scatter around this value; $k = 0.27 - 0.57$ has been observed, presumably due to the difficulty of accurately determining the separation length, which in turbulent flows is very short—typically a few boundary layer thicknesses.

Separation Criteria Based on Free Interaction Theory

Supersonic separation criteria refer to the conditions under which a supersonic flow separates from a surface. Two theories of supersonic boundary layer separation, developed in the 1950s, have given rise to a multitude of empirical separation criteria. One is the integral method of Reshotko and Tucker [20], which was developed to predict the effect of a sudden pressure change on a supersonic turbulent boundary layer with a Mach number less than 3. This analysis predicts the onset of shock wave-induced separation for a Mach number ratio equal to:

$$M_1/M_0 = 0.762 \tag{2-17}$$

The other falls within the framework of the present theory; a more elaborate list can be found at [20].

The free interaction theory can be used to establish separation criteria for supersonic flow. The best known is the type of criteria first proposed by Erdos and Pallone [28] in 1962. They determined the critical pressure rise between the pressure P_r at location $s = r$ and P_i $(s = 0)$ by assuming that the separation occurs when the pressure jump P_r $/P_i$ is

$$\frac{P_r}{P_i} = 1 + F_r \gamma M_i^2 \sqrt{\frac{c_{f,i}}{2\sqrt{M_i^2 - 2}}} \tag{2-18}$$

This equation is obtained by rewriting Eq. (2-14) and using the fact that the dynamic pressure can be written as

$$q_i = \frac{1}{2}\rho_i u_i^2 = \frac{1}{2} P_i \gamma M_i^2 \tag{2-19}$$

The pressure rise, corresponding to ‘‘true’’ incipient separation (point S in Figure 2.7) is obtained with $F_r = F_s = 4.22$, while the ‘‘effective’’ incipient separation (point P in Figure 2.7) is obtained with $F_r = F_p = 6.0$. The ‘‘true’’ incipient separation point ($F_r = 4.22$) corresponds to the first

appearance of a tiny separation bubble, while the ‘‘effective’’ incipient separation ($F_r = 6.0$) corresponds to a stage where the separation bubble has reached a size large enough to produce a significant change in the flow field. The latter (which is the value used by Erdos and Pallone) is most important for practical applications.

Generalization of the free interaction criteria for a non-uniform flow

The flow separation in nozzles doesn't follow exactly the conditions of Chapman; On the one hand, the flow is axisymmetric, on the other, it exist generally a high favorable pressure gradient which results from nozzles expansion waves, they superpose between I and S to the phenomenon of separation. If the length IS of the wall filling these waves was short, then the criteria of Chapman would be applicable. However, experience has shown that usually, this distance is far from being negligible. This resulted in great disagreement between the Chapman criteria and experiments. Research undertaken at Onera has elaborated a new method of calculation of these phenomena see Carrière et al. [29], [7].

2.3.3 Unsteadiness and Three-Dimensional Effects

In the previous section, we only looked at the mean properties of shock-induced separation. The unsteady pressure behavior has been the topic of a number large of studies, some of which are found at [13].

2.4 Configurations of flow separation phenomena in over-expanded nozzles

A flow exposed to an adverse pressure gradient of sufficient strength can cause the boundary layer to separate from the wall. In the previous section, we examined the influence of such adverse pressure gradients generated by obstacles. A similar condition occurs when a nozzle is operating in an over-expanded condition, i.e., $n < 1$ (cf. Eq. (2-1)). In rocket engines, this situation is faced in off-design operations. It also occurs during start transients, shut-off transients, or engine throttling modes.

Recent research has made it clear that two different separation patterns exist, the classical free shock separation, and the restricted shock separation, in the following denoted by their acronyms FSS and RSS, respectively. Figure 2.16 shows schematic figures for the two separation patterns together with the definition of their characteristic points. In the following, these two regimes will be described in more detail.

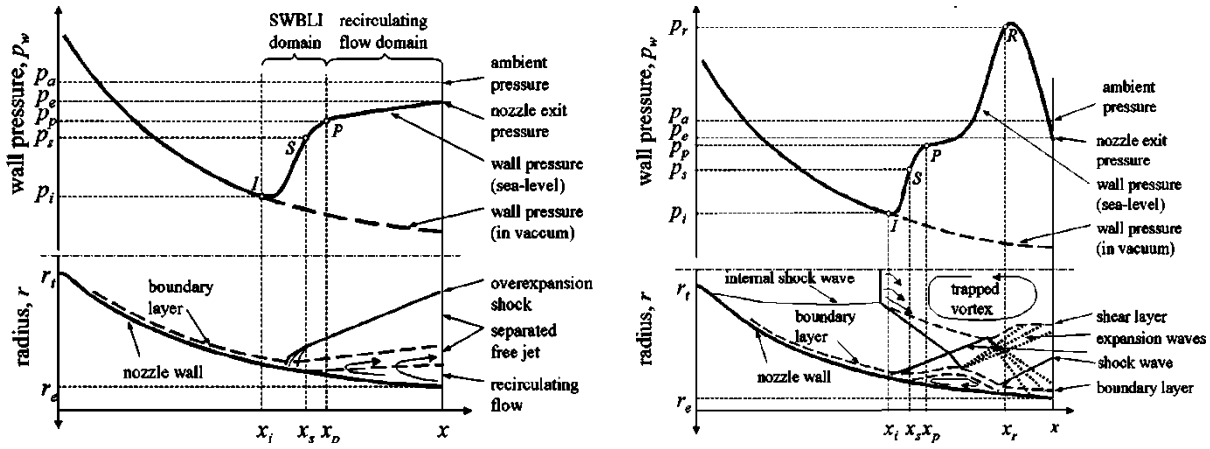

Figure 2.16 : Phenomenological sketch of free shock separation (FSS, top), and restricted shock separation (RSS, bottom) [13].

2.4.1 Free Shock Separation (FSS)

In the free shock separation case, the over-expanded nozzle flow fully separates from the wall. The resulting streamwise wall pressure evolution is mainly governed by the physics of shock wave boundary layer interactions occurring in any supersonic flow separation, cf. Section 2.3. However, in contrast to obstacle-induced separation, the separation location is not fixed by the geometrical properties of the test configuration but results mainly from the degree of overexpansion. As the degree of overexpansion is reduced, i.e., n is increased toward one, the separation shock moves out of the nozzle.

Based on the static wall pressure distribution, the flow can be divided into three regions:

- The non-perturbated region is similar to an attached full-flowing nozzle.
- The separation region is also referred to as the interaction or the intermittent region.
- The last portion of the nozzle, where the flow is fully separated, is referred to as the recirculation zone.

Pressure Fluctuations and Side Loads

Looking at the pressure fluctuations, we find distinct characteristics for the separation zone, as compared to the attached flow upstream of it, or the recirculation zone downstream of it.

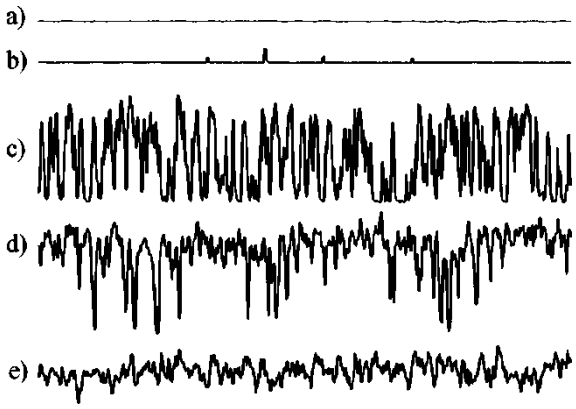

Figure 2.17 : Pressure signals at different positions through the interaction region in the VOLVO S7 short nozzle. Measurements made during down ramping of P_0. (cf. [56,76]). (a): attached flow; (b), (c), and (d): separation zone; (e): recirculation zone downstream of separation, [13].

An example is given in Figure 2.17, which shows fluctuating wall pressure signals recorded at different positions through the interaction region in the truncated VOLVO S7 nozzle [13]. In the attached zones (signal(a)), the pressure fluctuations are quite small. They are due only to the turbulent fluctuations of the attached boundary layer upstream. Signals (b)–(d) are from the separation zone. The large fluctuations are caused by the intermittent motion of the separation shock, causing an oscillation between the two levels P_i upstream of the separation shock, and P_p at the beginning of the recirculation zone—depending on the instantaneous position of the separation shock relative to the pressure sensor. Signal (e) shows the pressure fluctuations caused by the shear layer of the separated free jet in the recirculation downstream of separation. These fluctuations are low compared to the separation zone, yet substantially higher than in the attached flow.

One should keep in mind that the oscillation of the separation front reflects a time-dependent motion of the nozzle jet. It is not a local wall phenomenon but affects the entire flow field downstream of separation. This is reflected in the relatively high fluctuation level in the recirculation zone as compared to the attached flow region (see Figures 2.17(e) and 2.17(a), respectively). This is a feature particular to internal flow separation in nozzles, and it also explains why a correlation between the pressures at different circumferential positions has to exist.

This circumferential variation of the pressure is not necessarily axisymmetric, and may hence produce side forces perpendicular to the nozzle axis. Figure 2.18 shows side loads measured in the VOLVO S6 short nozzle during a sequence of slow up- and down-ramping of the chamber pressure (i.e., the different times correspond to different operational conditions). The side load level is largest in the range of $n = 0.05$ to $n = 0.25$.

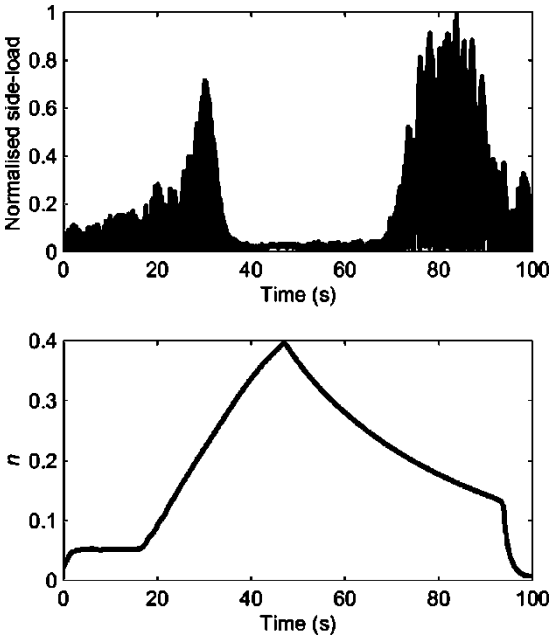

Figure 2.18 : Side loads in a truncated ideal nozzle (VOLVO S6) at free shock condition (from [77]) [13].

2.4.2 Restricted Shock Separation (RSS)

During cold-flow subscale tests for the J-2S engine development in the early 70s, a previously unknown flow separation pattern was observed at strongly over-expanded operating conditions [30]. In this flow regime, which only occurred at certain pressure ratios, the pressure downstream of the separation point showed an irregular behavior and partly reached values above the ambient pressure. This is due to a reattachment of the separated flow to the nozzle wall, inducing a pattern of alternating shocks and expansion waves along the wall (see Figure 2.16). Due to the short-separated region, this flow regime was called restricted shock separation (RSS) by Nave and Coffey [30]. The separation characteristics of RSS, as observed in the J-2S nozzle, and recently confirmed for subscale and full-scale rocket nozzles, are described in the following [13].

FSS-RSS Transition

Figure 2.20 shows CFD calculations visualizing the flow field (Mach number contours) during a start-up sequence of the VOLVO S1.

During the start-up of the nozzle flow, featuring initially a pure free shock separation, a transition from FSS to RSS occurs at a well-defined pressure ratio [13]. Figure 2.19 shows some typical measured steady-state wall pressure profiles in the VOLVO S1 nozzle during start-up, as n is increased toward one. The wall pressure profiles indicate FSS for $n < 0.14$ and RSS for $n > 0.14$ (cf. Fig. 2.16). The transition of the flow separation pattern from FSS to RSS takes place at $n \approx 0.14$. This can also be seen in Figure 2.20: at $n < 0.14$, the exhaust jet is seen to occupy only a fraction of the nozzle exit, whereas at $n > 0.14$ the exhaust is attached to the nozzle wall.

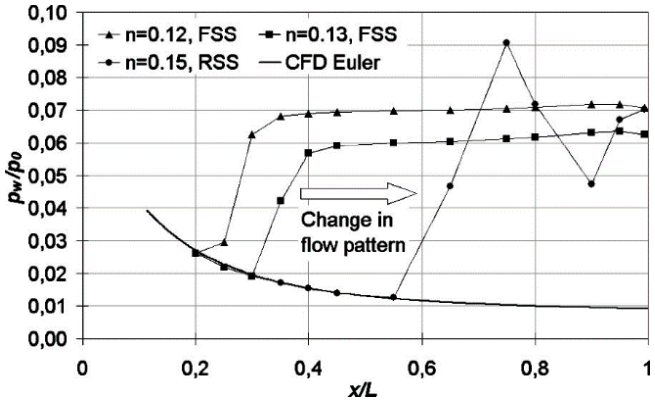

Figure 2.19 : Wall pressure profiles in the VOLVO S1 nozzle during start-up, (from [56]), [13].

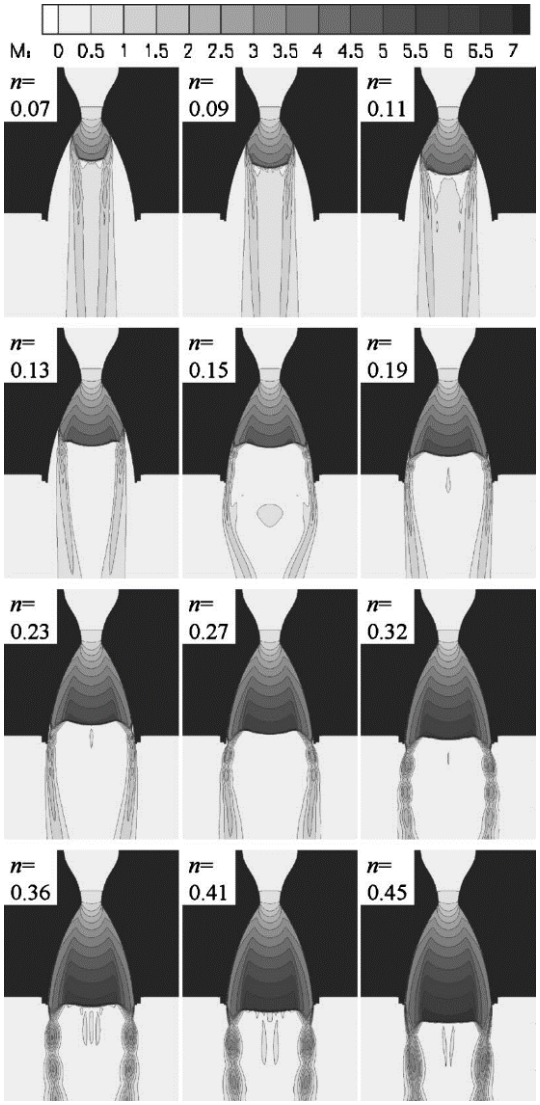

Figure 2.20 : Calculated Mach number contours in the VOLVO S1 nozzle at different operational conditions, n = 0.07– 0.45, (from [56]), [13].

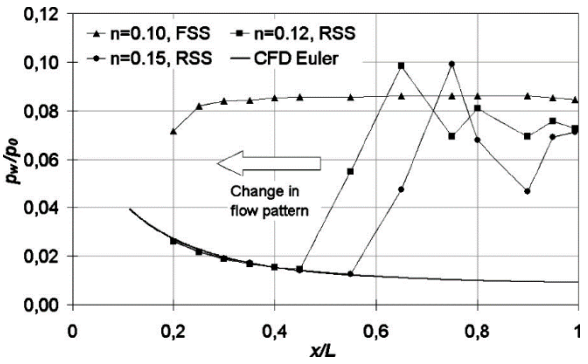

Figure 2.21 : Wall pressure profiles in the VOLVO S1 nozzle during shutdown, (from [56]), [13].

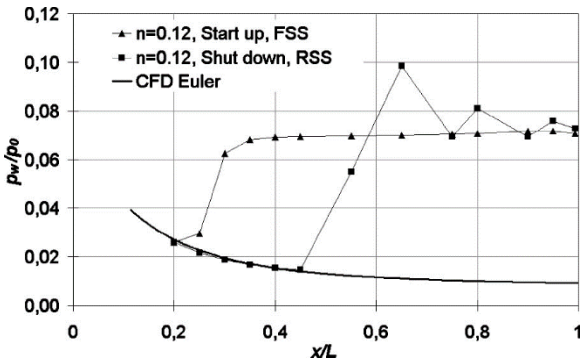

Figure 2.22 : Comparison between wall pressure profile at FSS and RSS condition at n = 0.12, (from [56]), [13].

The wall pressure distributions measured during shutdown are shown in Figure 2.21. Here, it can be seen that the transition between RSS and FSS occurs at a lower chamber pressure, $n = 0.11$, indicating that there is a hysteresis effect.

Figure 2.22 compares the wall pressure profiles at FSS and RSS conditions at a pressure ratio of $n = 0.12$. As can be seen, the wall pressure distribution is quite different for the two cases. The main difference is that the RSS separation line is located much further downstream of the FSS separation line. The reason is that when the jet attaches to the wall a closed recirculation zone is formed, with static pressures significantly below the ambient pressure level. Therefore, when an FSS-RSS or RSS-FSS transition takes place, the separation line jumps.

The End Effect

Upon further increasing n, the closed recirculation zone is pushed toward the nozzle exit. Finally, the reattachment point reaches the nozzle exit, and the recirculation zone opens to the ambient flow. This is connected with a pressure increase in the recirculation zone behind the separation shock that pushes the separation point back upstream. The recirculation zone then closes again, connected with a drop in static pressure, which results again in a downstream movement of the separation point. A pulsating process is observed, connected with the opening and closing of the separation zone. This retransition from RSS back to FSS is referred to in the literature as the end effect [13] and occurs in the VOLVO S1 nozzle at $n \approx 0.25$ [13]. The end effect is also observed during shutdown, at the same degree of overexpansion as during start-up, however in this case the transition is from FSS to RSS.

Side Loads Generated by FSS-RSS Transition

Östlund [13] was the first to show, based on analysis of the VOLVO S1 test, that these transitions between separation patterns are associated with distinct side load peaks, which occur impulsively and are characterized by high amplitude. Figure 2.23 shows a time record of the measured side load torque in the VOLVO S1 nozzle during a start-up and shutdown process. In each case, two distinct load peaks can be identified, one at $n = 0.14$ and one at 0.11 for start-up and shutdown, respectively, indicating an FSS-RSS transition, and one at $n = 0.25$, where the ‘‘end effect’’ takes place.

The above observations and conclusions by Östlund [13] were followed up by intensive research both within and outside Europe. Further subscale experiments were performed within different FSCD test campaigns [13] as well as recent Japanese experiments [13], which confirmed this mechanism for TOP and CTIC nozzles (both of which have internal shocks). In addition, a reevaluation of the test results of the Vulcain 1 engine confirmed this mechanism as the key driver for side loads during both start-up and shutdown [13].

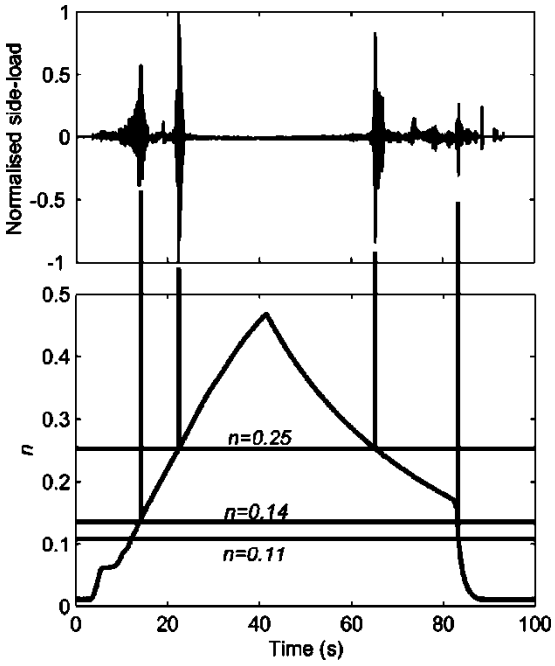

Figure 2.23 : Side loads due to transition in separation pattern in the VOLVO S1 nozzle (from [32]) [13].

Physical Mechanisms Driving the FSS-RSS Transition

The theory of reattached flow in the J-2S subscale nozzle was first confirmed by numerical simulations of Chen et al. in 1994 [13]. In addition, their calculations revealed a trapped vortex behind the central normal shock, but they did not provide any explanation for the generation of such a flow structure.

Later, Nasuti and Onofri stressed the role played by the centerline vortex on the separation pattern and side load generation [13]. The centerline vortex acts as an obstruction for the exhausting jet,

which is thereby pushed toward the wall. As a consequence, a radial flow component is generated that tends to reattach the separated region, thus switching the flow from FSS to RSS.

Frey and Hagemann have given another explanation of the reattached flow, based upon experimental observations and numerical simulation [13]. According to their results, the key driver for the transition from FSS to RSS and vice versa is the specific cap-shock pattern. Thus, a transition from FSS to RSS can only occur in nozzles featuring an internal shock. According to their findings, the cap-shock pattern results from the interference of the separation shock with the inverse Mach reflection of the weak internal shock at the centerline [13]. A key feature of this inverse Mach reflection is the trapped vortex downstream of it, driven by the curved shock structure upstream of it, which generates a certain vorticity in the flow [13]. Thus, the vortex would be a result of the curved shock structure, which is partially in contrast to the explanation given by Nasuti and Onofri, which also includes an effect of flow gradients upstream. Further experimental and numerical verification is planned to finally reach a conclusion with respect to this interesting vortex phenomenon.

An interesting point is that both the hypotheses of Nasuti and Onofri and Frey and Hagemann identify the curved cap-shock profile as a driver for the transition from FSS to RSS, in agreement with what is experimentally proven in [13].

2.5 Over-expanded operation of Conical Nozzles

The performance of fully expanded and under-expanded conical exhaust nozzles, having conventional divergence angles, can be described adequately based on one-dimensional theory. Even though a one-dimensional model of nozzle flow can be postulated for over-expanded nozzles, it is now well-known that it generally does not correspond to reality. Whereas for the one-dimensional model, it is assumed that the boundary condition of ambient pressure at the nozzle exit is satisfied by normal shock deceleration followed by subsonic compression within the nozzle (see Chapter 1), in actuality the flow may attain ambient pressure as the result of oblique shock compression accompanied by flow separation from the wall [31].

Over-expanded conical nozzle performance may be divided into the following five distinct regimes, in order of increasing nozzle pressure ratio (NPR) [31]:

1. Essentially one-dimensional flow with a normal shock downstream of the throat. This condition occurs for pressure ratios slightly above those required to choke the nozzle.
2. Unstable flow with oblique shock boundary layer separation. The shock pattern is asymmetric and unsteady.
3. Stable flow with symmetric oblique shock boundary layer separation around the nozzle circumference. As the pressure ratio is raised, the separation point moves toward the nozzle exit. This regime exists from a nozzle pressure ratio sufficient to establish stable flow until the pressure ratio is raised to the point where separation occurs in the immediate proximity of the nozzle exit plane.
4. Flow with oblique shock boundary layer interaction within the nozzle but in the immediate proximity of the nozzle exit plane. This regime exists until the pressure ratio is sufficiently high to expel the oblique shock pattern from the nozzle.
5. Undisturbed flow in the nozzle with oblique shocks initiating in the nozzle exit plane. The shocks become weaker as the nozzle pressure ratio is raised and disappear when the full expansion pressure ratio is reached.

For rocket motors and jet engines, nozzle geometry, and operating pressure are usually such that only regimes 3-5 are of interest to the engine designer. Nozzle performance in regime 5 can be estimated adequately based on a one-dimensional model while correcting for velocity deviations from axial in the exit plane (cf. Eq. (1-33)). Regime 4 covers only a very small range of pressure ratios. Since the shock wave boundary layer interaction is restricted to the immediate vicinity of the nozzle exit plane, nozzle performance, except for base drag effects, can be estimated as for regime 5. Estimating nozzle performance for regime 3 requires knowledge of the location of the boundary layer separation.

Several experimental investigations on conical and straight-walled two-dimensional nozzles have been carried out to determine the conditions for which flow separation takes place and the location of the separation points [31]. Within the scatter of the experimental data for the ratio of the wall pressure at the separation point to the ambient pressure, there seems to be no consistent significant difference between two-dimensional and axisymmetric nozzles, nor can any trend be detected as a function of nozzle half angle, for a range of half angles between $7°$ and $30°$. Fraser et al.; McKenney, and Foster and Cowles conclude that flow separation occurs at the point where the nozzle wall pressure reaches a particular fraction of the ambient pressure [31]. The "Summerfield criterion" predicts separation for $P_s/P_a < 0.4$. An alternate attempt to predict the separation point assumes that the oblique shock causing separation is such as to turn the flow at the wall to the axial direction [31].

CHAPTER 3. GOVERNING FLOW EQUATIONS AND TURBULENCE MODELING

In this chapter, we present the set of equations that describes the compressible turbulent flows, which will be used to resolve the flow phenomena in our problem. In the first hand, we start by presenting the physical and mathematical model of fluid dynamics which are the compressible Navier-Stokes equations. Then, making the appropriate averaging techniques for the flow variables, and based on some assumptions, we form the FANS (Favre-Averaged Navier Stokes) equations. Lastly, we will speak about the closure problem and modeling of the correlation's terms, especially, for the Reynolds stresses which will form the basis for turbulence modeling (effects). Finally, we will present three different turbulence models based on the Boussinesq hypothesis, or eddy-viscosity models, that will be adopted in this study.

3.1 The Fundamental Equations for Compressible Flows:

The flow phenomena are fully described by three sets of conservation principles namely,

- The conservation of mass (continuity) equation,

$$\frac{\partial \rho}{\partial t} + \frac{\partial (\rho u_j)}{\partial x_j} = 0 \tag{3-1}$$

- The conservation of momentum equation,

$$\frac{\partial (\rho u_i)}{\partial t} + \frac{\partial (\rho u_i u_j)}{\partial x_j} = \frac{\partial T_{ij}}{\partial x_j} = \frac{\partial \left(-P\delta_{ij} + \tau_{ij}\right)}{\partial x_j} \tag{3-2}$$

Where,

T_{ij}, is the complete stress tensor applied to a fluid element or fluid parcel.

P_{ij}, is the hydrostatic or more properly the thermodynamic pressure.

τ_{ij}, is the stress tensor due to viscosity.

δ_{ij}, is the Kronecker tensor (1 if $i = j$, 0 if $i \neq j$).

For Newtonian fluids the stress tensor, τ_{ij}, is proportional to the rate of strain tensor S_{ij} [32] [33]:

$$\tau_{ij} = 2\mu\, S_{ij} + \lambda S_{kk}\delta_{ij} \tag{3-3}$$

Where μ is the dynamic viscosity coefficient, λ is usually called the second viscosity coefficient, and,

$$S_{ij} = \frac{1}{2}\left(\frac{\partial u_i}{\partial x_j} + \frac{\partial u_j}{\partial x_i}\right) \tag{3-4}$$

It may now be useful to express the tensor S_{ij} as the sum of its isotropic and deviatoric parts, says S_{ij}^A and S_{ij}^D respectively:

$$S_{ij}^A = \frac{1}{3} S_{kk}\delta_{ij} = \frac{1}{3}\frac{\partial u_k}{\partial x_k}\delta_{ij} \tag{3-5}$$

$$S_{ij}^D = S_{ij} - S_{ij}^A = \frac{1}{2}\left(\frac{\partial u_i}{\partial x_j} + \frac{\partial u_j}{\partial x_i}\right) - \frac{1}{3}\frac{\partial u_k}{\partial x_k}\delta_{ij} \tag{3-6}$$

Thus, we get,

$$\tau_{ij} = \left(\lambda + \frac{2}{3}\mu\right)\frac{\partial u_k}{\partial x_k}\delta_{ij} + 2\mu\, S_{ij}^D = \mu_v \frac{\partial u_k}{\partial x_k}\delta_{ij} + 2\mu\, S_{ij}^D \tag{3-7}$$

Where we introduce the bulk viscosity coefficient μ_v, defined as $\mu_v = (\lambda + 2\mu/3)$.

As can be seen, the viscous stress tensor has, in general, both an isentropic part and a deviatoric part. By recalling form Eq. (3-2) that the complete stress tensor as applied to a fluid element is both composed of pressure action as well as a viscous contribution thus it follows that the complete stress tensor is given by,

$$T_{ij} = \left(-P + \mu_v \frac{\partial u_k}{\partial x_k}\right)\delta_{ij} + \mu\left(\frac{\partial u_i}{\partial x_j} + \frac{\partial u_j}{\partial x_i} - \frac{2}{3}\frac{\partial u_k}{\partial x_k}\delta_{ij}\right) \tag{3-8}$$

Eq. (3-8) shows that, in general, the isentropic part of the complete stress tensor contains a viscous term that is additive to the pressure term. We may then interpret $\mu_v\, div\boldsymbol{V}$ as the difference between the thermodynamic pressure and the opposite of the average of the normal stresses acting on any three orthogonal planes passing through a point in the fluid, which is usually referred to as *the mechanical pressure.* This difference is generally considered to be due to the time lag with which the thermodynamic equilibrium condition is reached in a motion that implies an isotropic dilatation of a fluid element [33].

Following a suggestion by stocks [33] [34], it is customary to assume that μ_v is negligible or, in other words, that the two coefficients of viscosity appearing in Eq. (3-3) are linked by the relation

$$\lambda + \frac{2}{3}\mu = 0 \tag{3-9}$$

This is known as *Stokes' hypothesis*, and its use has become common practice in the analysis of the motion of compressible fluids. As may be seen from Eq. (3-8), it implies that the thermodynamic pressure coincides with the mechanical pressure and characterizes the isotropic part of the complete stress tensor; furthermore, the viscous stress tensor becomes a purely deviatoric tensor and corresponds to the deviatoric part of T_{ij}. In other words, assuming the validity of Eq. (3-9) is equivalent to stating that isotropic dilatations of an elementary volume of fluid do not produce viscous stresses.

The use of Stokes' hypothesis renders the mathematical treatment of compressible flows considerably easier, but it has been the object of long-lasting discussions (see, e.g., the papers presented at the workshop chaired by Rosenhead [35], or the considerations in [36]). Indeed, for polyatomic gases, the available data for μ_v (though not numerous due to the complexity of its experimental evaluation) show that it is certainly not zero and often far from being negligible. For instance, μ_v is of the same order as μ for nitrogen and oxygen, but other gases, such as carbon dioxide, are characterized by much larger values of μ_v, of the order of $10^3\mu$. On the other hand, it is usually claimed that a fundamental result of the kinetic theory of gases is that $\mu_v = 0$ for monatomic gases. This would agree with the physical interpretation that the bulk viscosity is connected with the time lag for reaching local equilibrium conditions. This time would be much shorter for monatomic gases, due to the absence of the rotational and vibrational modes characterizing polyatomic gases. Furthermore, the rather scarce available experimental evidence (see, e.g., [37]) seems to suggest that the bulk viscosity of monatomic gases is indeed practically negligible. However, already more than sixty years ago, Truesdell [38] observed that a zero value of the bulk viscosity is not derived from but implicitly assumed in Maxwell's kinetic theory of gases. More recently, Rajagopal [39], starting from a different approach to the constitutive equations of a viscous fluid—in which the rate of strain is expressed as a linear function of the stress tensor rather than the opposite—concluded that the bulk viscosity can never be zero for physically realistic fluids, including monatomic gases. Finally, the bulk viscosity is significantly higher than the dynamic viscosity also for many liquids (see, e.g., [35], [40]).

In summary, one may consider as amply demonstrated that for most fluids of practical interest, the bulk viscosity is not zero and that the ratio μ_v/μ may vary from almost negligible to very large values. Therefore, such evaluations of the order of magnitude of the bulk viscosity seem to be in contradiction with the fact that, excluding very particular conditions, in most applications

concerning compressible flows good results may indeed be obtained by using the usual formulation of Stokes' hypothesis, namely that $\mu_v = 0$. Thus, we are seemingly left with the paradox that, to get adequate descriptions of most flow fields, we must retain the viscosity coefficient μ in Eq. (3-10), which defines the viscous stress tensor, but we are allowed to neglect the other one, μ_v, which may be of the same order of magnitude or even much larger.

A reasonable explanation of this circumstance may be obtained from a deeper analysis of the contribution of the stress tensor term in which the bulk viscosity appears—namely $\mu_v \, div\boldsymbol{V}$—and from a reflection on the admissibility of the operation that is done when a term is neglected in a relation or an equation (see also [41]). To this end, it is useful to rewrite the expressions of the tangential and normal components of the complete stress tensor separately. For a generic tangential stress ($i \neq j$), we have

$$T_{ij} = \mu \left(\frac{\partial u_i}{\partial x_j} + \frac{\partial u_j}{\partial x_i} \right) = 2\mu \, S_{ij}^D \tag{3-10}$$

Whereas the expression for a generic normal stress ($i = j$) is:

$$T_{ii} = \left(-P + \mu_v \frac{\partial u_k}{\partial x_k} \right) + 2\mu \left(\frac{\partial u_i}{\partial x_i} - \frac{1}{3} \frac{\partial u_k}{\partial x_k} \right) = \left(-P + 3\kappa \, S_{ii}^A \right) + 2\mu \, S_{ii}^D \tag{3-11}$$

The essential point to be observed now is that the terms S_{ii}^A are all equal, whereas this cannot happen for the terms S_{ii}^D because the trace of the deviatoric tensor D is zero. The effect of $\mu_v \, div\boldsymbol{V}$ is thus perfectly additive to that of the thermodynamic pressure; in other words, this term is associated with the same deformation—isotropic dilatation of a fluid element—that is connected with the thermodynamic pressure, which, however, is generally larger than $\mu_v \, div\boldsymbol{V}$ (in absolute value) by several orders of magnitude. Conversely, the coefficient μ, however small it may be, is associated with normal and tangential stresses causing deformations that cannot be justified without taking viscosity into account, namely pure strain (i.e., non-isotropic normal deformation) and pure distortion.

The above analysis suggests that we might formulate a different condition, which in practical applications is equivalent to the original Stokes' hypothesis but is much more satisfactory from the physical point of view and does not require disregarding the available experimental evidence. Indeed, rather than putting $\mu_v = 0$, we may simply assume that the absolute value of $\mu_v \, div\boldsymbol{V}$ is negligible compared to the thermodynamic pressure, i.e., that the following relation holds:

$$|\mu_v \, div\boldsymbol{V}| \ll P \tag{3-12}$$

In other words, with this assumption, we are neglecting any difference between the mechanical and the thermodynamic pressures. The rationale for this different approach and its applicability stands upon the obvious fact that a term appearing in a relation or equation cannot be neglected just because it is small, but only if it is small compared to a qualitatively similar one, i.e., to one that has the same effect. If this different point of view is adopted, there are indeed good reasons for the modified formulation Eq. (3-12) of Stokes' hypothesis to be a largely acceptable approximation. Only in very particular conditions will the term $\mu_v \, div\boldsymbol{V}$ be comparable to the thermodynamic pressure. This may happen, for instance, when the fluid is characterized by large values of μ_v (e.g., CO2), and the motion is such that extremely large values of $div\boldsymbol{V}$ occur, as happens in hypersonic flows or flows through shock waves (see [42] [43]).

Thus, for our analysis we follow the Stokes hypothesis in the above philosophy, so, the viscous stress tensor is linearly dependent only on the deviatoric part of the strain tensor namely,

$$\tau_{ij} = 2\mu \, S_{ij}^{D} = \mu\left(\frac{\partial u_i}{\partial x_j} + \frac{\partial u_j}{\partial x_i} - \frac{2}{3}\frac{\partial u_k}{\partial x_k}\,\delta_{ij}\right) \tag{3-13}$$

- The conservation of energy equation,

$$\frac{\partial(\rho E)}{\partial t} + \frac{\partial(\rho E u_j)}{\partial x_j} = -\frac{\partial q_j}{\partial x_j} + \frac{\partial\left(u_i\left(\tau_{ij} - P\delta_{ij}\right)\right)}{\partial x_j} \tag{3-14}$$

In equations (3-2) and (3-14) body forces due to gravity are assumed small (negligible) and no heat sources are present. ρ, u_i, P denotes the density, velocity, and pressure. E is the total energy which comprises the internal energy e and the kinetic energy per unit mass:

$$E = e + \frac{1}{2}u_i u_i \tag{3-15}$$

According to Fourier's law, the heat flux by conduction, q_j is related to the temperature gradient:

$$q_j = -\lambda\frac{\partial T}{\partial x_j} = -c_p\frac{\mu}{P_r}\frac{\partial T}{\partial x_j} \tag{3-16}$$

Where λ is the heat conductivity coefficient and the laminar Prandtl number Pr is defined by

$$P_r = \frac{c_p\mu}{\lambda} \tag{3-17}$$

To close these equations, it's also necessary to specify an equation of state, this part has been widely discussed in Chapter 1, refer to it for more information. Assuming a calorically perfect gas, the following relations are valid:

$$
\begin{aligned}
P &= \rho R T \\
e &= c_v T \\
c_p - c_v &= R \\
\gamma &= c_p / c_v
\end{aligned}
\tag{3-18}
$$

The above corresponding governing equations, supplemented with gas data for C_p, μ, λ and R, form a closed set of partial differential equations, and need only to be complemented with boundary and initial conditions [48]. It's worth well to emphasis that these equations are applicable for laminar as well as turbulent compressible flow without the need for any additional modeling, but the computational power required for such application is practically unavailable today at least not to the industrial or academic level except for some specialized organization.

For air the corresponding data are [44]:

$$
\begin{aligned}
R &= 287.035 \frac{J}{Kg \cdot K} \\
c_p &= 1004.7257 \frac{J}{Kg \cdot K}
\end{aligned}
\tag{3-19}
$$

Sutherland's formula for the shear viscosity is valid in a range of temperatures, between 200K and 1200K [45]:

$$
\frac{\mu}{1.716 \cdot 10^{-5}} = \left(\frac{T}{273}\right)^{\frac{3}{2}} \cdot \frac{384}{T + 111} \tag{3-20}
$$

The heat conductivity is likewise affected by the state of the internal energy of the molecules and follows a similar Sutherland law (Bertolotti(1997)) obtained from the best fit to experimental data [45]:

$$
\frac{\lambda}{0.0241} = \left(\frac{T}{273}\right)^{3/2} \cdot \frac{467}{T + 194} \tag{3-21}
$$

3.2 The Statistical Equations for Compressible Turbulent Flows (FANS)

We begin the discussion with a rough classification of compressible turbulent flows into [46]:

I) Flows with unimportant compressibility effects due to turbulent fluctuations and;
II) Flows in which such effects play a role.

Type I flows are assumed to follow Morkovin's hypothesis in its weak form (Morkovin (1962)) which states that thermodynamic pressure and total temperature fluctuations are negligible for small turbulent Mach numbers implying negative density-temperature correlations. The hypothesis

has led to the so-called strong Reynolds analogy (SRA) and is in line with the Van Driest transformation (Van Driest (1951)) which collapses velocity profiles of compressible turbulent boundary layers onto the incompressible law of the wall (Fernholz & Finley (1980), Huang & Coleman (1994)). Compressibility effects therefore manifest themselves in terms of mean density variations and can be modeled by straightforward adaptations of classical incompressible models. Besides boundary layers with zero or weak pressure gradient and freestream Mach numbers less than 5, mixing layers with convective Mach numbers less than 1 are commonly considered examples of type I flows (Bradshaw (1977)). It is also expected (although not confirmed at present) that type II flows in which fluctuations of the thermodynamic pressure become important, are encountered at hypersonic speeds. Unfortunately, direct numerical simulation data are not yet available to clarify this issue. A closer look at DNS results for different classes of flows, however, unveils the lack of subtlety of such a classification. Coleman et al.'s (1995) DNS of supersonic fully developed flow in a channel with cooled walls e.g. shows that, although compressibility effects due to turbulent fluctuations are unimportant, the strong Reynolds analogy in its form for nonadiabatic flows (Gaviglio (1987), Rubesin (1990)) does not apply. A more general representation of the analogy was therefore derived by Huang et al. (1995) and shown to match the DNS data. Recent direct simulations of annular mixing layers with convective Mach numbers ranging from $M_c = 0.1$ to 1.8 by Freund et al. (1997) indicate that pressure fluctuations are subordinate to temperature and density fluctuations (related to their mean values, respectively) only for $Mc < 0.2$. For higher values of Mc, Morkovin's hypothesis for adiabatic flows does not apply. A third example where pressure fluctuations are non-negligible is shock isotropic turbulence interaction. Based on DNS and linear theory Mahesh et. al. (1995) found a considerable deviation from Morkovin's hypothesis (in its weak form) behind shocks, although the deviations were seen to decrease with the downstream distance. To be more specific, total temperature fluctuations are generated immediately behind the shock as a result of shock oscillation and are convected into the far field. A second important finding of their work is that upstream entropy fluctuations lead to higher amplification rates of turbulent kinetic energy and vorticity across the shock than pure vortical fluctuations. This result should be of great value in explaining the interaction between shocks and strongly cooled boundary layers [46].

These examples show that a conclusive classification scheme for compressible turbulent flows is difficult to find at present, especially as long as our knowledge of compressibility effects is not complete [46].

In summary, adopting the weak form of Morkovin's hypothesis suggests that these density fluctuations in compressible turbulent flows have a negligible impact on the dynamics of turbulence, allowing the flow to be modeled similarly to incompressible turbulence.

3.2.1 Definition of averages

Engineering applications often face challenges when dealing with turbulent flow. The governing equations, under high Reynolds numbers typical of real-world situations, exhibit unpredictable and chaotic behavior. Directly solving these equations is not feasible due to the complexity introduced by turbulence. To simplify this problem, turbulence modeling focuses on capturing the overall effects rather than resolving all minute details. One-point averaging techniques are commonly used, these techniques focus on calculating averaged quantities, such as velocity, pressure, and temperature, at a single spatial location over time or across an ensemble of realizations. This removes the chaotic fluctuations caused by turbulence, allowing us to focus on the general behavior of the flow.

For compressible flows, it is common practice to work with two different averages simultaneously, the Reynolds average, denoted by a bar, and the Favre- or mass-weighted average, characterized by a tilde [46].

Let ϕ be any dependent variable.

- Classical time averaging (Reynolds averaging):

$$\phi = \bar{\phi} + \phi'$$
$$\bar{\phi} = \frac{1}{T}\int_{T} \phi(t)\, dt \tag{3-22}$$

This definition implies that,

$$\bar{\phi}' = 0 \tag{3-23}$$

- Density-weighted time averaging (Favre averaging):

$$\phi = \tilde{\phi} + \phi''$$
$$\tilde{\phi} = \frac{\overline{\rho\phi}}{\bar{\rho}} \tag{3-24}$$

This definition implies that,

$$\begin{aligned} \bar{\rho}\tilde{\phi} &= \overline{\rho\phi} \\ \overline{\rho\phi''} &= 0 \\ \overline{\phi''} &\neq 0 \end{aligned} \tag{3-25}$$

3.2.2 Favre Averaged Navier Stocks Equation (FANS)

When dealing with compressible flows (or variable density flows), besides the velocity and pressure fluctuation, we must account for density and temperature fluctuations. If we introduce the Reynolds decomposition and time-averaging the equations, additional fluctuating correlation arises. To achieve closure, we need to somehow approximate the correlation between the fluctuating quantities. Besides the complexity of the problem, it's yet practically impossible. One way to reduce these correlations and simplify the problem is to introduce a density-weighted averaging procedure suggested by Favre [47]. Following Favre, introducing a density-weighted time average decomposition (3-22) of u_i and E, and a standard time average decomposition (3-24) of ρ and P to the instantaneous continuity equation (3-1), momentum equation (3-2), and energy equation (3-14), then, time-averaging gives the following exact open equations [48]:

$$\frac{\partial \bar{\rho}}{\partial t} + \frac{\partial}{\partial x_i}[\bar{\rho}\tilde{u}_i] = 0 \tag{3-26}$$

$$\frac{\partial}{\partial t}(\bar{\rho}\tilde{u}_i) + \frac{\partial}{\partial x_j}\left[\bar{\rho}\tilde{u}_i\tilde{u}_j + \bar{P}\delta_{ij} + \overline{\rho u_i'' u_j''} - \overline{\tau_{ij}}\right] = 0 \tag{3-27}$$

$$\frac{\partial}{\partial t}\left(\bar{\rho}\tilde{E}\right) + \frac{\partial}{\partial x_j}\left[\bar{\rho}\tilde{E}\tilde{u}_j + \tilde{u}_j\bar{P} + \overline{u_j''P} + \overline{\rho u_j'' E''} + \overline{q_j} - \overline{u_i\tau_{ij}}\right] = 0 \tag{3-28}$$

The density average total energy $\tilde{E}$ is given by,

$$\tilde{E} = \tilde{e} + \frac{\tilde{u}_k\tilde{u}_k}{2} + k \tag{3-29}$$

Where k is the turbulent kinetic energy k is defined as,

$$k = \frac{\overline{u_k'' u_k''}}{2} \tag{3-30}$$

Note that the corresponding expression (3-15) for Favre averaged turbulent flows contains an extra term related to the turbulent energy.

Equations (3-26) - (3-28) are referred to as the Favre averaged Navier-Stokes equations. $\bar{\rho}$, $\tilde{u}_i$ and $\tilde{E}$ are the primary solution variables. Note that this is an open set of partial differential equations that contains several unknown correlation terms. To obtain a closed form of equations that can be solved it is necessary to model these unknown correlation terms.

Approximation and modeling

It is convenient to rewrite the unknown terms in the following way:

$$\overline{\tau_{ij}} = \tilde{\tau}_{ij} + \overline{\tau''_{ij}} \tag{3-31}$$

$$\overline{u''_j P} + \overline{\rho u''_j E''} = c_p\, \overline{\rho u''_j T} + \tilde{u}_k \overline{\rho u''_k u''_j} + \frac{\overline{\rho u''_j u''_k u''_k}}{2} \tag{3-32}$$

$$\bar{q}_j = -\overline{c_p \frac{\mu}{Pr}\frac{\partial T}{\partial x_j}} = -c_p \frac{\mu}{Pr}\frac{\partial \tilde{T}}{\partial x_j} - c_p \frac{\mu}{Pr}\frac{\partial \overline{T''}}{\partial x_j} \tag{3-33}$$

$$\overline{u_i \tau_{ij}} = \tilde{u}_i \tilde{\tau}_{ij} + \overline{u''_i \tau_{ij}} + \tilde{u}_i \overline{\tau''_{ij}} \tag{3-34}$$

Where the perfect gas relations (3-18) and Fourier's law (3-16) have been used. Note also that fluctuations in the molecular viscosity, μ, have been neglected [48].

inserting (3-31) - (3-34) into (3-26), (3-27) and (3-28) gives:

$$\frac{\partial \bar{\rho}}{\partial t} + \frac{\partial}{\partial x_i}[\bar{\rho}\tilde{u}_i] = 0 \tag{3-35}$$

$$\frac{\partial}{\partial t}(\bar{\rho}\tilde{u}_i) + \frac{\partial}{\partial x_j}\left[\bar{\rho}\tilde{u}_i\tilde{u}_j + \bar{P}\delta_{ij} + \overline{\rho u''_i u''_j}\ (1) - \tilde{\tau}_{ij} - \overline{\tau''_{ij}}\ (2)\right] = 0 \tag{3-36}$$

$$\begin{aligned}\frac{\partial}{\partial t}(\bar{\rho}\tilde{E}) + \frac{\partial}{\partial x_j}\Bigg[&\bar{\rho}\tilde{E}\tilde{u}_j + \tilde{u}_j\bar{P} + c_p\,\overline{\rho u''_j T}\ (3) + \tilde{u}_k\overline{\rho u''_k u''_j}(4) + \frac{\overline{\rho u''_j u''_k u''_k}}{2}\ (5)\\ &- c_p\frac{\mu}{Pr}\frac{\partial \tilde{T}}{\partial x_j} - c_p\frac{\mu}{Pr}\frac{\partial \overline{T''}}{\partial x_j}(6) - \tilde{u}_i\tilde{\tau}_{ij} - \overline{u''_i\tau_{ij}}(7) - \tilde{u}_i\overline{\tau''_{ij}}\ (8)\Bigg] = 0\end{aligned} \tag{3-37}$$

The terms marked in red from (1) to (8) are unknown, and have to be modeled in some way.

Terms (1) and (4) can be modeled using an eddy-viscosity assumption for the Reynolds stresses,τ_{ij}^{turb}, based on the Boussinesq hypothesis [48],

$$\tau_{ij}^{turb} \equiv -\overline{\rho u''_i u''_j} \approx 2\mu_t \widetilde{S_{ij}^D} - \frac{2}{3}\bar{\rho}k\delta_{ij} \tag{3-38}$$

Where μ_t is a turbulent viscosity, which is estimated with a turbulence model. The last term is included to ensure that the trace of the Reynolds stress tensor is equal to $-2\rho k$, as it should be [48].

Terms (2) and (8) can be neglected if;

$$\left|\tilde{\tau}_{ij}\right| \gg \left|\overline{\tau_{ij}''}\right| \tag{3-39}$$

This is true for virtually all flows [17].

Term (3) corresponding to the turbulent transport of heat, can be modeled using a gradient approximation for the turbulent heat flux:

$$q_j^{turb} \equiv c_p \, \overline{\rho u_j'' T} \approx - c_p \frac{\mu_t}{Pr_t} \frac{\partial \tilde{T}}{\partial x_j} \tag{3-40}$$

Where Pr_t is the turbulent Prandtl number, often a constant $Pr_t \approx 0.9$ is used [48].

Terms (5) and (7), corresponding to turbulent transport and molecular diffusion of turbulent energy, can be neglected if the turbulent energy is small compared to the enthalpy:

$$k \ll \tilde{h} = c_p \tilde{T} \tag{3-41}$$

This is a reasonable approximation for most flows below the hypersonic regime [48]. A better approximation might be a gradient expression of the form:

$$\frac{\overline{\rho u_j'' u_k'' u_k''}}{2} - \overline{u_i'' \tau_{ij}} \approx - \left(\mu + \frac{\mu_t}{\sigma_k}\right) \frac{\partial k}{\partial x_j} \tag{3-42}$$

Where $\sigma_k$is a model constant [48]. This approximation will not be included in the derived formulas below. Instead, term (5) and (7) will be set to zero in the energy equation.

Term (6) is an artifact from the Favre averaging. It is related to heat conduction effects associated with temperature fluctuations. It can be neglected if:

$$\left|\frac{\partial^2 \tilde{T}}{\partial x_j^2}\right| \gg \left|\frac{\partial^2 \overline{T''}}{\partial x_j^2}\right| \tag{3-43}$$

This is true for virtually all flows, and has been assumed in all following equations [48].

Closed approximated equations

To summarize, the governing equations (3-35) - (3-37), with assumptions (3-38), (3-39), (3-40), (3-41), and (3-43) can be written as in (3-44) - (3-54). These equations are valid for a perfect gas. Note also that all fluctuations in the molecular viscosity have been neglected.

$$\frac{\partial \bar{\rho}}{\partial t} + \frac{\partial}{\partial x_i}[\bar{\rho}\tilde{u}_i] = 0 \tag{3-44}$$

$$\frac{\partial}{\partial t}(\bar{\rho}\tilde{u}_i) + \frac{\partial}{\partial x_j}\left[\bar{\rho}\tilde{u}_i\tilde{u}_j + \bar{P}\delta_{ij} + \tilde{\tau}_{ij}^{tot}\right] = 0 \tag{3-45}$$

$$\frac{\partial}{\partial t}\left(\bar{\rho}\tilde{E}\right) + \frac{\partial}{\partial x_j}\left[\bar{\rho}\tilde{E}\tilde{u}_j + \tilde{u}_j\bar{P} + \tilde{q_j} - \tilde{u}_i\tilde{\tau}_{ij}^{tot}\right] = 0 \tag{3-46}$$

Where,

$$\tilde{\tau}_{ij}^{tot} = \tilde{\tau}_{ij}^{lam} + \tilde{\tau}_{ij}^{turb} \tag{3-47}$$

$$\tilde{\tau}_{ij}^{lam} \equiv \tilde{\tau}_{ij} = \mu\left(\frac{\partial \tilde{u}_i}{\partial x_j} + \frac{\partial \tilde{u}_j}{\partial x_i} - \frac{2}{3}\frac{\partial \tilde{u}_k}{\partial x_k}\,\delta_{ij}\right) \tag{3-48}$$

$$\tilde{\tau}_{ij}^{turb} \equiv -\overline{\rho u_i'' u_j''} \approx \mu_t\left(\frac{\partial \tilde{u}_i}{\partial x_j} + \frac{\partial \tilde{u}_j}{\partial x_i} - \frac{2}{3}\frac{\partial \tilde{u}_k}{\partial x_k}\,\delta_{ij}\right) - \frac{2}{3}\bar{\rho}k\delta_{ij} \tag{3-49}$$

$$\tilde{q}_j^{tot} \equiv \tilde{q}_j^{lam} + \tilde{q}_j^{turb} \tag{3-50}$$

$$\tilde{q}_j^{lam} \equiv \tilde{q}_j \approx -c_p\frac{\mu}{Pr}\frac{\partial \tilde{T}}{\partial x_j} = -\frac{\gamma}{\gamma-1}\frac{\mu}{Pr}\frac{\partial}{\partial x_j}\left[\frac{\bar{P}}{\bar{\rho}}\right] \tag{3-51}$$

$$\tilde{q}_j^{turb} \equiv c_p\,\overline{\rho u_j'' T} \approx -\,c_p\frac{\mu_t}{Pr_t}\frac{\partial \tilde{T}}{\partial x_j} = -\frac{\gamma}{\gamma-1}\frac{\mu_t}{Pr_t}\frac{\partial}{\partial x_j}\left[\frac{\bar{P}}{\bar{\rho}}\right] \tag{3-52}$$

And the perfect gas law transforms into,

$$\bar{P} = \bar{\rho}R\tilde{T} = \bar{\rho}R\frac{\tilde{e}}{c_v} = (\gamma-1)\bar{\rho}\left(\tilde{E} - \frac{\tilde{u}_k\tilde{u}_k}{2} - k\right) \tag{3-53}$$

If a separate turbulence model is used to calculate μ_t, k and Pr_t, and gas data is given for μ ,γ and Pr these equations form a closed set of partial differential equations, which can be solved numerically [48].

3.3 Eddy Viscosity Turbulence Models

At the first stage, when Reynolds introduced his decomposition to the primitive variables of the flow, he formed the well-known RANS equation. Turbulence manifested its effects by three terms in the three momentum equations, for a total of nine terms. These terms were grouped and called the Reynolds stress tensor R_{ij}. R_{ij} has the property to be symmetric, meaning that only six of the nine terms are independent, that $R_{ij} = R_{ji}$. Thus, six additional independent quantities are still needed! This is the famous "closure problem" that has plagued turbulence modeling since 1895 to the present and is not going away any time soon. The Reynolds stresses are therefore approximated

(modeled) experimentally, empirically, or numerically (e.g., DNS). Bold engineers, in a desire to reach closure, began attempting ways to relate the fluctuating properties to the averaged quantities, based on dimensional arguments and a gradient transport analogy. So, for better or for worse, these arguments are employed fairly commonly in turbulence research [49]. In this case and based on the discussion made at the start of this part,

$$-\overline{\rho u_i'' \phi''} \approx -\bar{\rho}\,\overline{u_i'' \phi''} \tag{3-54}$$

$$-\overline{u_i'' \phi''} \sim \frac{\partial \tilde{\phi}}{\partial x_i} \tag{3-55}$$

Where ϕ is any primitive variable, e.g., u_i, T, P, ρ, etc. An inspection of Eq. (3-55) shows that it can be made fully dimensionless by including a quantity that has units of m^2/s. Out of incredible inspiration (or desperation!), a new quantity was coined, "turbulent kinematic viscosity," ν_t, which is analogous to the kinematic viscosity [49]. Hence,

$$-\overline{u_i'' \phi''} = \nu_t \frac{\partial \tilde{\phi}}{\partial x_i} \tag{3-56}$$

The turbulent kinematic viscosity is typically, orders of magnitude, higher than the fluid viscosity, thus providing a reasonable way to gauge the degree of turbulence in a flow:

$$\frac{\nu_t}{\nu} \gg 1 \tag{3-57}$$

That $\nu_t \gg \nu$ is consistent with the expectation that the more turbulent the flow is, the larger ν_t will be. At this point, it is noteworthy to point out that both the kinematic viscosity and the turbulence viscosity have the same units and similar names. But, that is where the similarities end. The kinematic viscosity is based on the fluid type, pressure, and temperature, and is a measure of damping, with higher kinematic viscosity resulting in higher damping. On the other hand, the turbulent kinematic viscosity is based on Re, where the higher Re is, the higher the turbulent kinematic viscosity. Thus, the turbulent viscosity is a measure of the degree of turbulence being experienced by the fluid, with higher turbulent viscosities implying a higher degree of turbulence in the local region. In fact, if $\nu_t \rightarrow \nu$, then it is a safe bet that the flow is laminar [49].

Note that whereas the dynamic and kinematic viscosities are always positive, the turbulent dynamic and turbulent kinematic viscosities can become negative if the eddies are violent enough to impart energy onto the mean flow. Though not common, it is an issue associated with large-scale flows with high anisotropy, such as violent weather patterns (Sivashinsky and Yakhot 1985;

Dubrulle and Frisch 1991; Sivashinsky and Frenkel 1992) and ferrofluids under alternating magnetic fields at high frequencies (Shliomis and Morozov 1994) [49].

Continuing on, each of the nine Reynolds stresses can finally be approximated using Eq. (3-54),

$$\boldsymbol{R} \equiv \begin{vmatrix} \overline{\rho u'' u''} & \overline{\rho u'' v''} & \overline{\rho u'' w''} \\ \overline{\rho v'' u''} & \overline{\rho v'' v''} & \overline{\rho v'' w''} \\ \overline{\rho w'' u''} & \overline{\rho w'' v''} & \overline{\rho w'' w''} \end{vmatrix} \cong -\bar{\rho} \begin{vmatrix} \overline{u'' u''} & \overline{u'' v''} & \overline{u'' w''} \\ \overline{v'' u''} & \overline{v'' v''} & \overline{v'' w''} \\ \overline{w'' u''} & \overline{w'' v''} & \overline{w'' w''} \end{vmatrix} \approx \mu_t \begin{vmatrix} \frac{\partial \tilde{u}}{\partial x} & \frac{\partial \tilde{u}}{\partial y} & \frac{\partial \tilde{u}}{\partial z} \\ \frac{\partial \tilde{v}}{\partial x} & \frac{\partial \tilde{v}}{\partial y} & \frac{\partial \tilde{v}}{\partial z} \\ \frac{\partial \tilde{w}}{\partial x} & \frac{\partial \tilde{w}}{\partial y} & \frac{\partial \tilde{w}}{\partial z} \end{vmatrix} \quad (3\text{-}58)$$

Where,

$$\nu_t = \frac{\mu_t}{\bar{\rho}} \quad (3\text{-}59)$$

However, a new unknown was introduced, μ_t, which now requires an additional equation to solve. The approximation from Eq. (3-58) takes inspiration from the Newtonian stress tensor Eq. (3-7). The Boussinesq turbulence approximation assumes an analogous expression to the laminar Newtonian stress tensor, thereby asserting Eq. (3-49). The approximation asserts that the Reynolds stress tensor R_{ij} is proportional to the mean strain rate tensor $\tilde{S}_{ij}$, with the proportionality being twice the turbulent dynamic viscosity. Thus, R_{ij} is "aligned" with $\tilde{S}_{ij}$ along the principal axes (Hinze 1987; Peng and Davidson 1999; Wilcox 2006). The vast majority of the RANS-based turbulence models use this linear constitutive relationship for closure to estimate the Reynolds stresses; this is at the core of many modern one- and two-equation RANS models. The approximation is sometimes referred to as the Boussinesq hypothesis, but because it is more akin to an "assumption," Wilcox referred to it as the Boussinesq assumption (Wilcox 2006). The "assumption," of course, lies in the belief that the Reynolds stresses behave similarly as the Newtonian stress tensor. Though greatly successful, the Boussinesq approximation has some shortcomings, including the following situations:

- Secondary motion in ducts (rectangular pipe flow in the corner region, semi-truck vortex),
- Rapid changes in the mean strain rate tensor (rapid dilatation resulting in large volume change, high Mach),
- Curved surfaces (concave, convex, large swirl angle, airfoils),
- Rotating fluids (turbomachinery, wind turbines),
- Nonhomogeneous turbulent flows.

Under such situations, it is advisable to consider some corrections to the models that take the form of:

- Additional source terms,
- Extra terms in the transport equations,
- Corrective factors (damping, blending, limiting) in some of the terms of the transport equations.

Or extended, nonlinear versions of the Boussinesq approximation. There are many nonlinear constitutive equations in the literature, some of which include the curl operator to evaluate the mean vorticity. Such models are suitable for modeling curved surfaces, high swirls, secondary flows, flow separation, recirculation, highly anisotropic flows, and so forth (Lumley 1970; Bakker 2005; Alfonsi 2009; Wilcox 2006). Recent DNS and experimental data investigations continue to show issues with the Boussinesq approximation; some of these can be resolved using nonlocal, nonequilibrium approaches (Speziale and Eringen 1981; Hamba 2005; Schmitt 2007; Hamlington and Dahm 2009; Wilcox 2006; Spalart 2015) [49].

3.3.1 Specifying the Eddy Viscosity

The kinematic eddy viscosity has dimensions of $[velocity] \times [length]$, which suggests that it be modeled as

$$\nu_t = u_0 l_0 \tag{3-60}$$

Physically, u_0 should reflect the magnitude of velocity fluctuations and l_0 the size of turbulent eddies [50]. For wall-bounded flows a candidate for u_0 is the friction velocity, $u_\tau = \sqrt{\frac{\tau_w}{\rho}}$. However, this is not a local scale, since it depends on where the nearest wall is, and it is ambiguous near corners since it can be equidistant from two (or more) walls. A more appropriate velocity scale in general is $k^{1/2}$, where k is the turbulent kinetic energy [50].

For simple wall-bounded flows, l_0 is proportional to the distance from the boundary (e.g. $l_0 = \kappa y$). For simple free shear flows (e.g. jet, wake, mixing layer) l_0 is proportional to the width of the shear layer. However, these values are geometry-dependent and not conducive to complex geometries. For greater generality, we need to relate l_0 to local turbulence properties [50].

Common practice is to solve transport equations for one or more turbulent quantities (usually k + one other), from which μ_t can be derived on dimensional grounds. The following classification of eddy-viscosity models is based on the number of transport equations [50].

- ❖ Zero-equation models:
  - Constant-eddy-viscosity models;
  - Mixing-length models: l_0 specified geometrically; u_0 from mean flow gradients.
- ❖ One-equation models:
  - l_0 specified geometrically; transport equation to derive u_0;
- ❖ Two-equation models:
  - Transport equations for quantities from which u_0 and l_0 can be derived.
  - Of these, by far the most popular in general-purpose CFD are two-equation models: notably the $k-\varepsilon$ and $k-\omega$ models.

3.3.2 Low-Re Turbulence Models

Low Reynolds number (Low-Re) turbulence models are specifically designed to account for viscosity-dominated flows, particularly in regions near walls where turbulence is weak or transitioning from laminar flow. Unlike standard turbulence models, these models do not require special wall functions, as they can resolve flow quantities down to the viscous sublayer ($y^+ \leq 1$), making them ideal for applications with fine near-wall resolution [49] [50].

From this definition, we focus in this study on three major Low-Re turbulence models:

Wilcox $k-\omega$ Standard Model:

- Based on the transport of turbulent kinetic energy (k) and specific dissipation rate (ω).
- Effectively resolves near-wall turbulence without needing a wall function [49].
- More accurate for boundary layers, separation, and transition compared to its $k-\varepsilon$ counterpart [49].
- Better adaptability and performance for compressible flow extension, thus, applicable M ranging from incompressible to hypersonic flows [49] [51].
- Relevant for shock-separated flows, free shear flows, Backward-facing steps …ect.

Menter SST $k-\omega$ Model:

- An improvement over the standard $k-\omega$ model, combining features of both $k-\varepsilon$ and $k-\omega$ for better adaptability [49].
- Uses $k-\omega$ formulation near the wall for better Low-Re accuracy, while transitioning to $k-\varepsilon$ formulation in the free stream (high-Re) to improve stability [49].
- Highly effective for boundary layer flows, aerodynamic simulations, and curved surfaces [49].

- Ideal for adverse pressure gradients, separated flows, turbulent heat transfer, and aerospace applications [49].

Spalart-Allmaras Model:

- A single-equation turbulence model optimized for aerodynamic applications.
- Performs well in Low-Re flows, particularly in boundary layers with minimal separation.
- Frequently used in aerospace CFD simulations due to its robustness and computational efficiency.

In summary, Low-Re turbulence models provide a more precise representation of wall-bounded turbulence by capturing near-wall effects without relying on empirical wall functions. The Standard $k-\omega$, SST $k-\omega$, and Spalart-Allmaras models are three widely used approaches that ensure accuracy in simulations requiring fine near-wall resolution. Their effectiveness makes them the preferred choices for applications such as boundary layer modeling, aerodynamic optimization, and fluid-thermal interactions.

3.3.3 Spalart-Allmaras Model

The Spalart-Allmaras model [52] is a one-equation turbulence model designed for aerospace applications, particularly wall-bounded flows with adverse pressure gradients. Initially formulated as a low-Reynolds-number model, it requires near-wall resolution ($y^+ \sim 1$).

In Ansys Fluent, it has been extended with a y^+-insensitive wall treatment, allowing automatic blending from viscous sublayer to logarithmic formulations, ensuring consistent wall shear stress and heat transfer coefficients on intermediate grids ($1 < y^+ < 30$). However, a minimum resolution of $10-15$ cells is still recommended for accuracy [53].

While effective in aerodynamic and turbomachinery applications, the model is less reliable for free shear flows (e.g., plane and round jets) and does not accurately predict homogeneous isotropic turbulence decay [53].

Transport Equation for the Spalart-Allmaras Model

The transported variable in the Spalart-Allmaras model, $\tilde{\nu}$, is identical to the turbulent kinematic viscosity except in the near-wall (viscosity-affected) region. The transport equation for the modified turbulent viscosity $\tilde{\nu}$ is

$$\frac{\partial}{\partial t}(\bar{\rho}\tilde{\nu}) + \frac{\partial}{\partial x_i}(\bar{\rho}\tilde{\nu}\tilde{u}_i) = G_\nu + \frac{1}{\sigma_{\tilde{\nu}}}\left[\frac{\partial}{\partial x_j}\left\{\bar{\rho}(\nu + \tilde{\nu})\frac{\partial \tilde{\nu}}{\partial x_j}\right\} + C_{b2}\bar{\rho}\left(\frac{\partial \tilde{\nu}}{\partial x_j}\right)^2\right] - Y_\nu + S_{\tilde{\nu}} \qquad (3\text{-}61)$$

Where G_ν is the production of turbulent viscosity, and Y_ν is the destruction of turbulent viscosity that occurs in the near-wall region due to wall blocking and viscous damping. $\sigma_{\tilde{\nu}}$ and C_{b2} are the constants and ν is the molecular kinematic viscosity. $S_{\tilde{\nu}}$ is a user-defined source term. Note that since the turbulence kinetic energy, k, is not calculated in the Spalart-Allmaras model, thus, it is ignored when estimating the Reynolds stresses [53].

3.3.4 Standard $k - \omega$ Model

The standard $k - \omega$ model in Ansys Fluent is based on a $k - \omega$ model proposed by Wilcox in [54], which incorporates modifications for low-Reynolds number effects, compressibility, and shear flow spreading. One of the weak points of the 1998 Wilcox model is the sensitivity of the solutions to values for k and ω outside the shear layer (freestream sensitivity), which can have a significant effect on the solution, especially for free shear flows [55]. There is a newer version of the model (Wilcox 2006 k-ω model [56]), which also did not fully resolve the freestream sensitivity as shown in [55].

The standard $k - \omega$ model is an empirical model based on model transport equations for the turbulence kinetic energy (k) and the specific dissipation rate (ω), which can also be thought of as the ratio of ε to k [54]. As the $k - \omega$ model has been modified over the years, production terms have been added to both the k and ω equations, which have improved the accuracy of the model for predicting free shear flows.

Transport Equations for the Standard $k - \omega$ Model

The turbulence kinetic energy, k, and the specific dissipation rate, ω, are obtained from the following transport equations:

$$\frac{\partial}{\partial t}(\bar{\rho}k) + \frac{\partial}{\partial x_i}(\bar{\rho}k\tilde{u}_i) = \frac{\partial}{\partial x_j}\left(\Gamma_k \frac{\partial k}{\partial x_j}\right) + G_k - Y_k + S_k + G_b \qquad (3\text{-}62)$$

And

$$\frac{\partial}{\partial t}(\bar{\rho}\omega) + \frac{\partial}{\partial x_i}(\bar{\rho}\omega\tilde{u}_i) = \frac{\partial}{\partial x_j}\left(\Gamma_\omega \frac{\partial \omega}{\partial x_j}\right) + G_\omega - Y_\omega + S_\omega + G_{\omega b} \qquad (3\text{-}63)$$

In these equations, G_k represents the generation of turbulence kinetic energy due to mean velocity gradients. G_ω represents the generation of ω. Γ_k and Γ_ω represent the effective diffusivity of k and ω, respectively. Y_k and Y_ω represent the dissipation of k and ω due to turbulence. All of the above terms are calculated as described below. S_k and S_ω are user-defined source terms. G_b and $G_{\omega b}$ account for buoyancy terms as described in Effects of Buoyancy on Turbulence in the k-ω Models (p. 69 [53]).

3.3.5 Menter SST $k-\omega$ turbulence model

The main problem with the Wilcox model is its well-known strong sensitivity to freestream conditions. The baseline (BSL) $k-\omega$ model was developed by Menter [57] to effectively blend the robust and accurate formulation of the $k-\omega$ model in the near-wall region with the freestream independence of the $k-\varepsilon$ model in the far field. To achieve this, the $k-\varepsilon$ model is converted into a $k-\omega$ formulation. The BSL $k-\omega$ model is similar to the standard $k-\omega$ model, but includes the following refinements:

- The standard $k-\omega$ model and the transformed $k-\varepsilon$ model are both multiplied by a blending function and both models are added together. The blending function is designed to be one in the near-wall region, which activates the standard $k-\omega$ model, and zero away from the surface, which activates the transformed $k-\varepsilon$ model.
- The BSL model incorporates a damped cross-diffusion derivative term in the equation.
- The modeling constants are different.

The Shear Stress Transport (SST) $k-\omega$ model includes all the refinements of the BSL $k-\omega$ model, and in addition accounts for the transport of the turbulence shear stress in the definition of the turbulent viscosity [53].

These features make the SST $k-\omega$ model (Menter [57]) more accurate and reliable for a wider class of flows (for example, adverse pressure gradient flows, airfoils, transonic shock waves) than the standard and the BSL $k-\omega$ models.

Transport Equations for the SST $k-\omega$ Model

The SST $k-\omega$ model has a similar form to the standard $k-\omega$ model:

$$\frac{\partial}{\partial t}(\bar{\rho}k)+\frac{\partial}{\partial x_i}(\bar{\rho}k\tilde{u}_i)=\frac{\partial}{\partial x_j}\left(\Gamma_k\frac{\partial k}{\partial x_j}\right)+G_k-Y_k+S_k+G_b \tag{3-64}$$

And

$$\frac{\partial}{\partial t}(\bar{\rho}\omega) + \frac{\partial}{\partial x_i}(\bar{\rho}\omega\tilde{u}_i) = \frac{\partial}{\partial x_j}\left(\Gamma_\omega \frac{\partial \omega}{\partial x_j}\right) + G_\omega - Y_\omega + D_\omega + S_\omega + G_{\omega b} \quad (3\text{-}65)$$

In these equations, G_k represents the generation of turbulence kinetic energy, and is defined in the same manner as in the Standard $k-\omega$ model. G_ω represents the generation of ω, calculated as described in a section that follows. Γ_k and Γ_ω represent the effective diffusivity of k and ω, respectively, which are calculated as described in a section that follows. Y_k and Y_ω represent the dissipation of k and ω due to turbulence, calculated as described in the $k-\omega$ model. D_ω represents the cross-diffusion term, calculated as described in the section that follow. S_k and $S_\omega$are user-defined source terms. G_b and $G_{\omega b}$ account for buoyancy terms as described in Effects of Buoyancy on Turbulence in the k-ω Models (p. 69 [53]).

CHAPTER 4. NUMERICAL DISCRETIZATION & SOLUTION PROCEDURE

In this chapter, we will examine the steps and setups adapted for the generation of the numerical system equivalent and used to solve the last system of equations along with the boundary and initial conditions.

4.1 Domain Definition

Note: The Geometrical properties of the experimental nozzle can be found at Appendix B.

Based on a 2D axisymmetric analysis, I divided the domain into three multi-block parts. The convergent part (subsonic region), the divergent part (supersonic region), and the far field exit part. This was in response to the difficulties faced by the complexity of the nozzle geometry, very high curvature, and the requirement of refined mesh near the walls (mesh conformity & quality problem).
This indeed required the use of non-conformal mesh and the introduction of interfaces between the blocks.

- Convergent Part

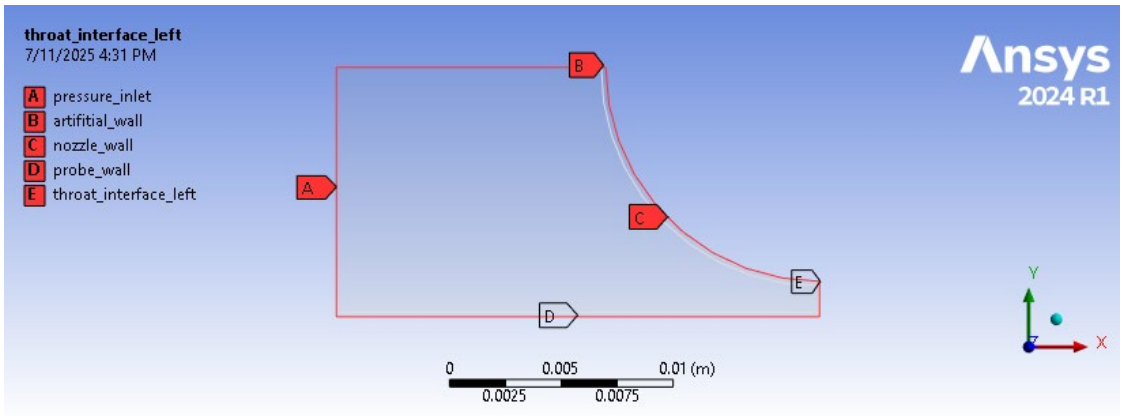

Figure 4.1 : Convergent Part Block.

- Divergent part

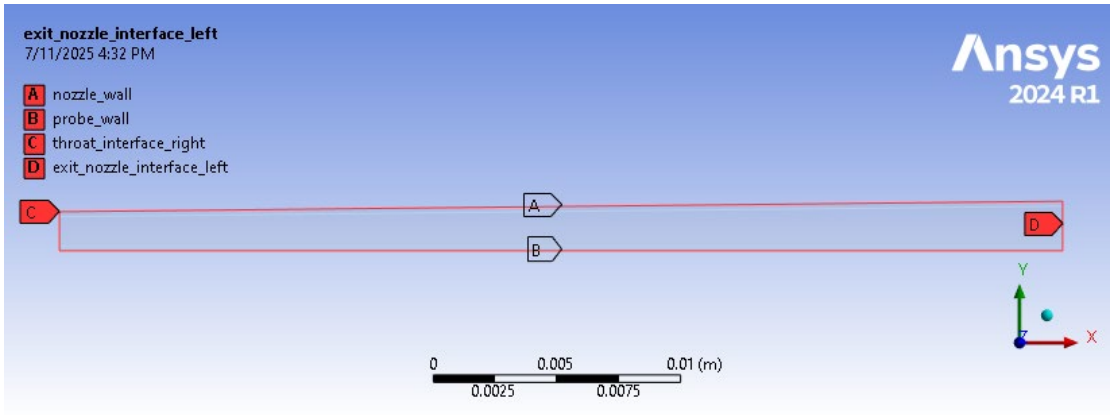

Figure 4.2 : Divergent Part Block.

- Exit Field part

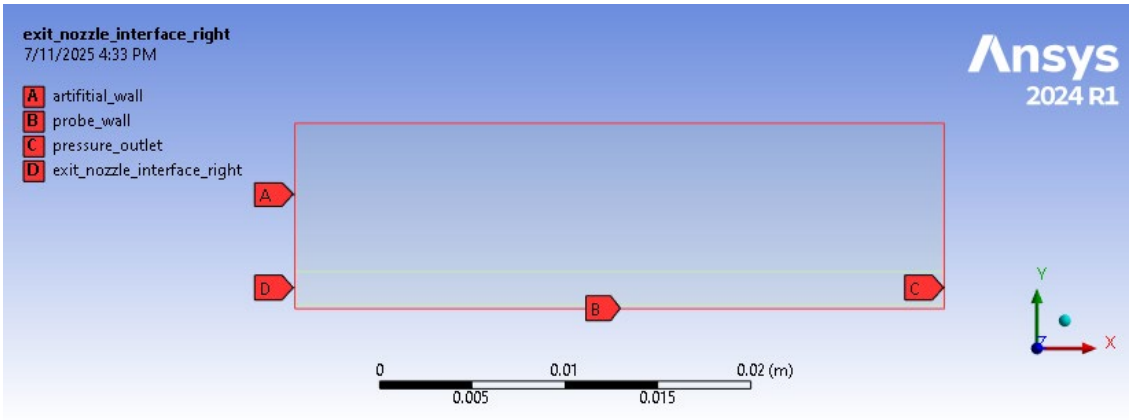

Figure 4.3 : Exit Far field Block.

- Complete assembled domain

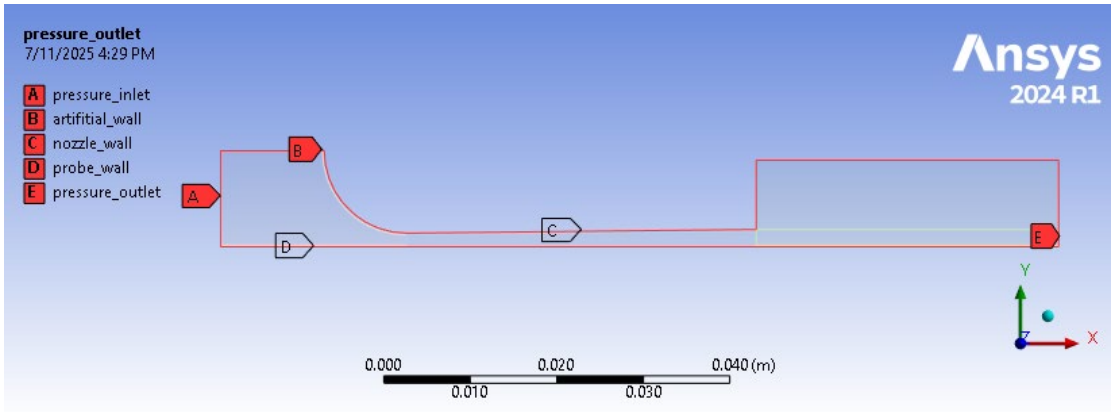

Figure 4.4 : The Complete Numerical Domain.

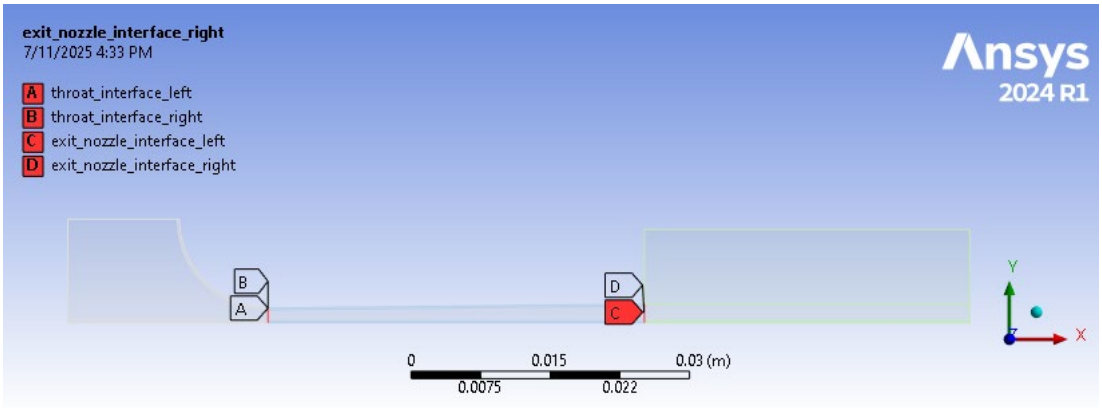

Figure 4.5 : Blocks Interfaces.

4.2 Domain discretization (Meshing)

The domain discretization and mesh generation were done using ANSYS Meshing. A hybrid mesh type was adopted, taking advantage of both structured and unstructured meshes as the conditions required. The study of boundary layer refinement was performed through the inflation function while the method to estimate the thickness of the first layer is given below. As mentioned above, the use of a multi-block domain has as its purpose the use of a non-conformal mesh and the introduction of interfaces (type interior) for the transfer of information (fluxes) across the blocks.

4.2.1 Mesh Proprieties

2D geometries allow the use of two types of cells (Figure 4.6) for domain discretization. The quadrilateral elements as structured mesh and the triangular elements for unstructured mesh. These

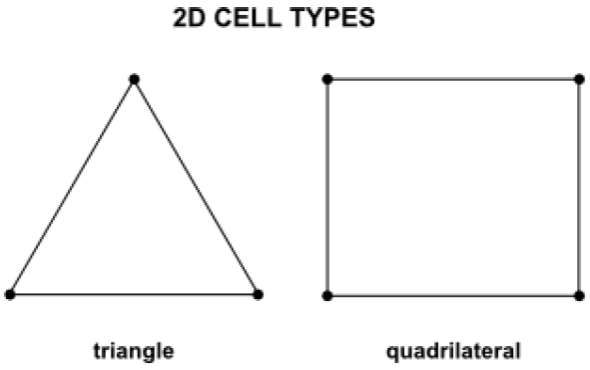

Figure 4.6 : 2D cell types [58].

elements represent an approximation of the original geometry. The sides of the triangles and quadrilaterals are called element edges, and their corners are element vertices (or nodes) [58].

The choice between structured and unstructured meshes depends on several factors, including accuracy, computational efficiency, and adaptability to complex geometries.

- *Structured Mesh:* Offers higher accuracy and lower numerical diffusion, making it ideal for capturing shock waves and boundary layers. Their structured nature enables faster computations and lower memory usage, but it can be difficult to generate for complex geometries.
- *Unstructured Mesh:* Provides flexibility in handling complex geometries and is easier to generate. However, it may introduce more numerical diffusion, which can affect wake and drag predictions. Refining the mesh in critical regions can help mitigate these issues.

A hybrid approach, such as structured-unstructured zonal meshing, can combine the benefits of both methods, improving accuracy while maintaining flexibility.

Mesh Sensibility Analysis

Mesh Number of Elements	Throat mass flow rate [kg/s]	Relative Deviation from the Mean (%)	Average exit Mach number	Relative Deviation from the Mean (%)
62716	0.032807652	0.0182	1.4633943	0.254516
75362	0.032803557	0.005716	1.4675301	0.027382
116869	0.032791912	0.029785	1.4728323	0.388782
140335	0.032803607	0.005869	1.4647568	0.161647

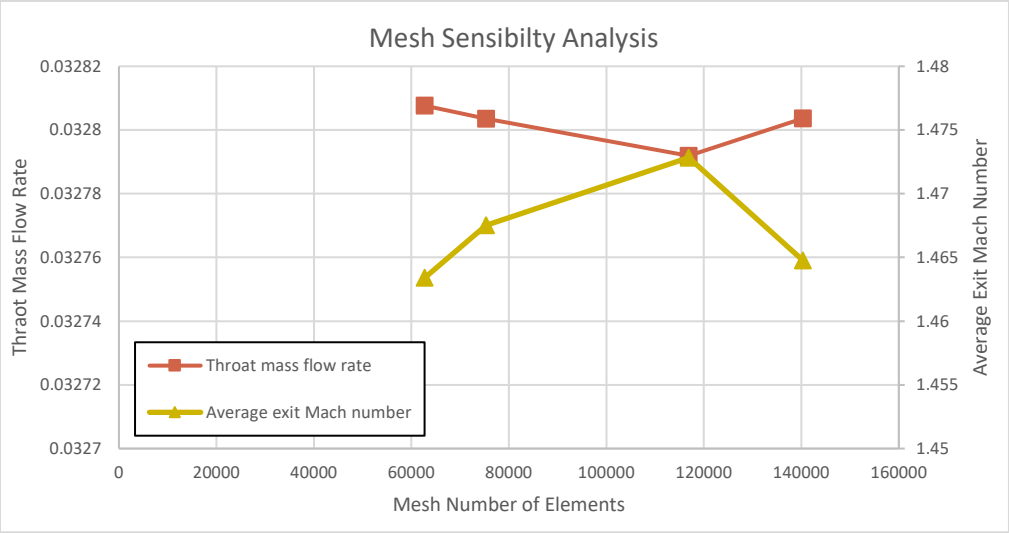

Figure 4.7 : Mesh Sensibility Analysis.

Mesh Statistics

Number of elements	Quadrilaterals elements	Triangles elements	Number of nodes
75362	70952	4410	74541

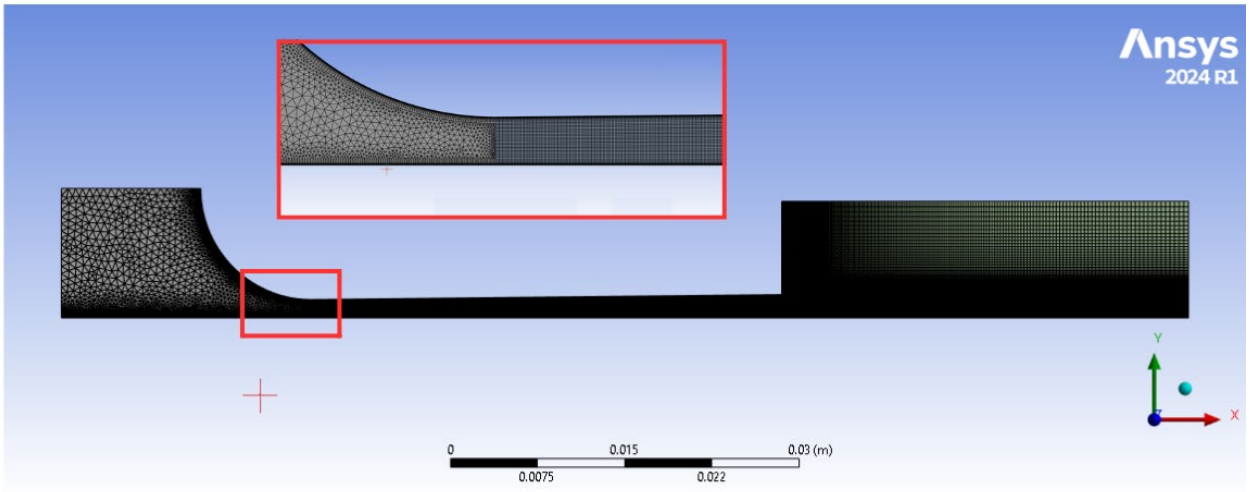

Figure 4.8 : Mesh visualization.

Mesh Quality

Aspect ratio metric

It's the ratio of the longest edge length to the shortest edge length in an element. Its value varies between 1 to infinite while a lower aspect ratio (closer to 1) indicates better quality. Figure 4.9 shows quadrilaterals and triangles with aspect ratios of 1 and 20.

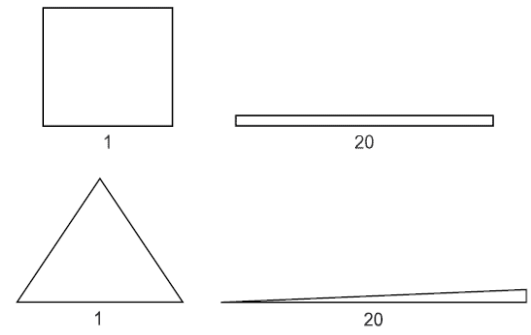

Figure 4.9 : Quadrilateral & triangular elements with aspect ratios 1 and 20 [58].

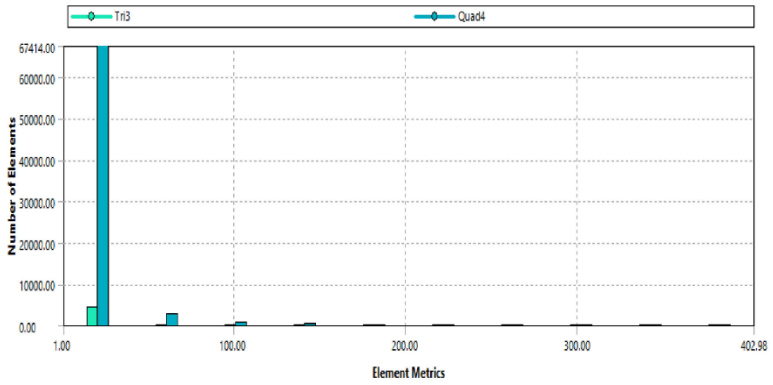

Figure 4.10 : Current mesh aspect ratio assessment.

Skewness metric

Skewness is one of the primary quality metrics for a mesh. Skewness determines how close to ideal (equilateral or equiangular) a face or cell is (see Figure 4.11).

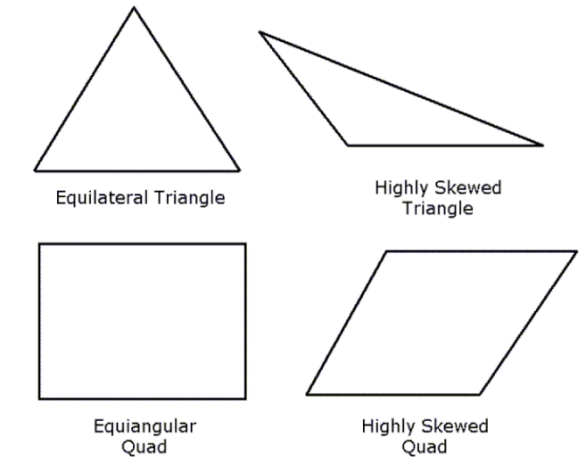

Figure 4.11 : Ideal and Skewed Triangles and Quadrilaterals [58].

According to the definition of skewness, a value of 0 indicates an equilateral cell (best), and a value of 1 indicates a completely degenerated cell (worst). Degenerate cells are characterized by nodes that are nearly coplanar (colinear in 2D).

Highly skewed faces and cells are unacceptable because the equations being solved assume that the cells are relatively equilateral/equiangular.

Two methods for measuring skewness are:

- Based on the equilateral volume (applies only to triangles and tetrahedra). Where the skewness is defined as:

$$skewness = \frac{optimal\ cell\ size - \ cell\ size}{optimal\ cell\ size} \tag{4-1}$$

Where, the optimal cell size is the size of an equilateral cell with the same circumradius.

- Based on the deviation from a normalized equilateral angle. This method applies to all cell and face shapes, including pyramids and prisms. Where the skewness is defined as:

$$skewness = \max\left[\frac{\theta_{max} - \theta_e}{180 - \theta_e}, \frac{\theta_e - \theta_{min}}{\theta_e}\right] \tag{4-2}$$

Here,

θ_{max} : largest angle in the face or cell.
θ_{min} : smallest angle in the face or cell.
θ_e : angle for an equiangular face/cell (60 for a triangle, 90 for a square).

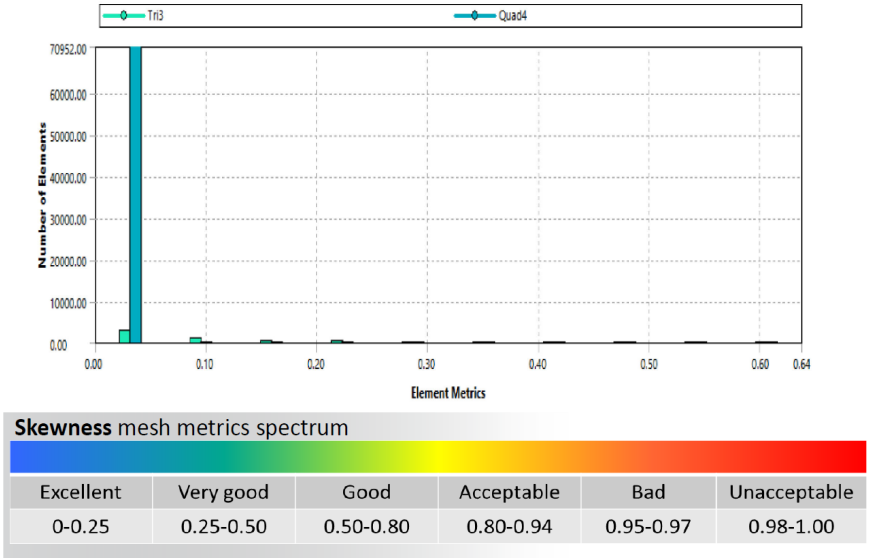

Figure 4.12 : Current mesh skewness assessment.

Orthogonal Quality metric

The range for orthogonal quality is $0 - 1$, where a value of 0 is the worst and a value of 1 is the best.

The orthogonal quality for cells is computed using the face normal vector $\overrightarrow{A_i}$ for each face, the vector from the cell centroid to the centroid of each of the adjacent cells $\overrightarrow{c_i}$, and the vector from the cell centroid to each of the faces $\overrightarrow{f_i}$. Figure 4.13 illustrates the vectors used to determine the orthogonal quality for a cell.

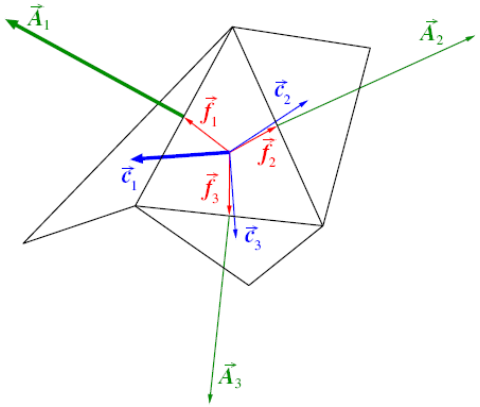

Figure 4.13 : Vectors Used to Compute Orthogonal Quality for a Cell [58].

For each face, the cosines of the angle between $\overrightarrow{A_i}$ and $\overrightarrow{c_i}$, and between $\overrightarrow{A_i}$ and $\overrightarrow{f_i}$, are calculated. The smallest calculated cosine value is the orthogonality of the cell. Finally, orthogonal quality depends on cell type:

- For tetrahedral, prism, and pyramid cells, the orthogonal quality is the minimum of the orthogonality and $(1 - cell\ skewness)$.
- For hexahedral and polyhedral cells, the orthogonal quality is the same as the orthogonality.

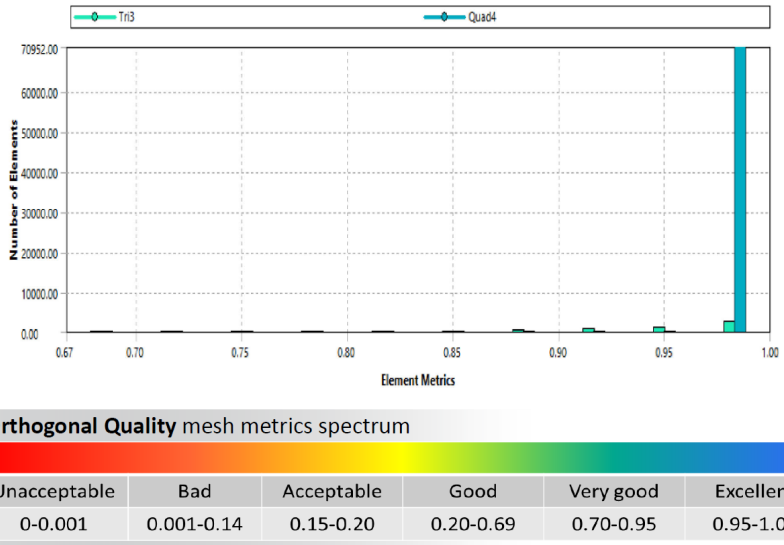

Figure 4.14 : Current mesh orthogonal quality assessment.

4.2.2 Non-Conformal Mesh

In Ansys Fluent it is possible to use a mesh that has non-conformal interfaces, that is, boundaries between cell zones that connect to each other in which the mesh node locations are not identical. Such nonconformal interfaces permit the cell zones to pass fluxes from one mesh to another.

To compute the flux across the non-conformal boundary, Ansys Fluent must first compute the intersection between the interface zones that make up the boundary. In the case of a solid-to-solid zone interface of the same material or a fluid-to-fluid zone interface, the resulting intersection produces an interior zone where the two interface zones overlap (see Figure 4.15). In the case of a solid-to-solid zone interface of different materials or a fluid-to-solid zone interface, the boundary is treated as a coupled wall (see The Coupled Wall Option (p. 1148) [58]).

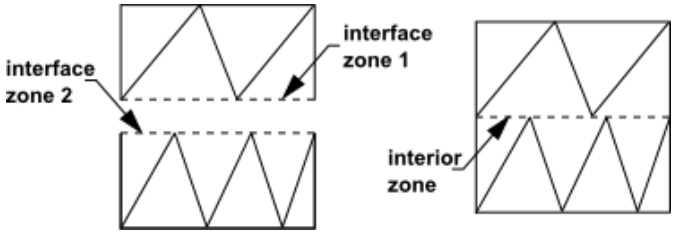

Figure 4.15 : Completely Overlapping Mesh Interface Intersection [58].

If one of the interface zones extends beyond the other (Figure 4.16), by default Ansys Fluent will create additional boundary zones for the portion(s) of the boundary where the two interface zones do not overlap; these are referred to as "non-overlapping zones", and you can change their settings and/or zone type at your discretion [58].

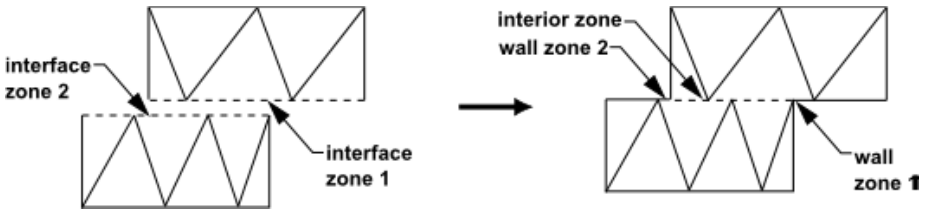

Figure 4.16 : Partially Overlapping Mesh Interface Intersection [58].

Fluxes across the mesh interface are computed using the faces resulting from the intersection of the two interface zones, not from the interface zone faces [58]. In the example shown in Figure 4.17, the interface zones are composed of faces A-B and B-C, and faces D-E and E-F.

The intersection of these zones produces the faces a-d, d-b, b-e, and e-c. Faces produced in the region where the two cell zones overlap (d-b, b-e, and e-c) are grouped to form an interior or coupled wall zone (depending on the types of the adjacent cell zones), while the remaining face (a-d) forms a wall zone.

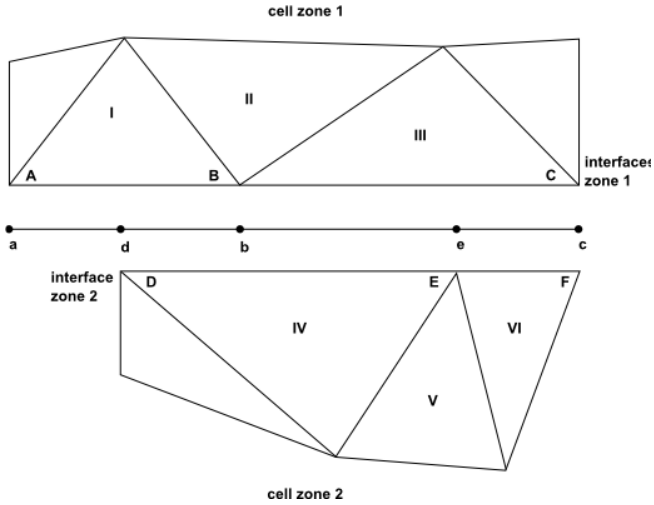

Figure 4.17 : Two-Dimensional Non-Conformal Mesh Interface [58].

To compute the flux across the interface into cell IV, face D-E is ignored and instead faces d-b and b-e are used to bring information into cell IV from cells I and III [58].

While the previous discussion described the default treatment of a non-conformal interface, there are several options you can enable at the interface to revise the treatment of the fluxes and/or reduce the memory usage and processing time:

- Periodic boundary condition.
- Periodic repeats.
- Coupled wall.
- Matching.
- Mapped.
- Static.

For more details on these non-conformal interface options refer to [58].

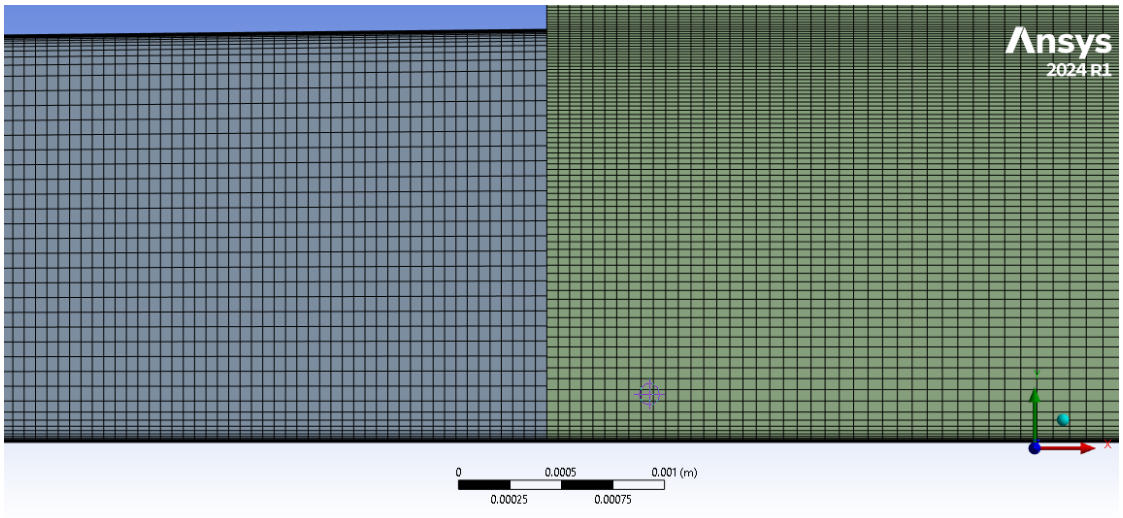

Figure 4.18 : Non-conformal mesh visualization at the interface.

4.2.3 The method used for the estimation of y^+

The dimensionless variable y^+ is a key parameter in the study of turbulent boundary layers. It represents the normalized wall distance in terms of viscous effects and is defined as:

$$y^+ = \frac{y\, u^*}{\nu} \tag{4-3}$$

Where,

- y^+ is the distance from the wall,
- u_τ is the friction velocity ($u_\tau = \sqrt{\frac{\tau_w}{\rho}}$, with τ_w being the wall shear stress),
- ν is the kinematic viscosity of the fluid.

This parameter helps classify different regions in the near-wall turbulence (Figure 4.19): the viscous sublayer ($y^+ < 5$), where molecular diffusion dominates; the buffer layer ($5 < y^+ < 30$), where both viscosity and turbulence interact; and the log-law region ($30 < y^+ < 700$), where fully developed turbulence follows a logarithmic velocity profile; And for $y^+ > 700$, the measured turbulent velocity exceeds the magnitude predicted by the log law and is therefore called the "defect layer" [49].

y^+ is crucial in Computational Fluid Dynamics (CFD) for mesh refinement and turbulence modeling to ensure accurate simulations of near-wall flow behavior.

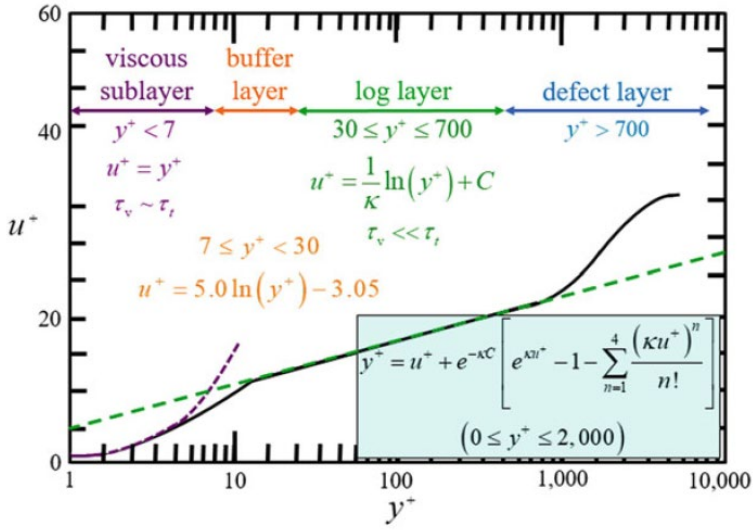

Figure 4.19 : Laminar (viscous), buffer, log, and defect layers [49].

Calculating y based on y^+

To find the value of y (typically, represents the wall-normal distance of the first cell to the wall) for our target dimensionless value of $y^+ \sim 1$ or any, first calculate Re based on the characteristics of the flow. The one-dimensional theory from chapter 1 is used here as reference values for flow variables in the calculations. At this point, it is necessary to obtain the appropriate characteristic length and velocity, x_{char} and u_{char}, so they properly reflect their impact on Re,

$$Re = \frac{\rho\, u_{char}\, x_{char}}{\mu} \tag{4-4}$$

For characteristic length, we will use here the hydraulic diameter based on the values of area ratio A/A^* and throat area A^*, and the characteristic velocity is estimated from 1D theory.

The next step is to calculate the skin friction, C_f, which is defined as

$$C_f = \frac{\tau_w}{\frac{1}{2}\rho u_{char}^2} \tag{4-5}$$

The formulas used in this analysis in based on the work by Lawrence J. De Chant and Marc J. Tattar [59], where they have obtained an analytical skin friction formula for compressible internal flows. The final form of the equation is:

$$\frac{C}{C_f^{1/2}\left[\frac{1}{2}(\gamma-1)M_{av}^2 r\right]} = const + 1.77\ln\left(C_f^{1/2}Re\right) + 1.77\ln(E) - 1.77\left(1 + 0.2121\,Re\frac{k}{D}C_f^{1/2}E\right) \quad (4\text{-}6)$$

Where $const = -0.6005$ for axisymmetric flow or 1.5086 for two-dimensional duct flow, r is the recovery factor for air $r = 0.88$ [59].

And,

$$A' = \left(\frac{T_{av}}{T_w} - 1\right) + \frac{1}{2}(\gamma-1)M_{av}^2\frac{T_{av}}{T_w}$$

$$B' = \left[\frac{1}{2}(\gamma-1)M_{av}^2\frac{T_{av}}{T_w}r\right]^{1/2}$$

$$C = \text{asin}\left[\frac{2B'^2 - A'^2}{\left(4B'^2 + A'^2\right)^{\frac{1}{2}}}\right] + \text{asin}\left[\frac{A'}{\left(4B'^2 + A'^2\right)^{\frac{1}{2}}}\right] \quad (4\text{-}7)$$

$$E = \frac{T_{av}}{T_w}\left[\frac{1.505}{1 + 0.505\frac{T_w}{T_{av}}}\right]$$

For the adiabatic wall, they suggested that,

$$\frac{T_w}{T_{av}} = 1 + \frac{1}{2}(\gamma-1)M_{av}^2 \quad (4\text{-}8)$$

Once C_f is known, it can be used to solve for the wall shear τ_w, Eq. (4-5), which for convenience, is now rewritten as

$$\tau_w = C_f\frac{\rho\, u_{char}^2}{2} \quad (4\text{-}9)$$

Finally, the variable u_τ can be obtained as

$$u_\tau = \sqrt{\frac{\tau_w}{\rho}} \quad (4\text{-}10)$$

Based on the target value of y^+, the thickness of the first cell from the wall, y, can be estimated via Eq. (4-3). Table 4.1 summarizes all the steps.

Table 4.1 : Calculation of y at the desired value of y^+[49].

Step	Equation	Unknowns
1	$Re = \frac{x_{char}\, u_{char}}{\nu}$	Re
2	Eq. (4-6) by Lawrence J. De Chant and Marc J. Tattar [59].	C_f, Re
3	$\tau_w = C_f \frac{\rho u_{cahr}^2}{2}$	τ_w, C_f
4	$u_\tau = \sqrt{\frac{\tau_w}{\rho}}$	u_τ, τ_w
5	$y = \frac{y^+ \nu}{u_\tau}$	y, u_τ

Based on the calculation made on my work for $y^+ \approx 1$, I have estimated a value for y in the range of $1.3 \times 10^{-6}\, m$ as a global value, and I have used a value of $1 \times 10^{-6}\, m$ as the actual value for mesh generation near the wall, see Figure 4.20.

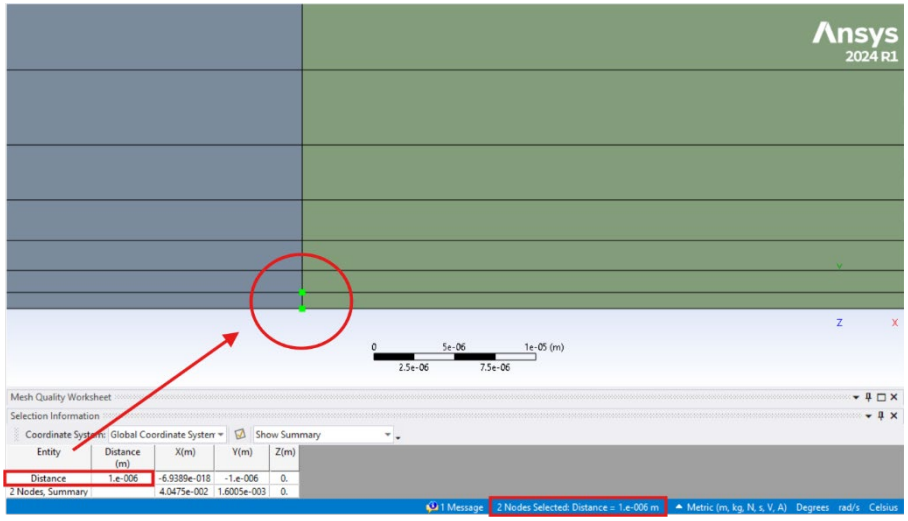

Figure 4.20 : First cell distance assessment.

4.3 Boundary Conditions

Ansys Fluent has a wide range of boundary conditions that permit flow to enter and exit the solution domain. A description of the boundary conditions that have been used along with recommendations for determining inlet values are provided.

4.3.1 Pressure inlet

Pressure inlet boundary conditions are used to define the fluid pressure at flow inlets, along with all other scalar properties of the flow. They are suitable for both incompressible and compressible flow calculations. Pressure inlet boundary conditions can be used when the inlet pressure is known but the flow rate and/or velocity is not known. Pressure inlet boundary conditions can also be used to define a “free” boundary in an external or unconfined flow [58].

I have used the following information for the pressure inlet boundary:

- Type of reference frame.
- Total (stagnation) pressure.
- Total (stagnation) temperature.
- Flow direction.
- Static pressure.
- Turbulence parameters (see Determining Turbulence Parameters).

All values are entered in the Pressure Inlet Dialog Box (Figure 4.21), which is opened from the Boundary Conditions task page.

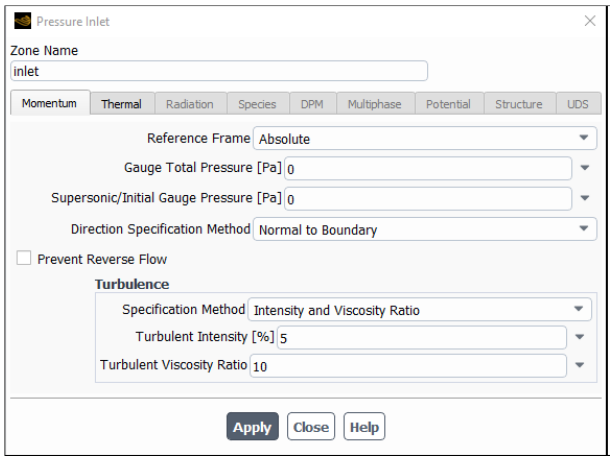

Figure 4.21 : The Pressure Inlet Dialog Box [58].

4.3.2 Pressure Outlet

Pressure outlet boundary conditions require the specification of a static (gauge) pressure at the outlet boundary. The value of the specified static pressure is used only while the flow is subsonic. Should the flow become locally supersonic, the specified pressure will no longer be used; pressure will be extrapolated from the flow in the interior (domain). All other flow quantities are extrapolated from the interior [58].

I selected the following information for a pressure outlet boundary:

- Static pressure.
- Pressure profile multiplier.
- Backflow conditions.
  - Backflow pressure specification.
  - Backflow direction specification method.
- Total (stagnation) temperature (for energy calculations).
- Turbulence parameters (see Determining Turbulence Parameters).

All values are entered in the Pressure Outlet Dialog Box (Figure 4.22), which is opened from the Boundary Conditions task page.

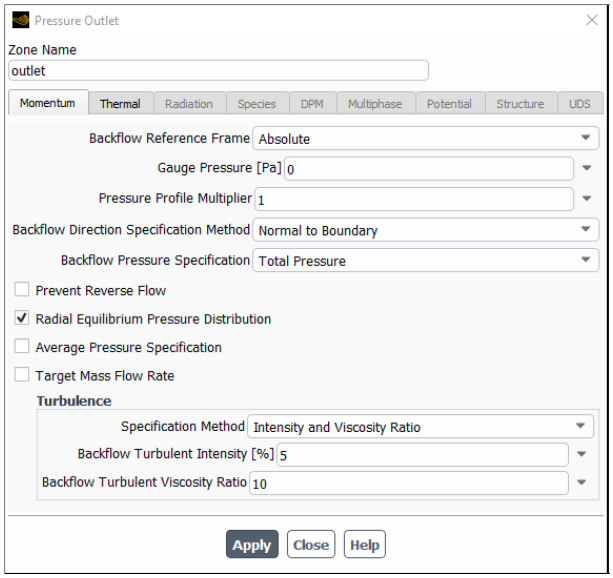

Figure 4.22 : The Pressure Outlet Dialog Box [58].

4.3.3 Wall Boundary Conditions

Wall boundary conditions are used to bind fluid and solid regions. In viscous flows, the no-slip boundary condition is enforced at walls by default, but you can specify a tangential velocity component in terms of the translational or rotational motion of the wall boundary, or model a “slip” wall by specifying shear. (You can also model a slip wall with zero shear using the symmetry boundary type, but using a symmetry boundary will apply symmetry conditions for all equations. See Symmetry Boundary Conditions, [58]).

The shear stress and heat transfer between the fluid and wall are computed based on the flow details in the local flow field.

Shear Conditions at Walls

Two types of shear conditions have been used:

- No-slip.
- Specified shear.

The no-slip condition is the default, and it indicates that the fluid sticks to the wall and moves with the same velocity as the wall, if it is moving. The specified shear boundary condition is useful in modeling situations in which the shear stress (rather than the motion of the fluid) is known. Examples of such situations are applied shear stress, slip wall (zero shear stress), and free surface conditions (zero shear stress or shear stress dependent on surface tension gradient). The specified shear boundary condition allows you to specify the x, y, z and components of the shear stress as constant values or profiles [58].

Shear conditions are entered in the Momentum tab of the Wall Dialog Box, which is opened from the Boundary Conditions Task Page.

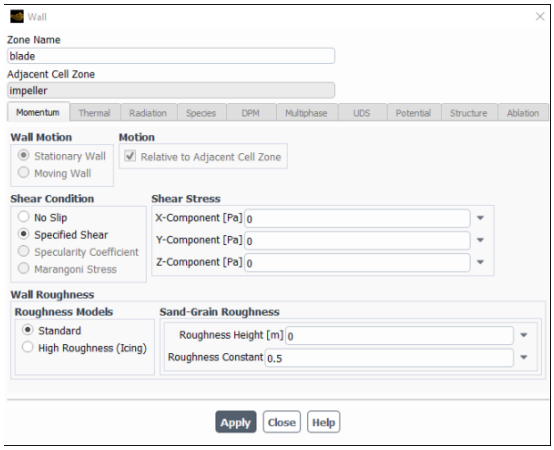

Figure 4.23 : The Wall Dialog Box for Specified Shear [58].

Thermal Boundary Conditions at Walls

When you are solving the energy equation, you need to define thermal boundary conditions at wall boundaries. The walls have been modeled as adiabatic walls by setting a zero-heat flux condition which is the default condition.

Thermal conditions are entered in the Thermal tab of the Wall Dialog Box (Figure 4.24), which is opened from the Boundary Conditions task page.

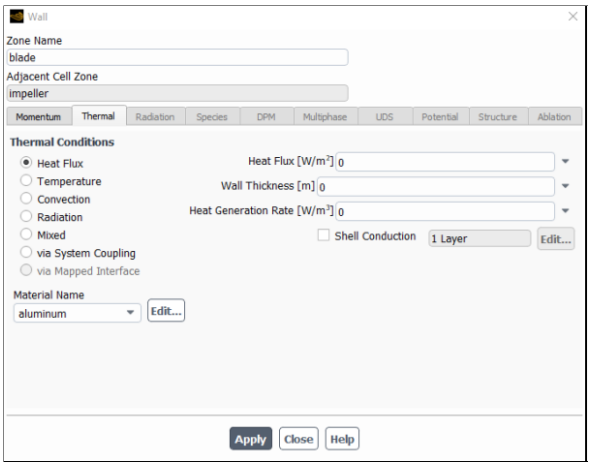

Figure 4.24 : The Wall Dialog Box (Thermal Tab) [58].

4.3.4 Determining Turbulence Parameters

Default values of turbulence parameters have been used because no information on the inlet non- on the outlet boundaries could be reached in the basis of the experiment. This default value expresses moderate turbulence (medium intensity) [58].

For more details about the specification of transported turbulence quantities. Refer to [58]. Or use any online turbulent quantities ‘calculator (ex. [60]).

4.4 Initiating the Solution

Before starting a CFD simulation, you must provide Ansys Fluent with an initial “guess” for the solution flow field. In many cases, you must take extra care to provide an initial solution that will allow the desired final solution to be attained. A real-life supersonic wind tunnel, for example, will not “start” if the back pressure is simply lowered to its operating value; the flow will choke at the tunnel throat and will not transition to supersonic. The same holds for a numerical simulation: the flow must be initialized to a supersonic flow or it will simply choke and remain subsonic [53].

There are two methods for initializing the solution, [53]:

- Initialize the entire flow field (in all cells). Three methods are available:
  - Standard initialization.
  - Hybrid initialization.
  - FMG initialization.
- Patch values or functions for selected flow variables in selected cell zones or cell registers.

4.4.1 Standard Initialization

In this method, the entire flow field is initiated with constant cell values, where you can compute the values from information in a specified zone, enter them manually, or have the solver compute average values based on all zones. You can also indicate whether the specified values for velocities are absolute or relative to the velocity in each cell zone [53].

4.4.2 Hybrid Initialization

Hybrid Initialization is a collection of recipes and boundary interpolation methods. It solves the Laplace equation to produce a velocity field that conforms to complex domain geometries, and a pressure field that smoothly connects high- and low-pressure values in the computational domain. All other variables (that is temperature, turbulence, VOF, species, and so on) will be patched based on domain-averaged values or a predetermined recipe [53].

4.4.3 Full Multigrid (FMG) Initialization

For many complex flow problems such as those found in rotating machinery, or flows in expanding or spiral ducts, flow convergence can be accelerated if a better initial solution is used at the start of the calculation. The Full Multigrid initialization (FMG initialization) can provide this initial and approximate solution at a minimum cost to the overall computational expense.

FMG initialization utilizes the Ansys Fluent FAS Multigrid technology (see [53]) to obtain the initial solution. Starting from a uniform solution (after performing standard or hybrid initialization or reading data), the FMG initialization procedure constructs the desirable number of geometric grid levels using the procedure outlined in Full-Approximation Storage (FAS) Multigrid [53]. To

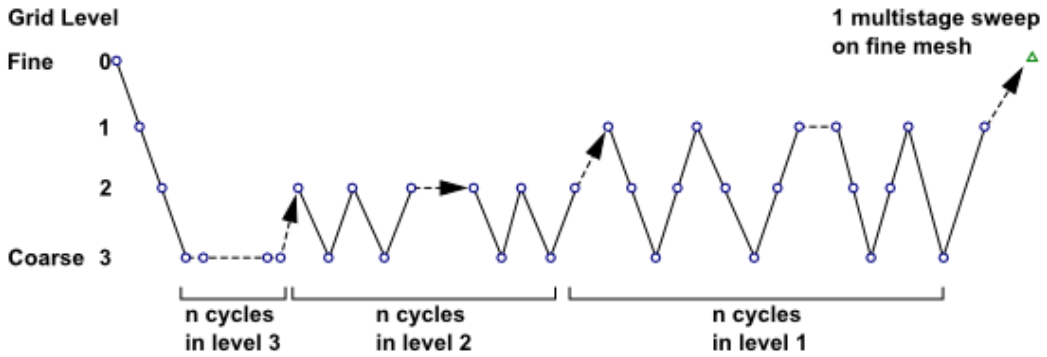

Figure 4.25 : The FMG Initialization [53].

begin the process, the initial solution is restricted all the way down to the coarsest level. The FAS multigrid cycle is then applied until a given order of residual reduction is obtained or the maximum number of cycles is reached. The solution is then interpolated one grid level up and the FAS multigrid cycle is applied again between the current level all the way down to the coarsest level. This process will repeat until the finest level is reached. The FMG initialization iteration is illustrated in Figure 4.25.

Since FMG initialization does most of the work on coarse levels, this initialization procedure is computationally inexpensive, and for large problems, a good initial solution can be obtained in a fraction of the time spent to converge on a final solution. Note that FMG initialization can be used with the pressure-based and density-based solvers [53].

When FMG initialization is started, the algorithm will perform the following steps:

1. Records the current solver selection and all current solver parameters.
2. Switches from the selected solver to the density-based explicit formulation.
3. Performs one FMG iteration using the FMG parameters given in the text command interface.
4. Switches back to the initially selected solver and resets all solver parameters back to the original solver settings.

In the FMG iteration, the Euler equations for inviscid flow are solved using first-order discretization to obtain the approximate solution [53]. If species are present, then the FMG initialization will solve the species equations. While turbulence equations or any other transport scalars are not solved during the FMG initialization cycles, their values will be updated once after the final FMG sweep on the fine mesh using the latest velocity and pressure fields [53].

Limitations of FMG Initialization

- FMG initialization is not available for unsteady flows.
- FMG will not solve turbulence or other transport equations field variables.
- FMG cannot be used with multiphase flow.

4.5 General Scalar Transport Equation: Discretization and Solution

Ansys Fluent uses a control-volume-based technique (Finite Volume Method) to convert a general scalar transport equation to an algebraic equation that can be solved numerically [53]. This control

volume technique consists of integrating the transport equation about each control volume, yielding a discrete equation that expresses the conservation law on a control-volume basis.

Discretization of the governing equations can be illustrated most easily by considering the unsteady conservation equation for the transport of a scalar quantity ϕ. This is demonstrated by the following equation written in integral form for an arbitrary control volume V as follows, [53]:

$$\int_V \frac{\partial \rho \phi}{\partial t} dV + \oint \rho \phi \vec{V} \cdot d\vec{A} = \oint \Gamma_\phi \nabla \phi \cdot d\vec{A} + \int_V S_\phi dV \tag{4-11}$$

Where,

ρ : density.

$\vec{V}$: Velocity vector.

$\vec{A}$: surface area vector.

Γ_ϕ : diffusion coefficient for ϕ.

$\nabla \phi$: gradient of ϕ.

S_ϕ : source term of ϕ per unit volume.

Eq. (4-25) is applied to each control volume, or cell, in the computational domain. The two-dimensional, triangular cell shown in Figure 4.26 is an example of such a control volume. Discretization of Eq. (4-25) on a given cell yields, [53]:

$$\frac{\partial \rho \phi}{\partial t} V + \sum_f^{N_{faces}} \rho_f \phi_f \overrightarrow{V_f} \cdot \overrightarrow{A_f} = \sum_f^{N_{faces}} \Gamma_\phi \nabla \phi_f \cdot \overrightarrow{A_f} + S_\phi V \tag{4-12}$$

Where,

N_{faces} : number of faces enclosing cell.

ϕ_f: value of ϕ convected through face f.

$\rho_f \vec{V}_f \cdot \vec{A}_f$: mass flux through the face.

$\vec{A}_f$: area vector of face f.

$\nabla \phi_f$: gradient of ϕ at face f.

V : cell volume.

Where $\frac{\partial \rho \phi}{\partial t} V$ is defined in Temporal Discretization. The equations solved by Ansys Fluent take the same general form as the one given above and apply readily to multi-dimensional, unstructured meshes composed of arbitrary polyhedral [53].

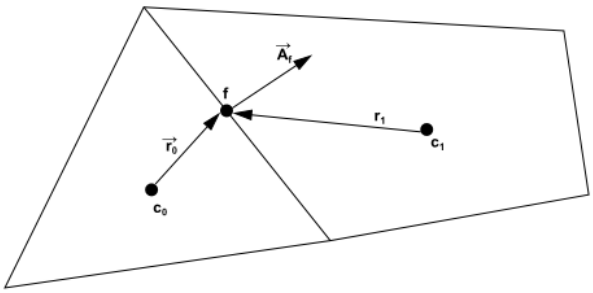

Figure 4.26 : Control Volume Used to Illustrate Discretization of a Scalar Transport Equation [53].

4.5.1 Solving the Linear System

The discretized scalar transport equation (Eq. (4-26)) contains the unknown scalar variable ϕ at the cell center as well as the unknown values in surrounding neighbor cells. This equation will, in general, be non-linear with respect to these variables. A linearized form of Eq. (4-26) can be written as, [53]:

$$a_p \phi = \sum_{nb} a_{nb} \phi_{nb} + b \tag{4-13}$$

where the subscript "nb" refers to neighbor cells, and a_p and a_{nb} are the linearized coefficients for ϕ and ϕ_{nb}. The number of neighbors for each cell depends on the mesh topology, but will typically equal the number of faces enclosing the cell (boundary cells being the exception) [53]. Similar equations can be written for each cell in the mesh. This results in a set of algebraic equations with a sparse coefficient matrix. For scalar equations, Ansys Fluent solves this linear system using a point implicit (Gauss-Seidel) linear equation solver in conjunction with an algebraic multigrid (AMG) method that is described in Algebraic Multigrid (AMG), [53].

4.5.2 Equations Discretization

Spatial Discretization

By default, Ansys Fluent stores discrete values of the scalar ϕ at the cell centers (c_0 and c_1 in Figure 4.26). However, face values ϕ_f are required for the convection terms in Eq. (4-26) and must be interpolated from the cell center values. This is accomplished using an upwind scheme.

Upwinding means that the face value ϕ_f is derived from quantities in the cell upstream, or "upwind," relative to the direction of the normal velocity V_n in Eq. (4-26). Ansys Fluent allows you to choose from several upwind schemes: first-order upwind, second-order upwind, and QUICK [53].

The diffusion terms in Eq. (4-26) are central-differenced and are always second-order accurate [53].

Temporal Discretization

For transient simulations, the governing equations must be discretized in both space and time. The spatial discretization for the time-dependent equations is identical to the steady-state case. Temporal discretization involves the integration of every term in the differential equations over a time step Δt. The integration of the transient terms is straightforward, as shown below.

A generic expression for the time evolution of a variable ϕ is given by

$$\frac{\partial \phi}{\partial t} = F(\phi) \tag{4-14}$$

Where the function F incorporates any spatial discretization. If the time derivative is discretized using backward differences, the first-order accurate temporal discretization is given by

$$\frac{\phi^{n+1} - \phi^n}{\Delta t} = F(\phi) \tag{4-15}$$

and the second-order discretization is given as described in Second-Order Time Integration Using a Variable Time Step Size [58].

Where

ϕ: is scalar quantity.

$n+1$: value at the next time level, $t + \Delta t$.

n : value at the next time level, t.

Once the time derivative has been discretized, a choice remains for evaluating $F(\phi)$: in particular, which time level values of ϕ should be used in evaluating. This give rise to the implicit and explicit formulations.

Evaluation of Gradients and Derivatives

Gradients are needed not only for constructing values of a scalar at the cell faces, but also for computing secondary diffusion terms and velocity derivatives. The gradient $\nabla\phi$ of a given variable ϕ is used to discretize the convection and diffusion terms in the flow conservation equations. The gradients are computed in Ansys Fluent according to the following methods, [53]:

- Green-Gauss Cell-Based
- Green-Gauss Node-Based
- Least Squares Cell-Based

4.6 Density-Based Solver

The density-based solver solves the governing equations of continuity, momentum, and (where appropriate) energy and species transport simultaneously (that is, coupled together). Governing equations for additional scalars will be solved afterward and sequentially (that is, segregated from one another and the coupled set) using the procedure described in General Scalar Transport Equation: Discretization and Solution [53]. Because the governing equations are nonlinear (and coupled), several iterations of the solution loop must be performed before a converged solution is obtained. Each iteration consists of the steps illustrated in Figure 4.27 and outlined below:

1. Update the fluid properties based on the current solution. (If the calculation has just begun, the fluid properties will be updated based on the initialized solution.)
2. Solve the continuity, momentum, and (where appropriate) energy and species equations simultaneously.
3. Where appropriate, solve equations for scalars such as turbulence and radiation using the previously updated values of the other variables.
4. When the interphase coupling is to be included, update the source terms in the appropriate continuous phase equations with a discrete phase trajectory calculation.
5. Check for convergence of the equation set.

These steps are continued until the convergence criteria are met [58].

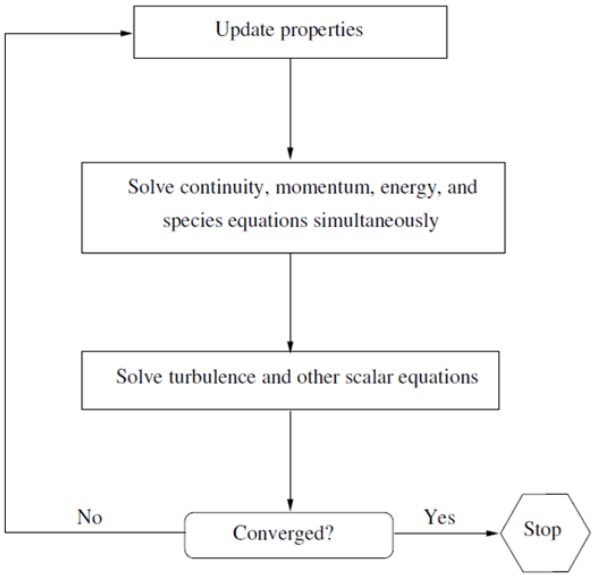

Figure 4.27 : Overview of the Density-Based Solution Method [58].

In the density-based solution method, the coupled system of equations (continuity, momentum, energy and species equations if available) is linearized to produce a system of algebraic equations for the dependent variables in every computational cell. The manner in which the governing equations are linearized may take an "implicit" or "explicit" form with respect to the dependent variable (or set of variables) of interest [58]. By implicit or explicit we mean the following:

- **Implicit:** For a given variable, the unknown value in each cell is computed using a relation that includes both existing and unknown values from neighboring cells. Therefore, each unknown will appear in more than one equation in the system, and these equations must be solved simultaneously to give the unknown quantities.
- **Explicit:** For a given variable, the unknown value in each cell is computed using a relation that includes only existing values. Therefore, each unknown will appear in only one equation in the system and the equations for the unknown value in each cell can be solved one at a time to give the unknown quantities.

In summary, the coupled implicit approach solves all variables (P, u, v, w, T) in all cells at the same time. Whereas, the density-based explicit approach solves for all variables (P, u, v, w, T) one cell at a time [58].

4.6.1 Governing Equations in Vector Form

The system of governing equations for a single-component fluid, written to describe the mean flow properties, is cast in integral Cartesian form for an arbitrary control volume V with differential surface area dA as follows:

$$\frac{\partial}{\partial t}\int_V W\, dV + \oint [F - G]\cdot dA = \int_V H\, dV \tag{4-16}$$

where the vectors W, F and G are defined as

$$W = \begin{Bmatrix} \rho \\ \rho u \\ \rho v \\ \rho w \\ \rho E \end{Bmatrix}, F = \begin{Bmatrix} \rho\vec{V} \\ \rho u\,\vec{V} + P\,\hat{\imath} \\ \rho v\,\vec{V} + P\,\hat{\jmath} \\ \rho w\,\vec{V} + P\,\hat{k} \\ (\,\rho E + P)\,\vec{V} \end{Bmatrix}, G = \begin{Bmatrix} 0 \\ \vec{\tau}_{1i} \\ \vec{\tau}_{2i} \\ \vec{\tau}_{3i} \\ \vec{\tau}_{ij}u_j + q \end{Bmatrix} \tag{4-17}$$

In Eq. (4-39) W is called the solution vector because the elements in W are the dependent variables which are usually obtained numerically in steps of time; the column vectors F and G are called the flux terms (or flux vectors), and H represents a source term (which is zero if body forces and volumetric heating are negligible). And Here ρ, $\vec{V}$, E, and P are the density, velocity, total energy per unit mass, and pressure of the fluid, respectively. τ is the viscous stress tensor, and q is the heat flux.

Total energy E is related to the total enthalpy H by

$$E = H - P/\rho \tag{4-18}$$

Where

$$H = h + \left|\vec{V}\right|^2/2 \tag{4-19}$$

The Navier-Stokes equations as expressed in Eq. (4-39) become (numerically) very stiff at low Mach numbers due to the disparity between the fluid velocity and the acoustic speed (speed of sound). This is also true for incompressible flows, regardless of the fluid velocity, because acoustic waves travel infinitely fast in an incompressible fluid (the speed of sound is infinite). The numerical stiffness of the equations under these conditions results in poor convergence rates. This difficulty is overcome in Ansys Fluent's density-based solver by employing a technique called (time-derivative) preconditioning [53].

4.6.2 Convective Fluxes

Roe Flux-Difference Splitting Scheme

The inviscid flux vector appearing in Eq. (4-39) is evaluated by a standard upwind, flux-difference splitting [53]. This approach acknowledges that the flux vector contains characteristic information propagating through the domain with speed and direction according to the eigenvalues of the system. By splitting into parts, where each part contains information traveling in a particular direction (that is, characteristic information), and upwind differencing the split fluxes in a manner consistent with their corresponding eigenvalues.

This formulation can be viewed as a second-order central difference plus an added matrix dissipation [53]. The added matrix dissipation term is not only responsible for producing an upwinding of the convected variables, and of pressure and flux velocity in supersonic flow, but it also provides the pressure-velocity coupling required for stability and efficient convergence of low-speed and incompressible flows [53].

AUSM+ Scheme

An alternative way to compute the flux vector appearing in Eq. (4-39) is by using a flux-vector splitting scheme [53]. The scheme called the Advection Upstream Splitting Method (AUSM), was first introduced by Liou and Steffen in 1993 [53]. The AUSM scheme first computes a cell interface Mach number based on the characteristic speeds from the neighboring cells. The interface Mach number is then used to determine the upwind extrapolation for the convection part of the inviscid fluxes. A separate Mach number splitting is used for the pressure terms. Generalized Mach number-based convection and pressure splitting functions were proposed by Liou and the new scheme was termed AUSM+ [53]. The AUSM+ scheme has several desirable properties:

- Provides exact resolution of contact and shock discontinuities.
- Preserves positivity of scalar quantities.
- Free of oscillations at stationary and moving shocks.

4.6.3 Steady-State Flow Solution Methods

The coupled set of governing equations Eq. (4-39) in Ansys Fluent is discretized in time for both steady and unsteady calculations [53]. In the steady case, it is assumed that time marching proceeds

until a steady-state solution is reached. Temporal discretization of the coupled equations is accomplished by either an implicit or an explicit time-marching algorithm [53].

Marching solution concept

Exploring the ramifications of Eq. (4-39) further. It is written with a time derivative $\frac{\partial W}{\partial t}$; hence it applies to an unsteady flow. In a given problem, the actual transients in an unsteady flow may be of primary interest. In other problems, a steady-state solution may be desired but wherein the best manner to solve for this steady state is to solve the unsteady equations and let the steady state be approached asymptotically at large times. (This approach is sometimes called the time-dependent solution of steady flows). For either an inherently transient solution, or a time-dependent solution leading to a steady state, the solution of Eq. (4-39) takes the form of a time-marching solution, i.e., where the dependent flow-field variables are solved progressively in steps of time. For such a time-marching solution, we isolate $\frac{\partial W}{\partial t}$ by rearranging Eq. (4-39) [61].

In CFD, marching solutions are not limited to marching just in time. Under certain circumstances, steady-state flows can also be solved by marching in a given spatial direction. The circumstances that allow the use of a spatially marching solution depend on the mathematical properties of the governing equation [61].

Stability Criterion and CFL-based solution

Stability in numerical methods ensures that errors do not amplify uncontrollably over time, keeping the solution well-bounded. It is crucial for solving differential equations, especially when dealing with stiff systems or long-time simulations. Stability analysis helps determine whether a numerical method will produce a reliable solution or diverge due to accumulating errors [61]. Two methods are often invoked for stability analysis the Eigenvalue Method and Von Neumann Stability Analysis [61].

The CFL (Courant-Friedrichs-Lewy) condition is a crucial stability criterion in time-marching schemes for solving partial differential equations (PDEs) numerically. It ensures that the time step Δt is small enough relative to the spatial discretization to maintain numerical stability, particularly for explicit methods [61].

The CFL condition states that for stability:

$$\frac{\Delta \mathrm{t}}{\Delta x} \leq \frac{1}{|\lambda|} \tag{4-20}$$

Where,

Δt : is the time step,

Δx : is the spatial gird resolution,

λ : represents the wave speed or characteristic velocity of the system.

For different equations,

Advection Equation: $\lambda = u$, so the CFL condition becomes $\frac{\Delta t}{\Delta x} \leq \frac{1}{|u|}$.

Diffusion Equation: $\lambda = \alpha$, where α is the diffusion coefficient, requiring $\frac{\Delta t}{\Delta x^2} \leq \frac{1}{2}$.

Wave Equation: $\lambda = c$, where c is the wave speed.

CFL-Based Solution Approach

1. **Choose an appropriate discretization scheme** (Explicit Euler, Runge-Kutta, Lax-Wendroff, etc.).
2. **Determine the maximum wave speed** in the problem.
3. **Compute the stable time step** using $\Delta t \leq C \frac{\Delta x}{|\lambda|}$. where C is the CFL number (typically between 0.1 and 1).
4. **March in time using the computed Δt** while checking the CFL stability criterion at each step.
5. **Ensure convergence to a steady-state solution**, if applicable.

4.6.4 Under-relaxation technique

Under-relaxation is a numerical technique used in iterative solvers to enhance stability and prevent divergence by controlling the update step in each iteration. Instead of applying the full computed correction, an under-relaxation factor (ω) between 0 and 1 is introduced to gradually adjust the solution, following the formula

$$Q_{new} = Q_{old} + \omega \, \Delta Q \tag{4-21}$$

Where Q is the solution vector.

This method is widely used in computational fluid dynamics (CFD), nonlinear equation solvers, and optimization problems where abrupt changes may lead to oscillatory or unstable behavior. By

carefully choosing (ω), the solver can balance fast convergence and numerical stability, ensuring smooth and reliable results.

4.6.5 Residuals and Convergence criteria

Residuals measure the difference between the current approximate solution and the exact solution (or next iteration). They indicate how much the solution deviates from satisfying the governing equations.

The residual R^i is computed from the intermediate solution Q^i and, for Eq. (4-39) is given by

$$R^i = \sum^{N_{faces}} \left(F\left(Q^i\right) - G\left(Q^i\right)\right) \cdot A - V\,H \tag{4-22}$$

This are called the absolute residuals. While, relative residuals are defined as the change of the absolute residuals between two subsequent iterations divided by the absolute residual.

$$\hat{R} = \frac{R_{interationN} - R_{interationN-1}}{R_{interationN}} \tag{4-23}$$

Then convergence is reached when the solution approaches a steady or correct result as iterations progress. Common convergence criteria include:

- **Residual-based convergence:** Iterations stop when $|R^N| < \epsilon$, where ϵ is a predefined tolerance.
- **Relative error convergence:** $\left|\hat{R}^N\right| < \delta$, ensuring that successive solutions change insignificantly.

If the method fails to meet the criteria within a set number of iterations, adjustments may be required.

4.7 Solution Strategies for Compressible Flows

The difficulties associated with solving compressible flows are a result of the high degree of coupling between the flow velocity, density, pressure, and energy. This coupling may lead to instabilities in the solution process and, therefore, may require special solution techniques in order to obtain a converged solution [58]. In addition, the presence of shocks (discontinuities) in the flow introduces an additional stability problem during the calculations. Solution techniques that may be beneficial in compressible flow calculations include the following:

- (Pressure-based solver only) Initialize the flow to be near stagnation (that is velocity small but not zero, pressure to inlet total pressure, temperature to inlet total temperature). Turn off the energy equation for the first 50 iterations. Leave the energy under-relaxation at 1. Set the pressure underrelaxation to 0.4, and the momentum under-relaxation to 0.3. After the solution stabilizes and the energy equation has been turned on, increase the pressure under-relaxation to 0.7.
- Set reasonable limits for the temperature and pressure (in the Solution Limits Dialog Box [58]) to avoid solution divergence, especially at the start of the calculation. If Ansys Fluent prints messages about temperature or pressure being limited as the solution nears convergence, the high or low computed values may be physical, and you must change the limits to allow these values.
- If required, begin the calculations using a reduced pressure ratio at the boundaries, increasing the pressure ratio gradually in order to reach the final desired operating condition. If the Mach number is low, you can also consider starting the compressible flow calculation from an incompressible flow solution (although the incompressible flow solution can in some cases be a rather poor initial guess for the compressible calculation).
- In some cases, computing an inviscid solution as a starting point may be helpful.

CHAPTER 5. RESULTS AND DISCUSSIONS

5.1 Overview of The Experimental Setup

Cold Test Experiments were conducted using the TQ-AF27 Apparatus at the Laboratory of Aerodynamics and Heat Transfer, situated within the Higher School of Aeronautical Techniques (ESTA) in Dar-El-Beida.

The AF27 facility serves as a comprehensive platform for studying the thermodynamic and fluid mechanics principles governing the adiabatic expansion of air through subsonic and supersonic nozzles. It provides valuable insights into how nozzle geometry influences airflow characteristics, including mass flow rate, pressure distribution, and expansion behavior.

By simulating real-world applications, such as steam and gas turbines, the facility reinforces fundamental laws governing the expansion of compressible fluids through nozzles. Additionally, it enables the investigation of key flow phenomena, including choked flow—where sonic velocity

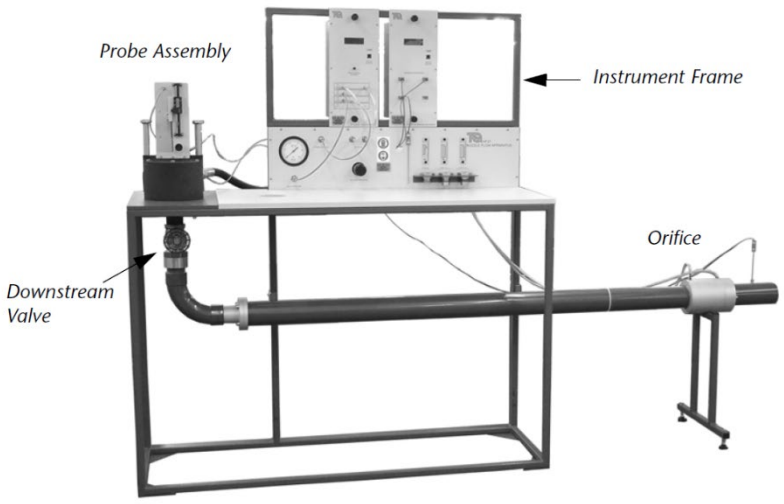

Figure 5.1 : The Nozzle Flow Apparatus.

is attained at the nozzle throat—and variations in nozzle operation under off-design and adapted conditions.

5.1.1 Description of the Apparatus

The nozzle flow apparatus utilizes a separate compressed air source to provide airflow for experimentation. An adjustable regulator controls the maximum air pressure entering the pressure chest, while a shut-off valve controls the flow. The air enters the pressure chest and passes downwards through one of three interchangeable nozzles.

Once the air exits the nozzle, it discharges into a vertical pipe fitted with a throttling valve, which controls the nozzle downstream pressure. The airflow then moves through a curved section before entering a straight pipe, allowing it to stabilize. Before leaving the system, the air passes through an orifice, which plays a key role in measuring the mass flow rate.

The apparatus is equipped with a digital pressure display that monitors chest pressure, pressure within the nozzle probe assembly, ambient pressure, and differential pressure across the orifice. The cylindrical 'constant area' probe assembly measures the static pressures at successive transverse planes along the nozzle axis, with a sensing hole positioned at a fixed distance from the probe tip. A digital indicator records probe movement along the nozzle length, while a mimic plate, graduated in 2 mm interval marks, provides a visual reference for the sensing hole's position.

To ensure reliability, the system includes an analog pressure gauge that offers chest pressure readings even in case of electrical failure. A digital temperature display measures ambient air

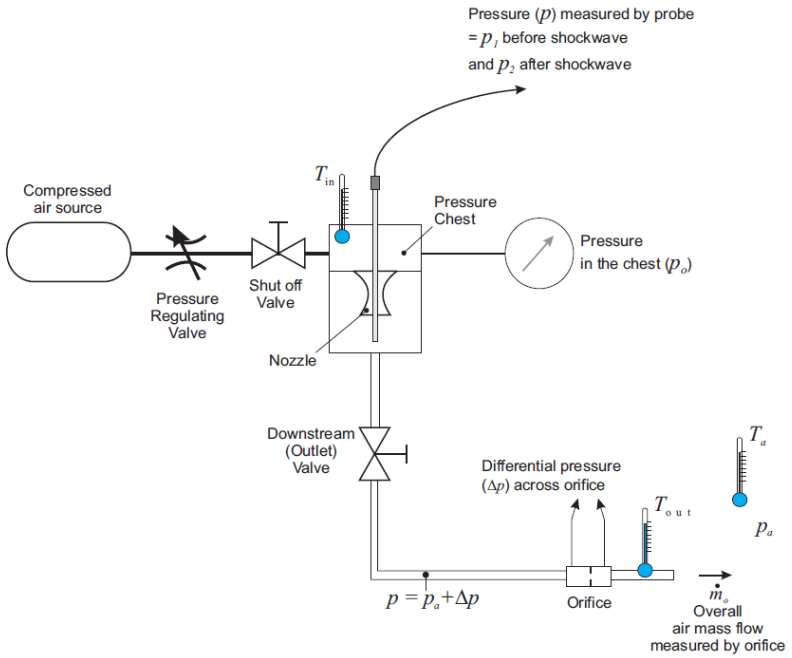

Figure 5.2 : Schematic Layout of the AF27.

temperature, as well as temperatures inside the pressure chest and downstream of the orifice. These temperature and pressure readings help determine mass flow through the apparatus.

5.1.2 Versatile Data Acquisition System (VDAS)

TecQuipment's VDAS is an optional extra for the Nozzle Flow Apparatus. It is a two-part product (Hardware and Software) that can:

- Automatically log data from your tests.
- Automatically calculate data for you.
- Create charts and tables of your data.
- Export your data for processing in other software.

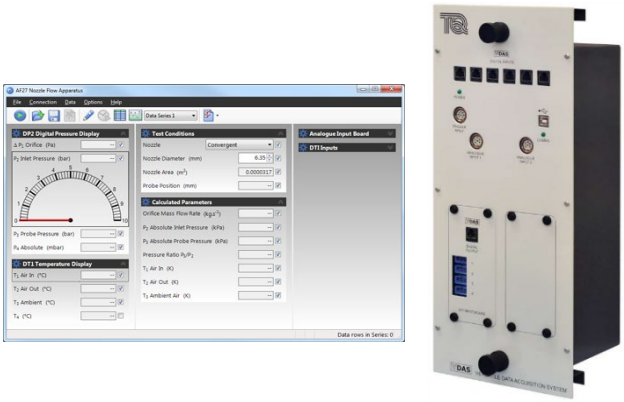

Figure 5.3 : The VDAS Hardware and Software.

5.1.3 Technical Specifications

Table 5.1: Apparatus Technical Specifications.

Orifice	Pressure Probe	Pressure Display	Temperature Display
Diameter 50 mm Area $= 0.001963m^2$ $Cd = 0.62$	Nominal diameter 3.2 mm	▪ $\Delta P1$: Two input (differential) pressure transducer - 2000 Pa. ▪ $P2$: Single input - 10 bar (gauge). ▪ $P3$: Single input - 10 bar (gauge). ▪ $P4$: (Internal) Absolute Atmospheric Pressure.	Four inputs, $T1$ to $T4$: K-type connections. Temperatures displayed in $°C$.

5.1.4 Nozzles

Three nozzles are supplied with the apparatus.

Convergent Nozzle

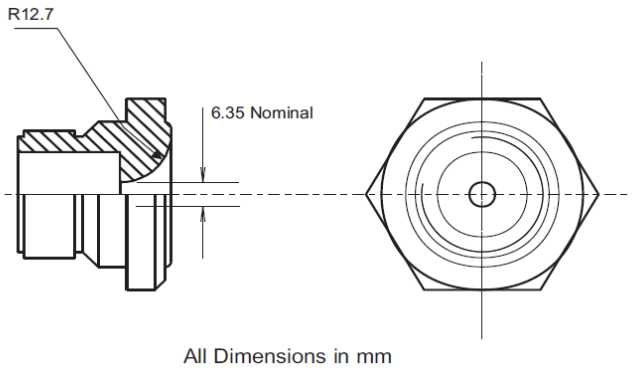

Figure 5.4 : Convergent Nozzle.

Convergent-divergent (or 'Laval') Nozzle

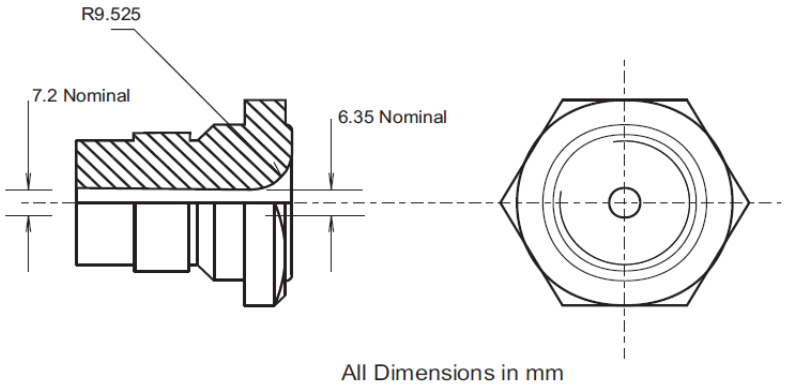

Figure 5.5 : The Convergent-Divergent Nozzle.

Convergent Nozzle with a Parallel Extension

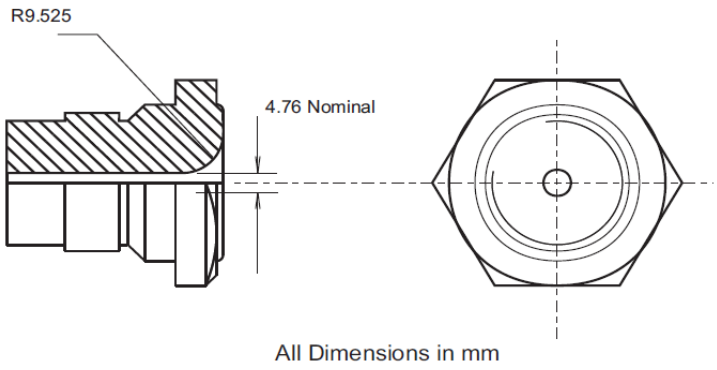

Figure 5.6 : The Convergent - Parallel Nozzle.

5.1.5 Experimental Procedures

The RENNER Kompressoren RSF-H series, screw compressor, is used as a high-pressure air source. Maintained for a target pressure of 7 bar, it first fills an accumulator tank with compressed air.

Compressed air filters are installed before the apparatus connection to remove water, dirt, oil, and other contaminants.

Once the tank is full, we press and hold the reset button to zero the recorded pressure values of the pressure display before opening the shut-off valve. Similarly, the digital position recorder must be calibrated to the zero-reference value position, for that, we use the mimic to set up this position upstream of the nozzle.

At this stage, compressor noise is already significant, but it increases further when airflow begins, so ear defenders are obligatory.

As we open the valve. First, we adjust the pressure (gauge) of the chest to a mid-value of 5 bar. Even for such simple setup, it's yet difficult to achieve a steady-state operation as the pressure oscillates down and up over a certain range.

Secondly, we move the probe all the way downstream the nozzle, and then, we set up the downstream pressure (gauge) through the downstream valve, monitoring its value via the recorded probe value. This pressure represents the back or simulated ambient pressure at which the nozzle operates. Be sure that, at the time you fix its value, the recorded chest pressure is effectively 5 bar,

and this rule should be the same for all the measurements. Then, upload the value into the computer using VDAS.

Finally, move the probe across different points along the nozzle while continuously uploading values. Again, make sure that at the moment when you upload the data values, the chest pressure is effectively 5 bar.

Once all data are recorded, visualize the results within VDAS for quality assessment and, if necessary, remeasure specific values for better accuracy. After collecting the complete dataset, export it in an Excel file.

The same loop applies for the next tests, move the probe downstream and adjust the downstream pressure to its new value, while keeping the same chamber (chest) pressure for all tests.

Figure 5.7 : Picture of the complete experimental setup.

5.1.6 The different experimental tests data

Table 5. 2 : Tests Data's.

Test	NPR	Chamber Pressure, $P_0\ [bar]$ (gauge)	Downstream Pressure, $P_a\ [bar]$ (gauge)	Ambient Pressure, $P_{atm}\ [mbar]$ (absolute)	Chamber Temperature, $T_0\ [K]$
1	4.84988	5.0	0.23	1009	296.95
2	3.5058	5.0	0.7	1016	301
3	3.141	5.0	0.9	1015	301
4	2.8575	5.0	1.09	1015	302.35
5	2.5878	5.0	1.31	1014	300.75
6	2.3922	5.0	1.5	1014	301.45
7	1.9695	5.0	2.04	1013	300.05
8	1.7076	5.0	2.51	1009	298.15
9	1.4911	5.0	3.02	1012	300.65
10	1.3353	5.0	3.49	1013	302.25
11	1.16	5.0	4.13	1015	301.65

5.2 Numerical vs Experimental Probe Pressure Distribution

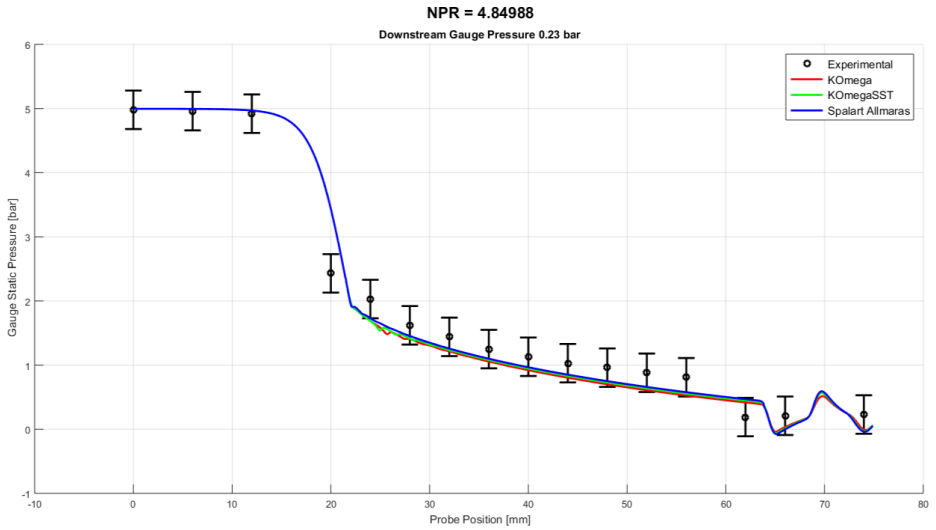

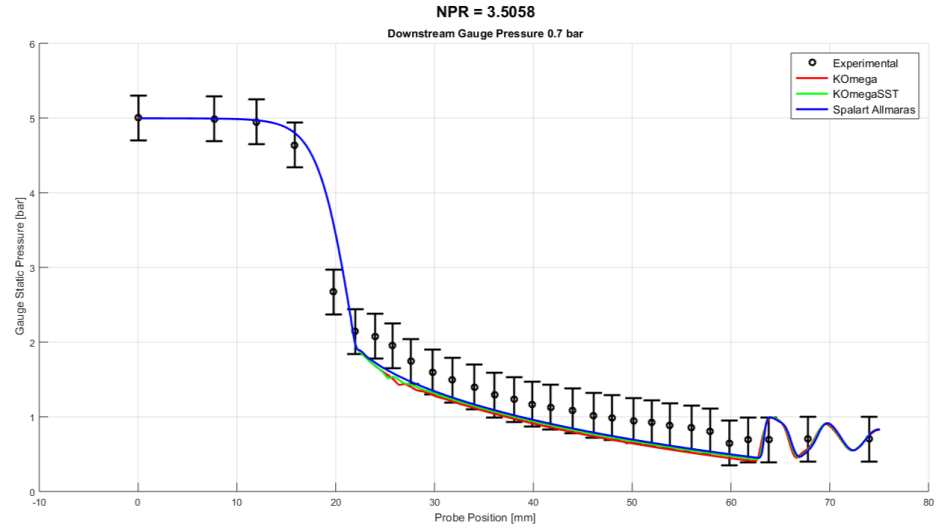
NPR = 3.5058
Downstream Gauge Pressure 0.7 bar
Experimental
KOmega
KOmegaSST
Spalart Allmaras
Gauge Static Pressure [bar]
Probe Position [mm]

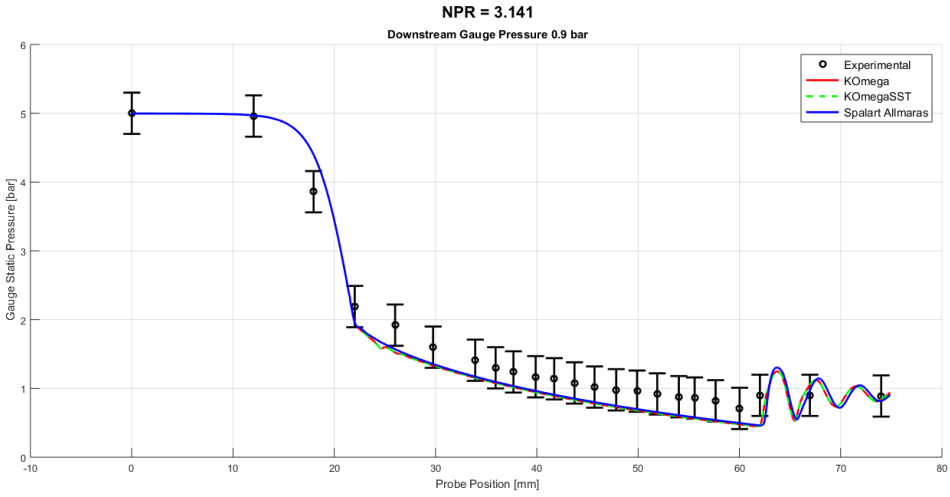
NPR = 3.141
Downstream Gauge Pressure 0.9 bar
Experimental
KOmega
KOmegaSST
Spalart Allmaras
Gauge Static Pressure [bar]
Probe Position [mm]

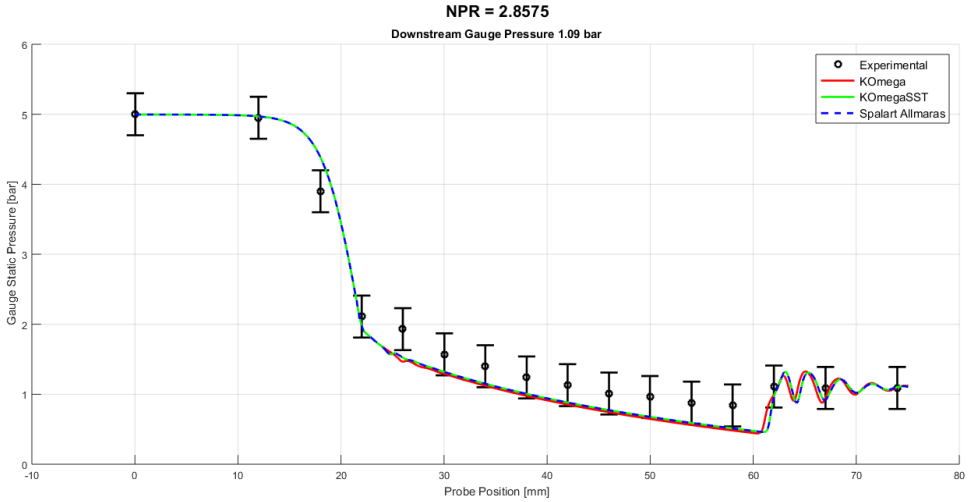
NPR = 2.8575
Downstream Gauge Pressure 1.09 bar
Experimental
KOmega
KOmegaSST
Spalart Allmaras
Gauge Static Pressure [bar]
Probe Position [mm]

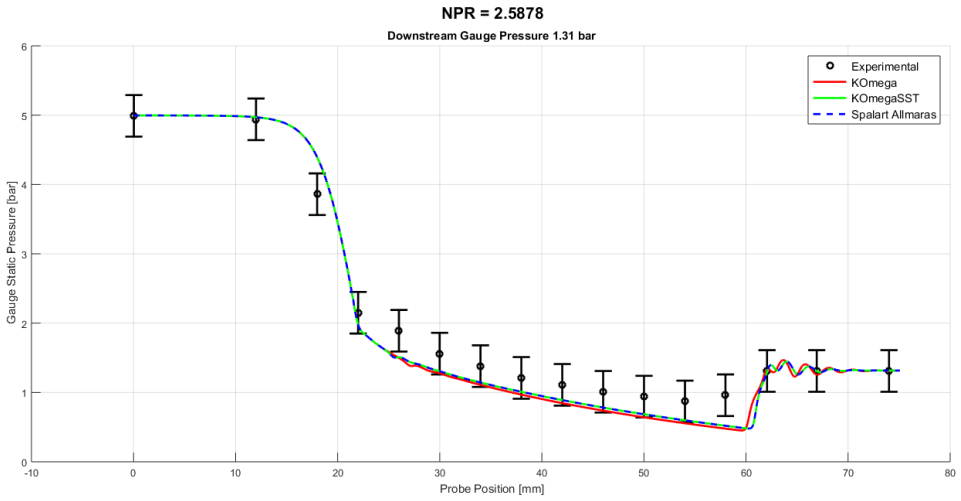
NPR = 2.5878
Downstream Gauge Pressure 1.31 bar
Experimental
KOmega
KOmegaSST
Spalart Allmaras
Gauge Static Pressure [bar]
Probe Position [mm]

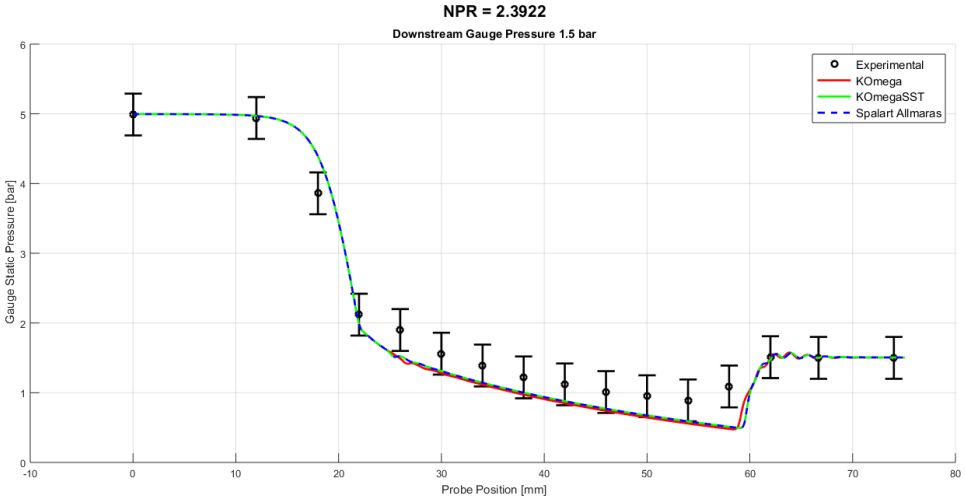
NPR = 2.3922
Downstream Gauge Pressure 1.5 bar
Experimental
KOmega
KOmegaSST
Spalart Allmaras
Gauge Static Pressure [bar]
Probe Position [mm]

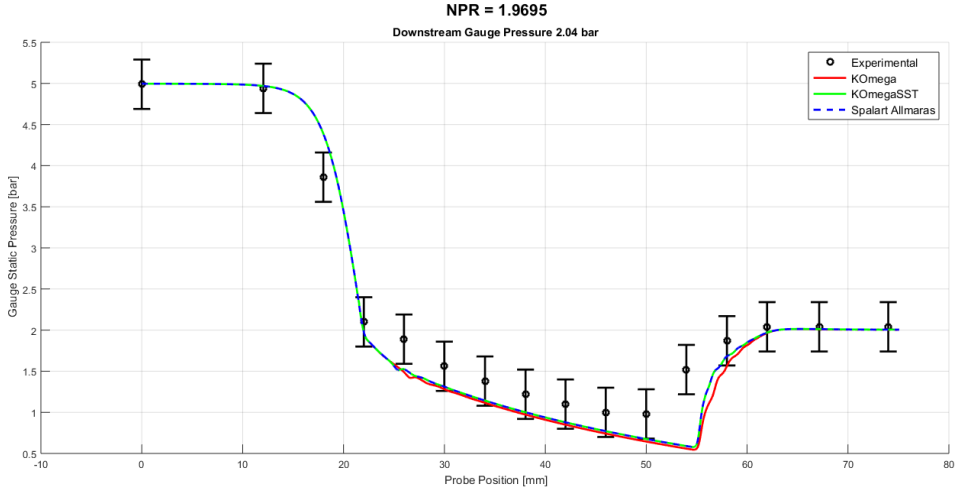
NPR = 1.9695
Downstream Gauge Pressure 2.04 bar
Experimental
KOmega
KOmegaSST
Spalart Allmaras
Gauge Static Pressure [bar]
Probe Position [mm]

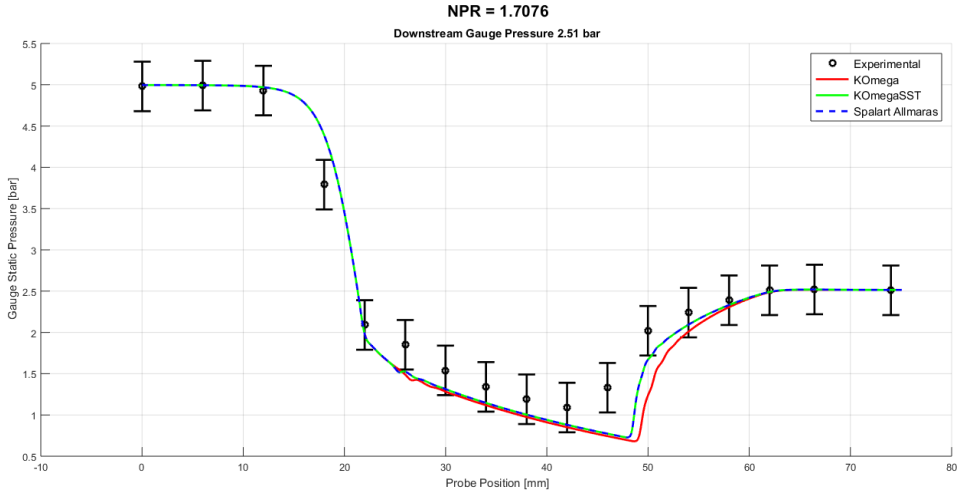
NPR = 1.7076
Downstream Gauge Pressure 2.51 bar
Experimental
KOmega
KOmegaSST
Spalart Allmaras
Gauge Static Pressure [bar]
Probe Position [mm]

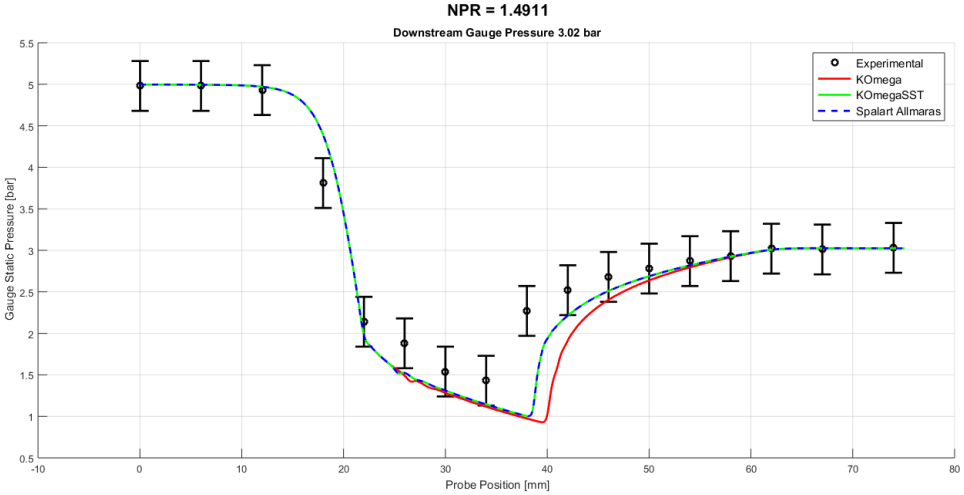
NPR = 1.4911
Downstream Gauge Pressure 3.02 bar
Experimental
KOmega
KOmegaSST
Spalart Allmaras
Gauge Static Pressure [bar]
Probe Position [mm]

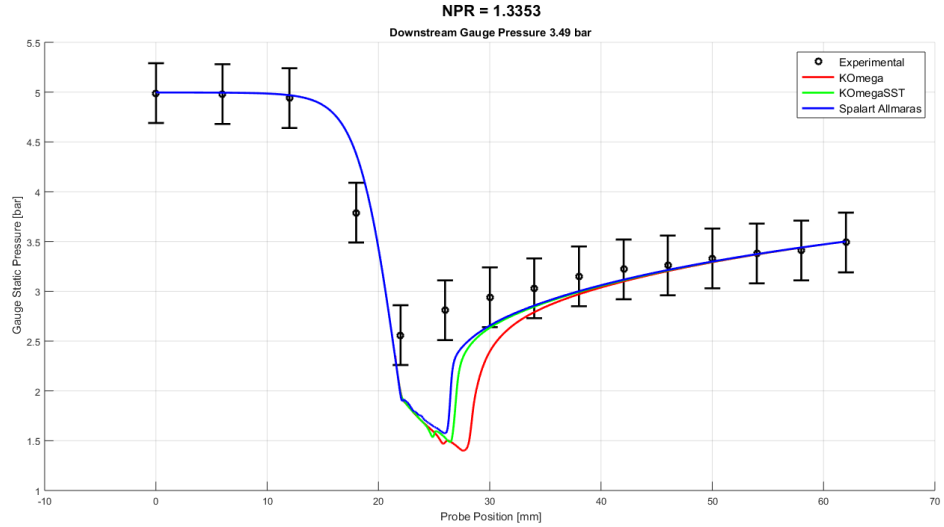
NPR = 1.3353
Downstream Gauge Pressure 3.49 bar
Experimental
KOmega
KOmegaSST
Spalart Allmaras
Gauge Static Pressure [bar]
Probe Position [mm]

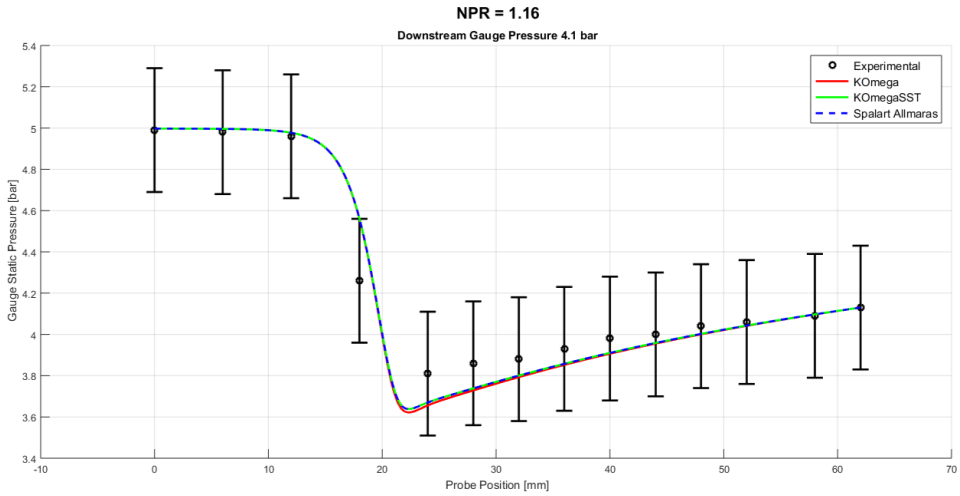

In the preceding graphs, gauge pressure values where used instead of absolute pressure. Both the experimental and numerical results demonstrate excellent coherence, exhibiting only a small error offset. This error is estimated to range from a maximum of 50% down to nearly 0%, with a global average of 12%, as visually represented by the constant error bars of 0.3 bar. This discrepancy is likely attributable to unsteady fluctuations in chamber pressure, which can significantly affect measurement accuracy.

Additionally, static pressure probes are essential tools for measuring static pressure in fluid flows. However, their presence and design can introduce various effects and errors that influence the accuracy of experimental measurements. The following factors illustrate how these probes can affect results:

1. ***Boundary Layer Effects****:* A static pressure tap that is not flush with the wall (either protruding or recessed) can introduce errors due to boundary layer interaction and local disturbances.
2. ***Shock Wave Formation:*** In supersonic flows, the probe itself can generate shock waves. These waves may significantly alter the pressure field, causing the measured static pressure to deviate from the true freestream value.
3. ***Pressure Tap Location and Size:*** The location and diameter of the pressure taps are critical. Larger holes can introduce more pronounced errors, particularly in wall static pressure measurements, by causing local recirculation within the cavity. Similarly, protruding or recessed taps induce errors from flow disturbances at the tap.
4. ***Response Time****:* The length and diameter of the tubing connecting the pressure tap to the transducer can affect the response time of the measurement, particularly for unsteady pressures. Long, thin tubes can smooth out high-frequency content and introduce a time lag.
5. ***Sensor Characteristics:*** The pressure transducer itself may contribute to measurement inaccuracies due to:

- *Zero-point error:* Drift in the instrument's baseline reading over time.
- *Span error:* Deviations in the full-scale reading.
- *Non-linearity:* The signal may not remain proportional to the pressure across the entire range.
- *Temperature sensitivity:* Fluctuations in temperature may alter sensor output.
- *Mechanical wear or damage:* Physical deterioration of the sensor's diaphragm can lead to erroneous readings.

6. ***Calibration:*** Proper calibration of the entire measurement system (probe + tubing + transducer) is crucial to account for the inherent errors and characteristics of the setup.

In terms of a purely numerical comparison of turbulence models, the Spalart-Allmaras model demonstrated the best agreement with the experimental data. The SST $k-\omega$ model followed, showing improved accuracy compared to the Standard $k-\omega$ model, which, in many cases, exhibited similarities when compared with the Spalart-Allmaras predictions.

These findings are consistent with those reported in the literature ([58], [49]), underscoring the Spalart-Allmaras model's unique advantages, particularly its robustness and stability in steady-state simulations. It has demonstrated faster convergence and reduced susceptibility to numerical instabilities when compared to the two-equation models during our simulations. Originally developed for aerodynamic applications, the model delivers enhanced accuracy in predicting shock-wave boundary layer interactions involving mild separation, closely reflecting the characteristics of the current study.

In the following sections, all numerical results will be presented using the Spalart-Allmaras model.

5.3 Numerical Mach Number Contours

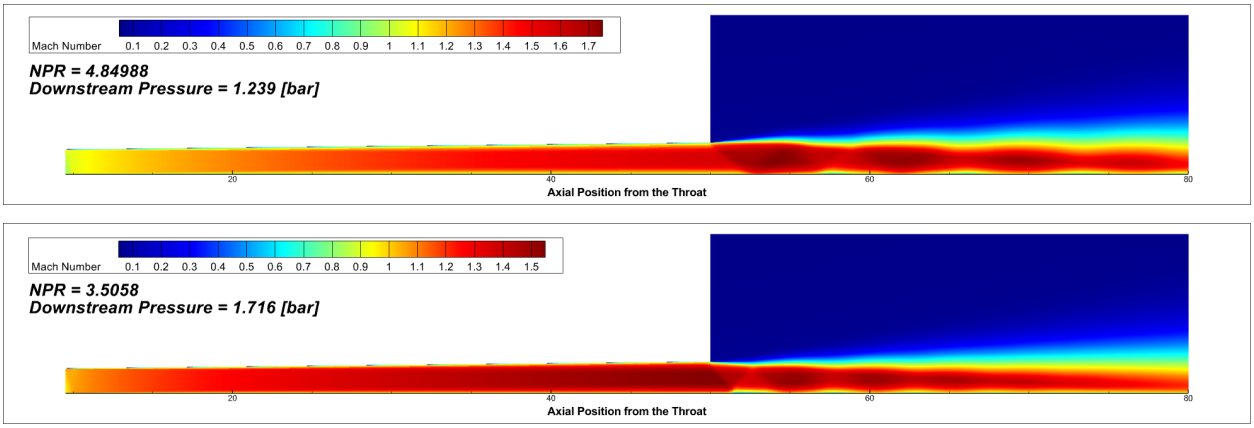

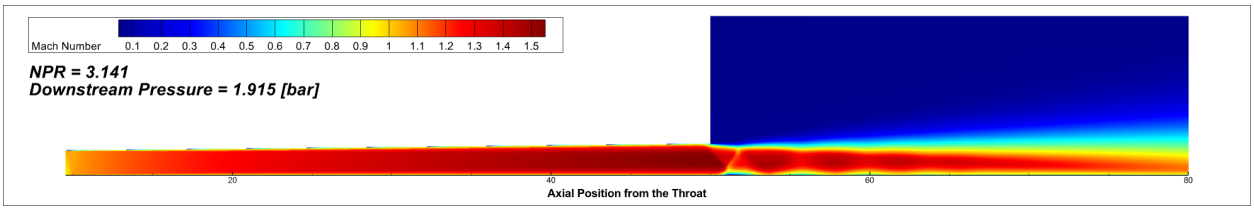
Mach Number 0.1 0.2 0.3 0.4 0.5 0.6 0.7 0.8 0.9 1 1.1 1.2 1.3 1.4 1.5
NPR = 3.141
Downstream Pressure = 1.915 [bar]
20 40 60 80
Axial Position from the Throat

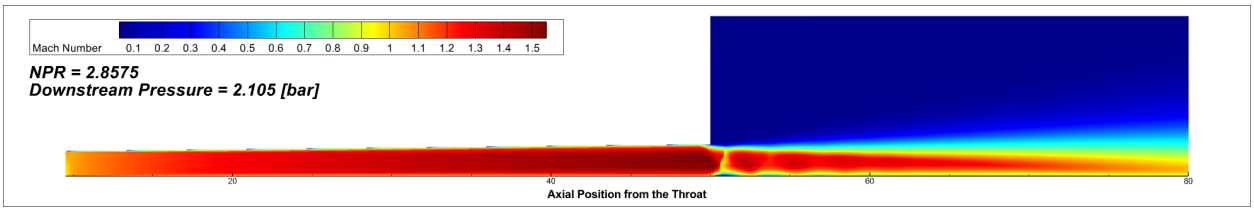
Mach Number 0.1 0.2 0.3 0.4 0.5 0.6 0.7 0.8 0.9 1 1.1 1.2 1.3 1.4 1.5
NPR = 2.8575
Downstream Pressure = 2.105 [bar]
20 40 60 80
Axial Position from the Throat

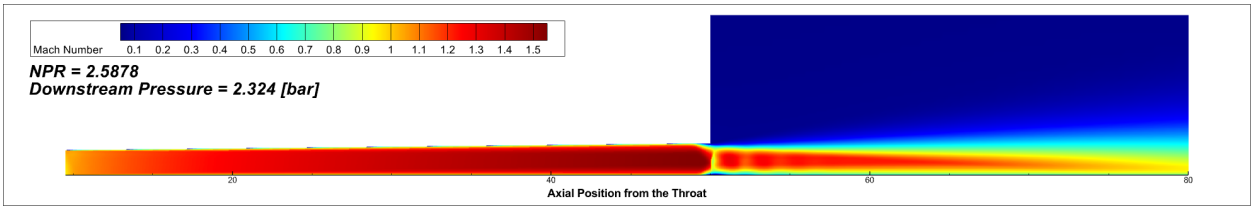
Mach Number 0.1 0.2 0.3 0.4 0.5 0.6 0.7 0.8 0.9 1 1.1 1.2 1.3 1.4 1.5
NPR = 2.5878
Downstream Pressure = 2.324 [bar]
20 40 60 80
Axial Position from the Throat

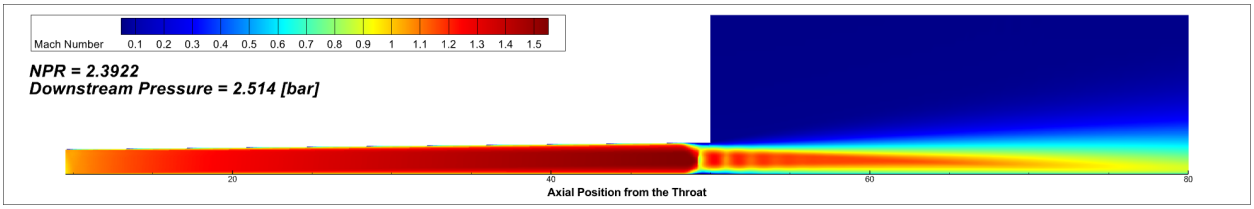
Mach Number 0.1 0.2 0.3 0.4 0.5 0.6 0.7 0.8 0.9 1 1.1 1.2 1.3 1.4 1.5
NPR = 2.3922
Downstream Pressure = 2.514 [bar]
20 40 60 80
Axial Position from the Throat

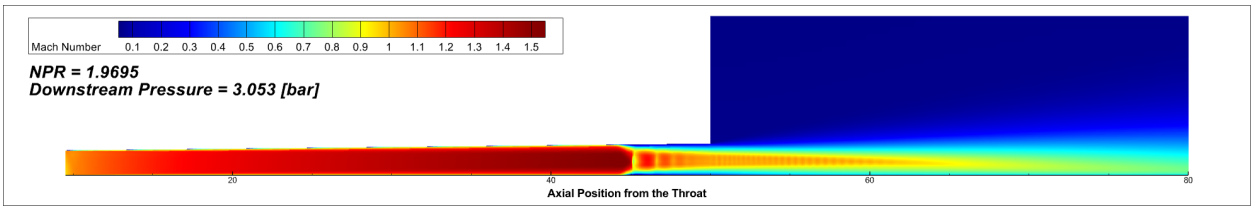
Mach Number 0.1 0.2 0.3 0.4 0.5 0.6 0.7 0.8 0.9 1 1.1 1.2 1.3 1.4 1.5
NPR = 1.9695
Downstream Pressure = 3.053 [bar]
20 40 60 80
Axial Position from the Throat

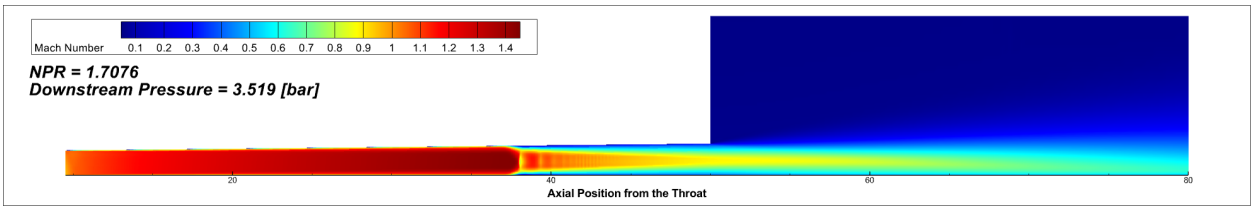
Mach Number 0.1 0.2 0.3 0.4 0.5 0.6 0.7 0.8 0.9 1 1.1 1.2 1.3 1.4
NPR = 1.7076
Downstream Pressure = 3.519 [bar]
20 40 60 80
Axial Position from the Throat

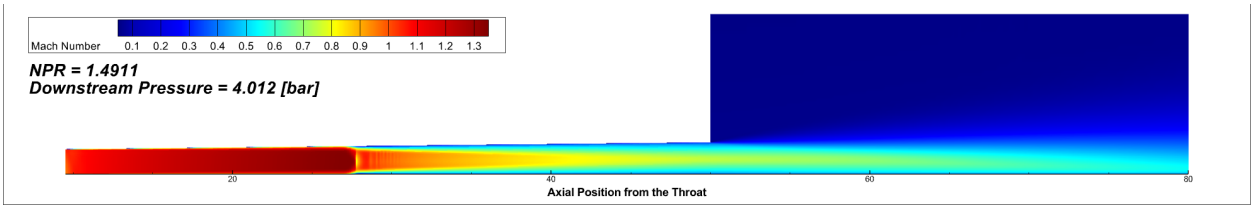
Mach Number 0.1 0.2 0.3 0.4 0.5 0.6 0.7 0.8 0.9 1 1.1 1.2 1.3
NPR = 1.4911
Downstream Pressure = 4.012 [bar]
20 40 60 80
Axial Position from the Throat

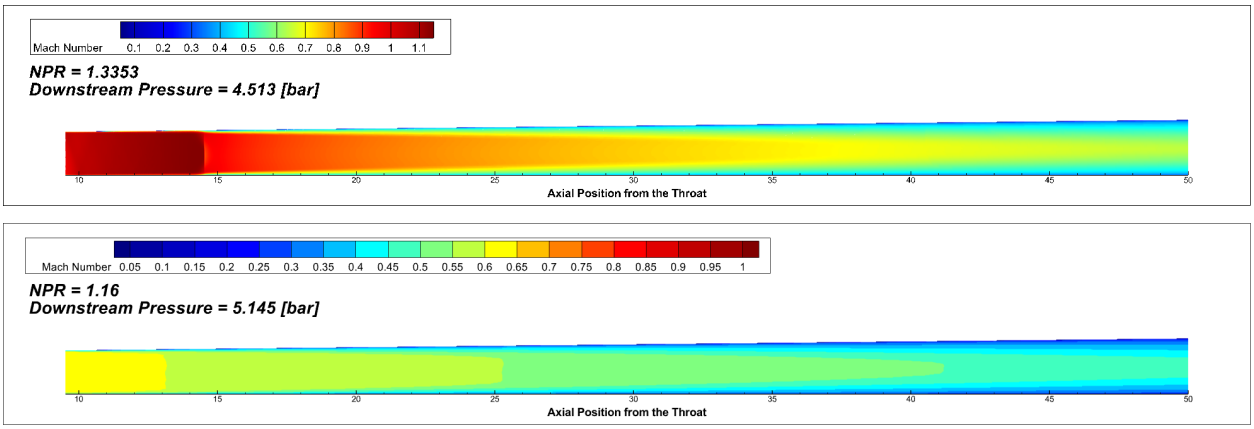

The previous figures illustrate the numerical results of Mach number contours at different Nozzle Pressure Ratio (NPR) values.

At the highest NPR value ($NPR = 4.84988$), the nozzle operates in a nearly adapted regime. However, small expansion waves, characteristic of under-expanded flow, are observed emanating from the nozzle lips.

As the NPR decreases to the range $2.8575 \leq NPR \leq 3.5058$, the flow enters an over-expanded regime, characterized by the presence of an oblique shock and a barrel-shaped plume at the nozzle exit. This oblique shock becomes more pronounced as the downstream pressure increases, resulting in a larger shock angle and greater flow deviation.

At $NPR = 2.8575$, an incipient flow separation at the nozzle exit is observed, which will be demonstrated in more clearly later.

By further decreasing the NPR to 2.5878 and below, the shock structure transitions from a barrel-like configuration to a Mach disk pattern, followed by alternating zones of expansion and compression until the flow structures fully dissipates. This behavior is further clarified in the subsequent figure, which presents the Mach number distribution along the centerline of the divergent section as a function of axial position.

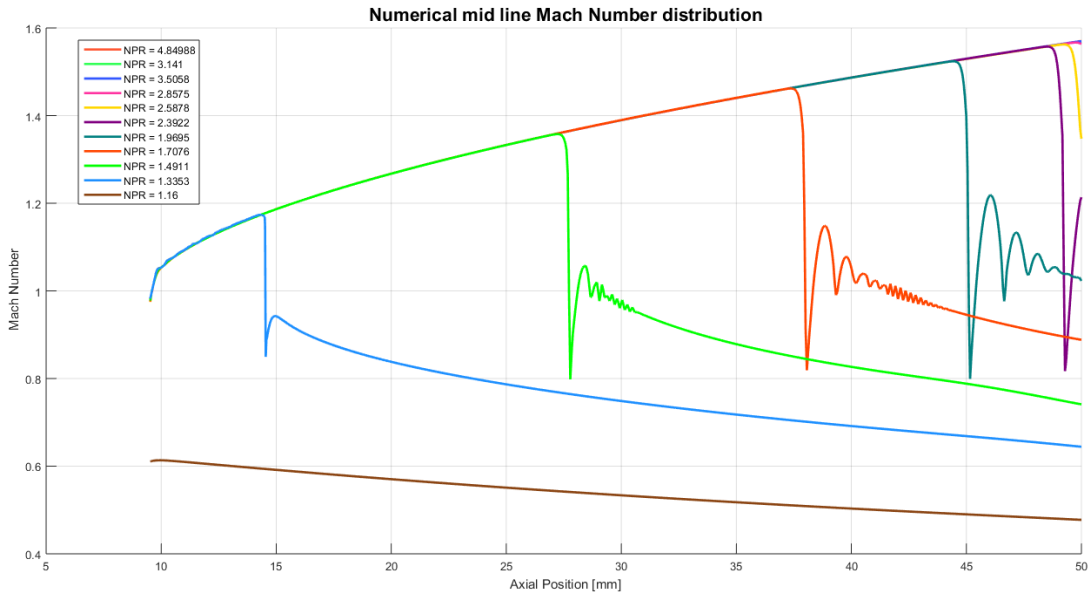

The Mach number distribution clearly reveals the presence of a Mach disk, with the normal shock indicated by a rapid drop to a subsonic Mach value. This is followed by successive zones of expansion and recompression, manifested as "wiggles" in the Mach number profile, continuing until the cycles fully decays. As the NPR decreases (i.e., as the downstream pressure increases), the shock structure shifts upstream toward the throat. Simultaneously, the strength of the normal shock weakens due to the decreasing upstream Mach number associated with this upstream movement. The expansion and recompression zones also become narrower and less distinct.

This last observed flow structure, uncharacteristic of typical conical nozzles [31], reflects the presence and influence of the central probe. The probe encountered a localized shock wave originating from the nozzle wall, which subsequently induced flow separation at its surface. This oblique shock, in conjunction with its reflection, then coalesced into a singular normal shock as the two separation points propagated inward within the nozzle (see the Mach contours).

A final notable transition occurs with the emergence of a single normal shock, followed by a fully subsonic flow, without any indication of boundary layer separation. This solution resembles the ideal one-dimensional nozzle flow with an internal normal shock and represents the final flow field behavior before the nozzle transitions to a completely subsonic regime. These two distinct flow regimes are illustrated for NPR values of 1.3353 and 1.16, respectively.

5.4 Analytical vs Numerical Results

The analytical calculations are more detailed in the Appendix. B.

	NPR=4.84988				
	Ideal Theory	Free Interaction Theory	$k-\omega$	SST $k-\omega$	Spalart-Allmaras
Mass flow rate, [kg/s]	0.033161309	0.033161309	0.032952	0.032949845	0.032923424
Exit Mach Number,	1.74641037	1.74641037	1.490421	1.4665339	1.4458934
Thrust Force, [N]	15.50224546	15.50224546	14.04613	13.886195	13.743144
Specific Impulse, [s]	47.65340513	47.65340513	43.45166	42.95966403	42.55122766
Thrust Coefficient,	1.091914412	1.091914412	0.989352	0.978086465	0.96801054
Normal Shock/ Separation position [mm]	/	/	/	/	/
	NPR=3.5058				
	Ideal Theory	Free Interaction Theory	$k-\omega$	SST $k-\omega$	Spalart-Allmaras
Mass flow rate, [kg/s]	0.033161309	0.033161309	0.032744	0.032744956	0.032720968
Exit Mach Number,	1.74641037	1.74641037	1.466748	1.4484933	1.4335753
Thrust Force, [N]	13.94376417	13.94376417	13.87363	13.756227	13.6545
Specific Impulse, [s]	42.86268365	42.86268365	43.19035	42.82387032	42.53835108
Thrust Coefficient,	0.980998616	0.980998616	0.976551	0.967804639	0.960647745
Normal Shock/ Separation position [mm]	/	/	/	/	/
	NPR=3.141				
	Ideal Theory	Free Interaction Theory	$k-\omega$	SST $k-\omega$	Spalart-Allmaras
Mass flow rate, [kg/s]	0.033161309	0.033161309	0.032738	0.032740056	0.032714983
Exit Mach Number,	1.74641037	1.74641037	1.401483	1.4105584	1.4079975
Thrust Force, [N]	13.29358016	13.29358016	13.38659	13.462382	13.448513
Specific Impulse, [s]	40.86403887	40.86403887	41.68159	41.91538739	41.90429715
Thrust Coefficient,	0.935411102	0.935411102	0.941956	0.94728895	0.946313049
Normal Shock/ Separation position [mm]	/	/	/	/	/

	NPR=2.8575				
	Ideal Theory	Free Interaction Theory	$k-\omega$	SST $k-\omega$	Spalart-Allmaras
Mass flow rate, [kg/s]	0.033161309	0.033161309	0.032661	0.03266417	0.032639702
Exit Mach Number,	1.74641037	1.74641037	1.19764	1.2996195	1.3536873
Thrust Force, [N]	12.67280145	12.67280145	11.88507	12.616983	13.022951
Specific Impulse, [s]	38.95578503	38.95578503	37.09353	39.37448471	40.67187687
Thrust Coefficient,	0.891729619	0.891729619	0.836301	0.887801919	0.916368112
Normal Shock/ Separation position [mm]	/	/	49.0651	49.5601	49.89
	NPR=2.5878				
	Ideal Theory	Free Interaction Theory	$k-\omega$	SST $k-\omega$	Spalart-Allmaras
Mass flow rate, [kg/s]	0.033161309	0.033161309	0.032734	0.032735138	0.032711481
Exit Mach Number,	1.74641037	/	1.113713	0.97455282	1.1539107
Thrust Force, [N]	11.95727231	11.84594	11.2234	10.110337	11.472239
Specific Impulse, [s]	36.75627141	36.41403946	34.95033	31.48345953	35.75024081
Thrust Coefficient,	0.841520867	0.833685596	0.789873	0.711538496	0.807385519
Normal Shock/ Separation position [mm]	/	49.99938	48.2952	48.9001	49.4501
	NPR=2.3922				
	Ideal Theory	Free Interaction Theory	$k-\omega$	SST $k-\omega$	Spalart-Allmaras
Mass flow rate, [kg/s]	0.033161309	0.033161309	0.032703	0.03270655	0.03268233
Exit Mach Number,	1.74641037	/	1.020991	1.0723061	1.0480184
Thrust Force, [N]	11.3364936	11.67956	10.4497	10.870441	10.679996
Specific Impulse, [s]	34.84801758	35.90259268	32.57221	33.88000145	33.31110749
Thrust Coefficient,	0.79783212	0.821976216	0.735422	0.765032584	0.751629574
Normal Shock/ Separation position [mm]	/	44.61201	47.1953	47.7453	48.6802

	NPR=1.9695				
	Ideal Theory	Free Interaction Theory	$k-\omega$	SST $k-\omega$	Spalart-Allmaras
Mass flow rate, [kg/s]	0.033161309	0.033161309	0.032776	0.032778617	0.032755067
Exit Mach Number,	1.74641037	/	0.876439	0.87547674	0.8577259
Thrust Force, [N]	9.575442419	11.41833	9.193076	9.1816741	9.0269263
Specific Impulse, [s]	29.43460275	35.09958004	28.59136	28.55369001	28.09262987
Thrust Coefficient,	0.674006118	0.80372519	0.647092	0.646289147	0.635396599
Shock/ Separation position [mm]	/	29.97199	43.5108	43.4558	44.6657
	NPR=1.7076				
	Ideal Theory	Free Interaction Theory	$k-\omega$	SST $k-\omega$	Spalart-Allmaras
Mass flow rate, [kg/s]	0.033161309	0.033161309	0.032856	0.032859198	0.032835585
Exit Mach Number,	1.74641037	/	0.735403	0.73223307	0.72242456
Thrust Force, [N]	8.052900966	11.23427	7.886805	7.8562709	7.7662108
Specific Impulse, [s]	24.75435918	34.53378551	24.46911	24.37196152	24.1099
Thrust Coefficient,	0.567213224	0.791295774	0.555514	0.553363411	0.547019948
Normal Shock/ Separation position [mm]	/	21.35112	37.5165	36.8016	37.6815
	NPR=1.4911				
	Ideal Theory	Free Interaction Theory	$k-\omega$	SST $k-\omega$	Spalart-Allmaras
Mass flow rate, [kg/s]	0.033161309	0.033161309	0.032736	0.032738658	0.032718395
Exit Mach Number,	0.6028	/	0.624279	0.62575966	0.61937631
Thrust Force, [N]	6.70138	/	6.817746	6.8300829	6.767862
Specific Impulse, [s]	20.59983	/	21.22975	21.26650362	21.08582006
Thrust Coefficient,	0.47178	/	0.479974	0.480842887	0.47646249
Normal Shock/ Separation position [mm]	44.98953	/	28.3877	27.0678	27.6178

	NPR=1.3353				
	Ideal Theory	Free Interaction Theory	$k-\omega$	SST $k-\omega$	Spalart-Allmaras
Mass flow rate, [kg/s]	0.033161309	0.033161309	0.032681	0.032671648	0.032647437
Exit Mach Number,	0.54328	/	0.55413	0.55541512	0.5530979
Thrust Force, [N]	6.07841	/	6.113748	6.12363	6.0967155
Specific Impulse, [s]	18.68485	/	19.06944	19.10596128	19.03609351
Thrust Coefficient,	0.42785	/	0.430341	0.431036385	0.429141899
Normal Shock/ Separation position [mm]	31.91716	/	16.7841	15.0793	14.5294
	NPR=1.16				
	Ideal Theory	Free Interaction Theory	$k-\omega$	SST $k-\omega$	Spalart-Allmaras
Mass flow rate, [kg/s]	0.033112835	0.033112835	0.028069	0.027957096	0.027778918
Exit Mach Number,	0.477748171	0.477748171	0.422785	0.42216934	0.41751623
Thrust Force, [N]	4.598914811	4.598914811	4.064636	4.0421284	3.9744073
Specific Impulse, [s]	14.15761152	14.15761152	14.76116	14.73835591	14.58438226
Thrust Coefficient,	0.323605524	0.323605524	0.286011	0.284426899	0.279661661
Normal Shock/ Separation position [mm]	/	/	/	/	/

These tables show typical nozzle parameters based on both ideal 1D and FIT theories, along with numerical results from the different turbulence models. They serve as a comparative reference between analytical predictions and CFD-based approaches while simultaneously providing benchmark values for subsequent graphical representations.

5.4.1 Nozzle Wall Pressure Distribution

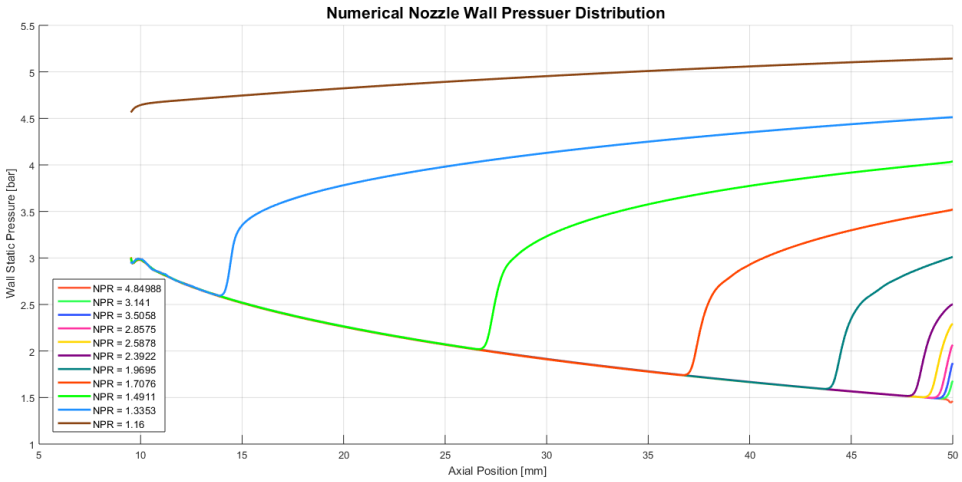

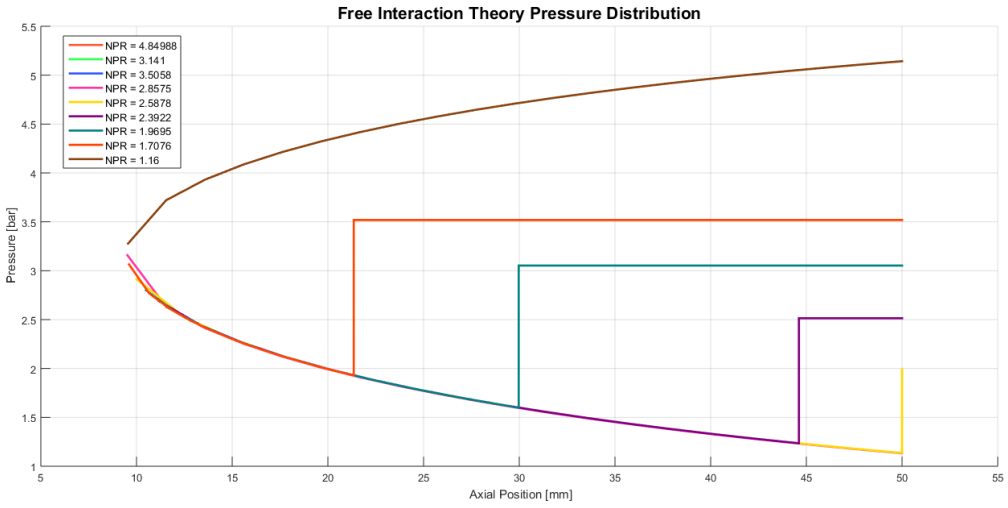

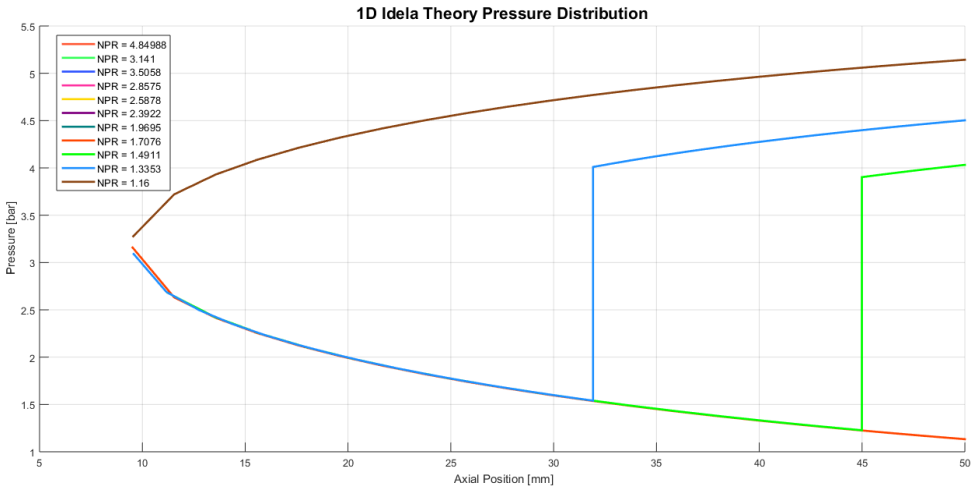

In the first figure, which illustrates the numerical wall pressure distribution, the characteristic pressure profile of an over-expanded conical nozzle is clearly identified, consistent with the discussion in Chapter 2. A well-defined pressure plateau appears downstream of the separation point, indicating the expected flow behavior [20].

Furthermore, a qualitative comparison between the analytical and numerical wall pressure distributions reveals notable differences. The Chapman free interaction theory provides more accurate pressure profiles than the ideal one-dimensional theory; however, it does not precisely predict the exact location of the separation point [7], [13]. This limitation will be further examined in the subsequent discussion. Nevertheless, the overall shape of the pressure distribution remains consistent and serves as a reasonable approximation.

5.5 Shock/ Separation Behavior and Position

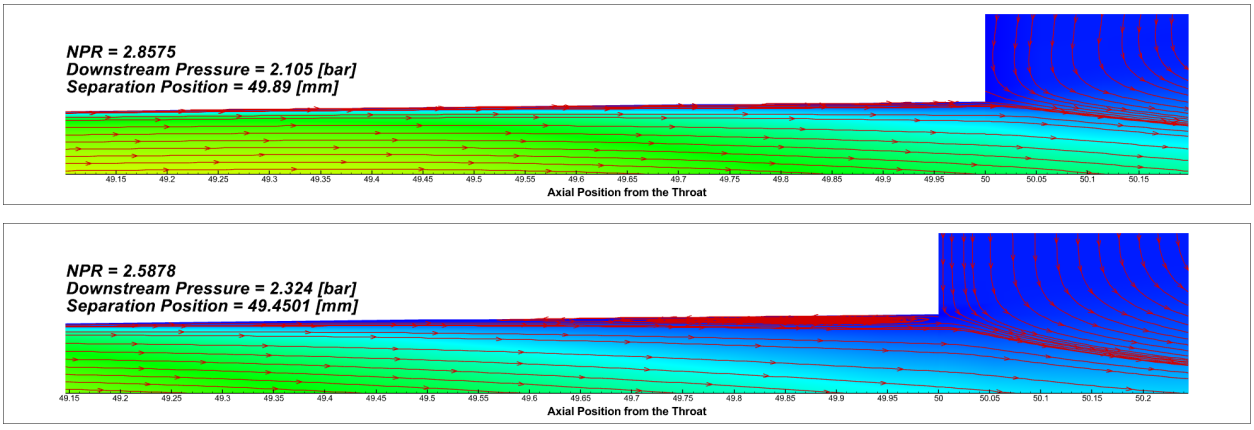

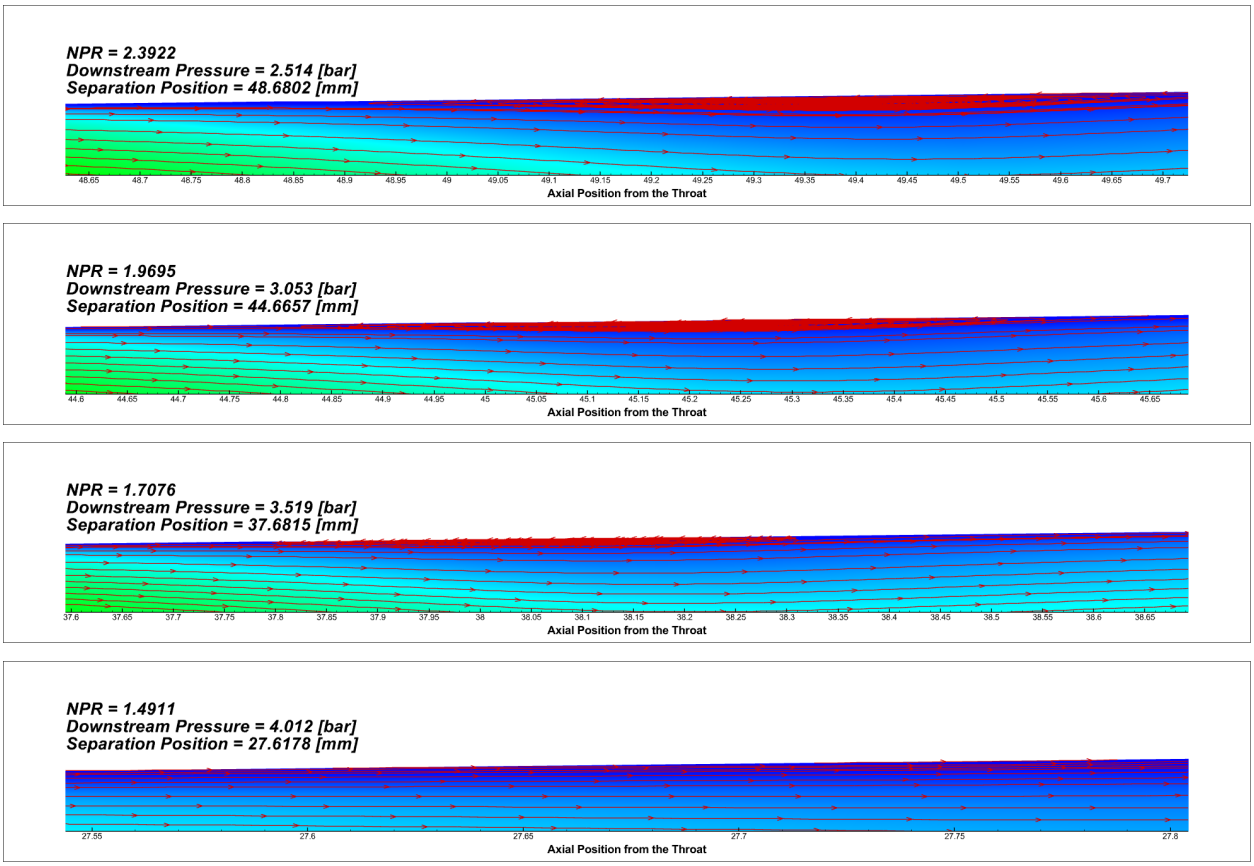

As illustrated in the above figures, the separation point is clearly marked by a recirculating flow bubble forming along the nozzle wall. However, an unexpected behavior emerges: the flow does not remain fully separated, as typically observed in a Free Shock Separation (FSS) regime. Instead, it reattaches shortly after separation, confining the separated region to a small recirculating bubble. This characteristic behavior persists across nearly all Nozzle Pressure Ratios (NPRs). The size of the separated region progressively decreases with increasing NPR, becoming virtually absent at higher values. The only case exhibiting a near-FSS-like separation occurs at an NPR of 2.5878, where the separation region shifts closer to the nozzle exit. At the next higher NPR, only incipient separation is observed at the nozzle lips.

These trends are further supported by the wall shear stress distributions presented in the subsequent figures.

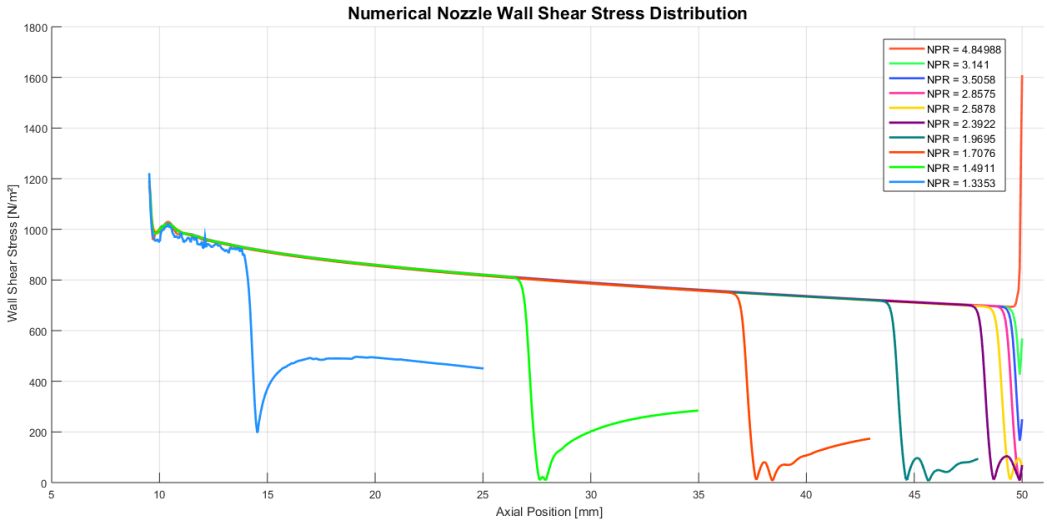

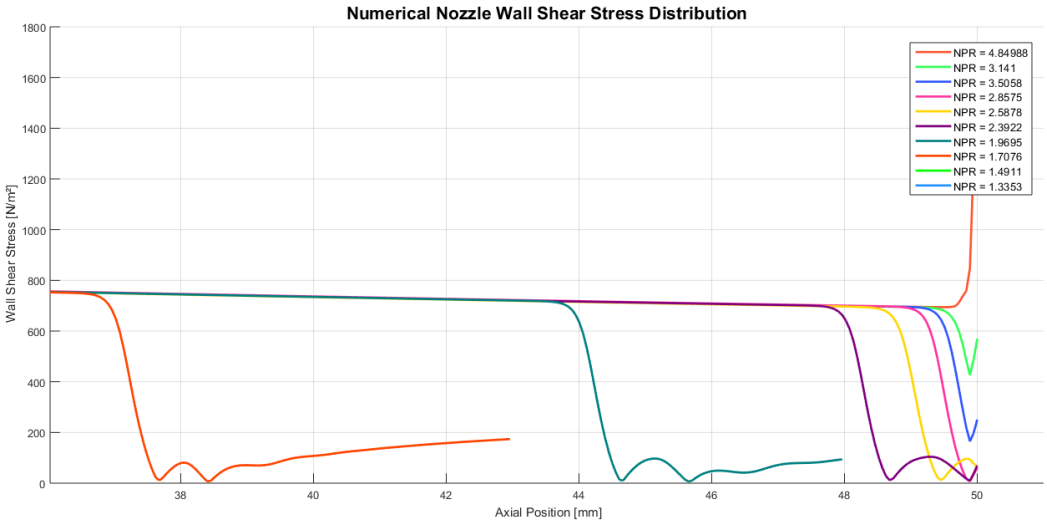

Examining the numerical shear stress distribution along the nozzle wall reveals the separation point as an initial drop in shear stress, approaching nearly zero. For cases with a higher degree of over-expansion, this is followed by a distinct "ballistic" evolution of shear stress within the separated region, culminating in a second minimum that marks the reattachment point.

Both the height of the apogee (the peak within the "ballistic" curve) and the distance between the separation and reattachment points progressively decrease as the NPR increases. Eventually, at an NPR of 1.4911, the shear stress profile appears nearly flat, indicating a very thin and almost negligible separated region.

The final NPR value of 1.3353 corresponds to the case of a normal shock without separation, as previously described and confirmed here through the shear stress analysis.

5.5.1 Shock/ Separation position comparison

The following figures illustrate the separation and normal shock positions obtained from the numerical solutions (black points), the separation point predicted by Chapman's Free Interaction Theory (FIT) (red line), and the normal shock position estimated using one-dimensional theory (green line) at various NPR values.

As previously noted, the Free Interaction Theory is typically applicable to configurations exhibiting Free Shock Separation (FSS). However, since reattachment occurs shortly after separation in our numerical results, it is difficult to draw definitive conclusions about the theory's accuracy in predicting separation points across all cases. Nevertheless, the theory provides a good approximation in the single case that closely resembles FSS, corresponding to an NPR value of 2.5878 where the numerical separation point aligns most closely with the FIT prediction.

Another noteworthy point regarding FIT's accuracy is its prediction of incipient separation at the nozzle lips starting from an NPR of approximately 3 (corresponding to a downstream pressure of 1.99714 bar). This prediction is consistent with our current numerical findings.

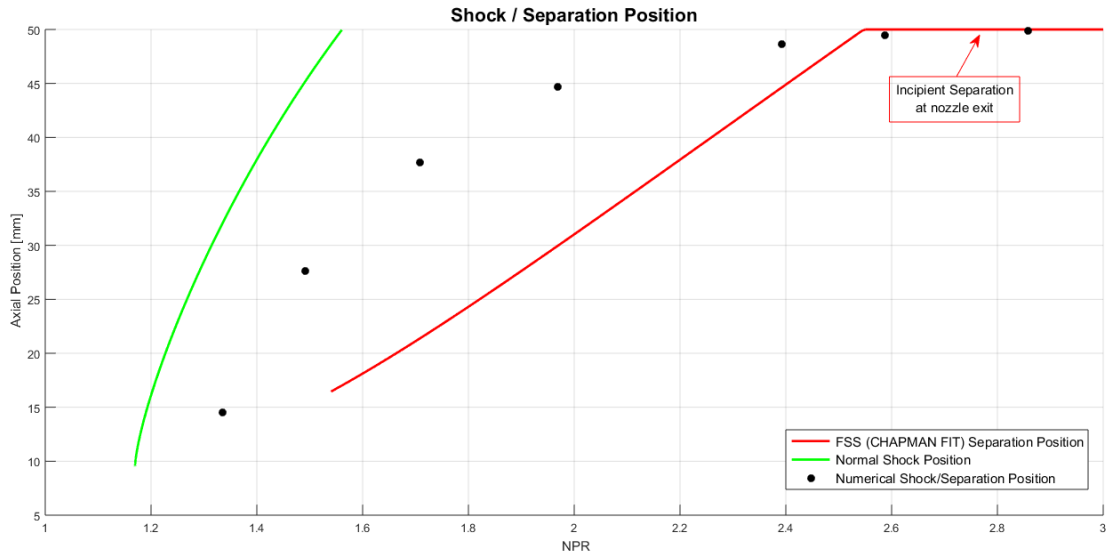

5.6 Mass Flow Rate and Exit Mach Number Comparison

The following figure compares the mass flow rates obtained from the analytical one-dimensional theory, the numerical solution, and the experimental orifice measurements across different NPR values.

It is important to note that the experimental mass flow rate does not represent the exact mass flow rate through the nozzle itself. Instead, it reflects the mass flow rate measured further downstream at the machine's exit orifice. Its primary purpose here is to illustrate the concept of a choked nozzle and to capture the general flow behavior, as evidenced by the observed mass flow trends. Compared to the analytical predictions, the numerical results show excellent agreement in the supersonic regime, with the only notable deviation occurring in the final case corresponding to subsonic nozzle flow.

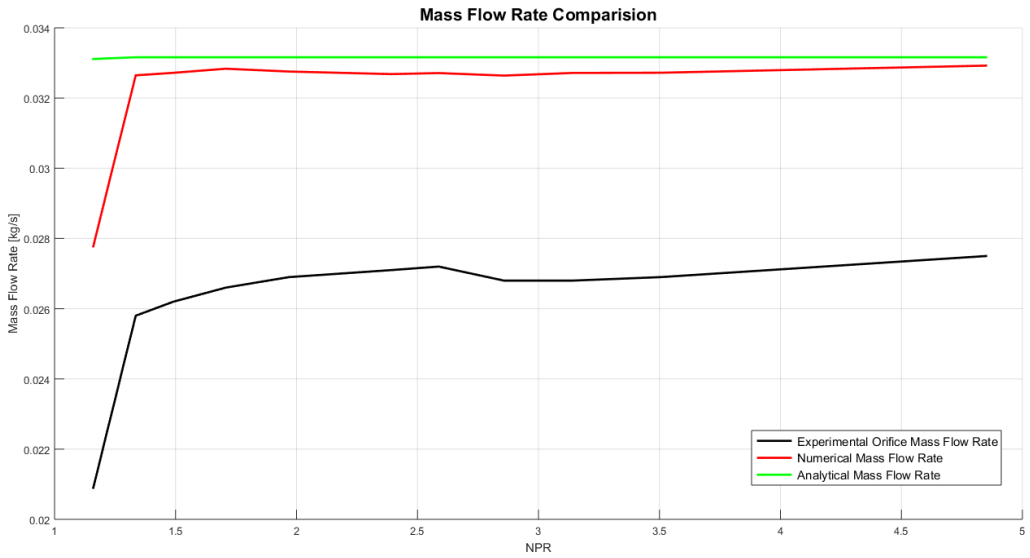

For the exit Mach number, an entirely opposite behavior is observed between the numerical results and the one-dimensional theory. Throughout most of the supersonic regime, a significant offset error is evident except for the cases corresponding to NPR values that result in a one-dimensional normal shock solution and subsonic nozzle flow.

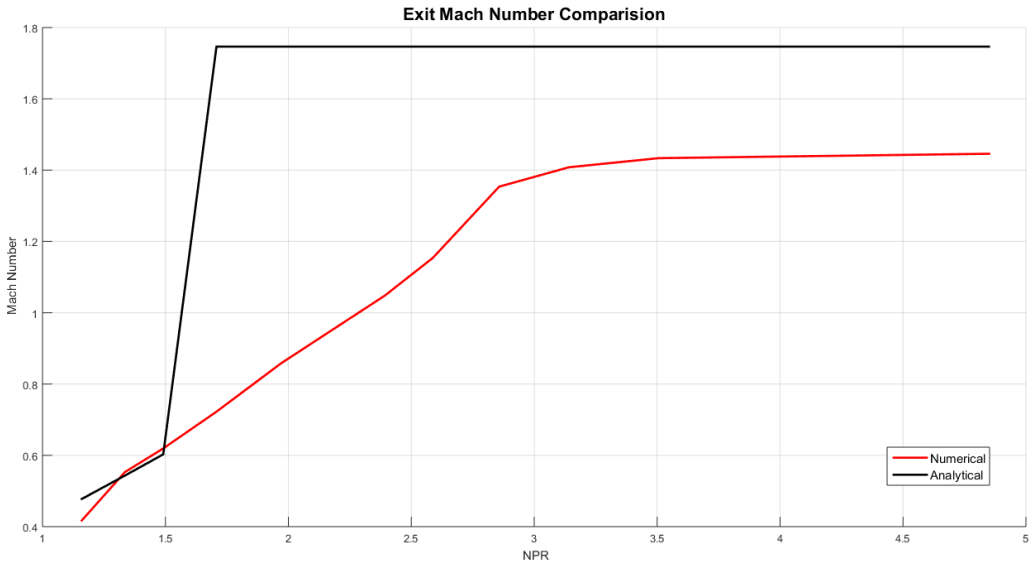

5.7 Nozzle Performance Comparison

As the following results demonstrate, the theoretical performance estimates align remarkably well with the numerical results. This agreement is particularly significant, as engineers in most nozzle design frameworks are primarily concerned with these final performance metrics. Consequently, this simplified theoretical approach, which provides reasonably accurate performance predictions, serves as a powerful tool for initial design and approximate estimations.

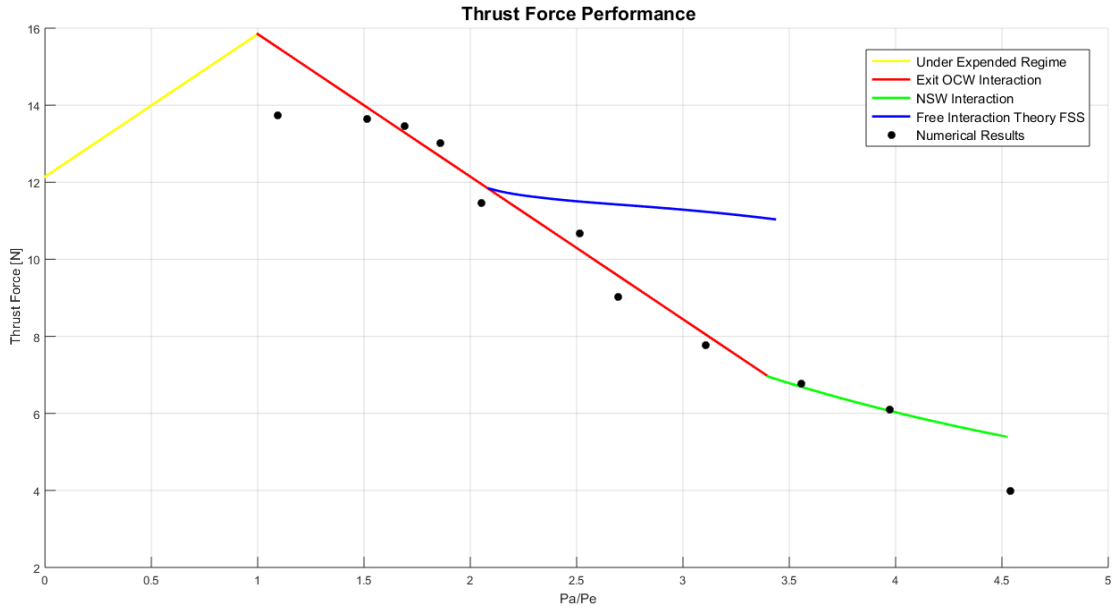

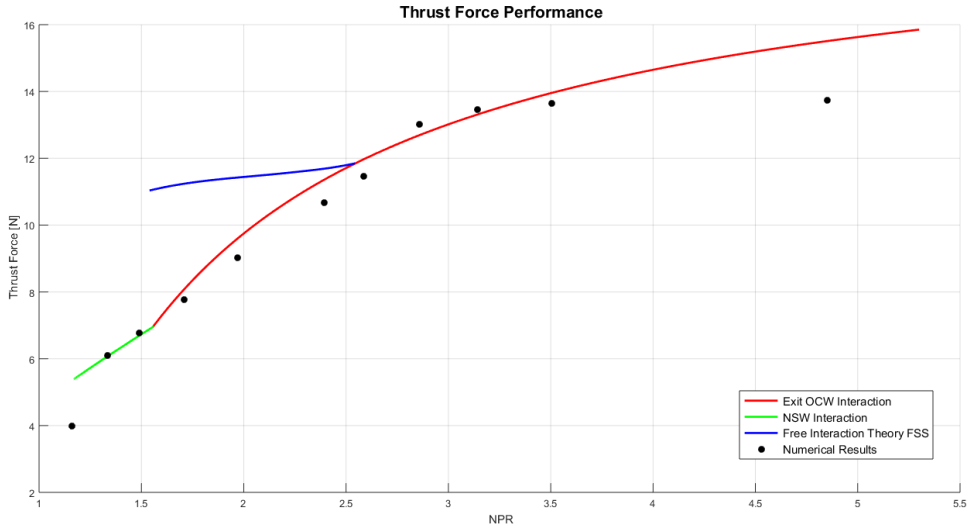
Thrust Force Performance
Thrust Force [N]
NPR
Exit OCW Interaction
NSW Interaction
Free Interaction Theory FSS
Numerical Results

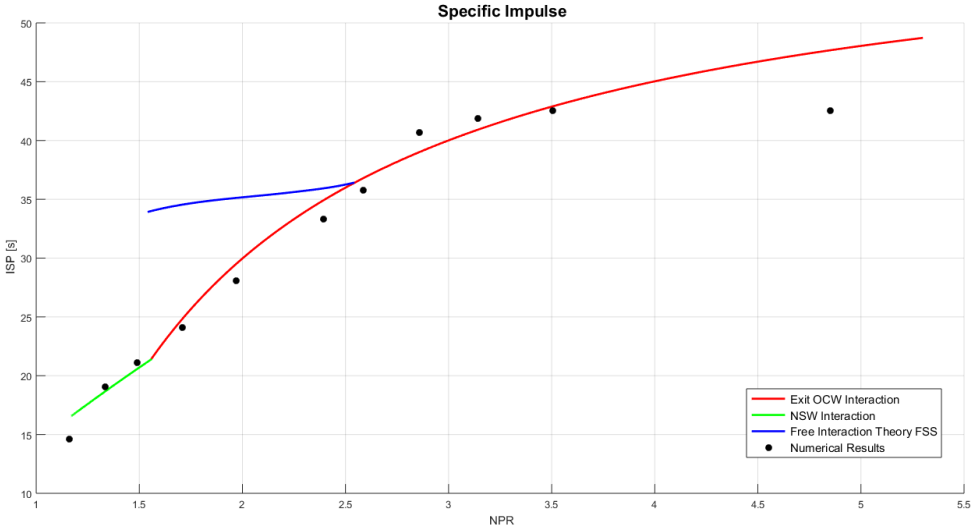
Specific Impulse
ISP [s]
NPR
Exit OCW Interaction
NSW Interaction
Free Interaction Theory FSS
Numerical Results

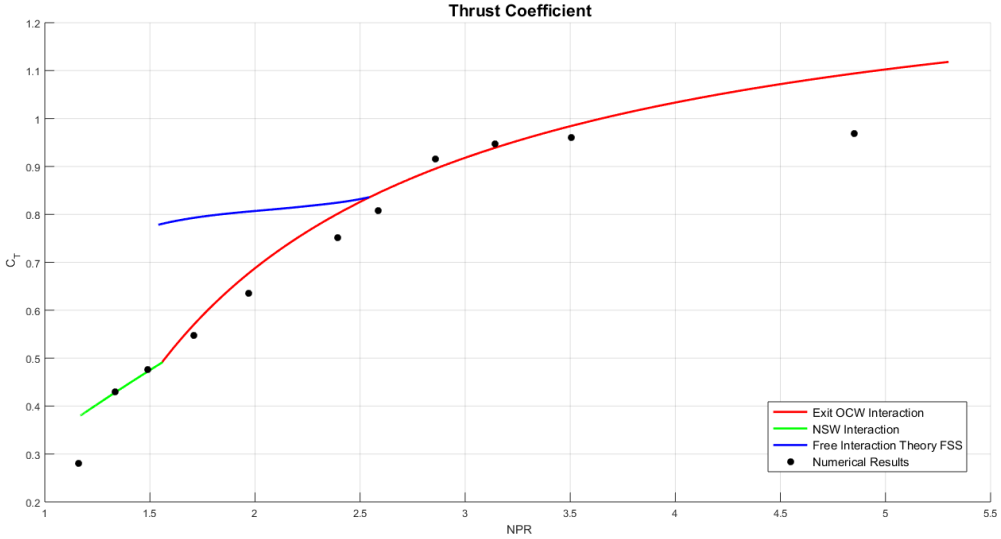
Thrust Coefficient
C_T
NPR
Exit OCW Interaction
NSW Interaction
Free Interaction Theory FSS
Numerical Results

CONCLUSION

The over-expanded operation of a nozzle is primarily governed by Shock Wave–Boundary Layer Interaction (SWBLI), a complex phenomenon involving the interplay between the internal flow field, separated regions, and the exhaust plume. Experimental observations reveal distinct separation configurations—most notably Free Shock Separation (FSS) and Restricted Shock Separation (RSS)—both of which contribute to performance losses and the generation of side loads due to unsteady and asymmetric flow behavior. Additionally, conventional nozzle operations exhibit various exhaust flow structures, such as barrel shocks, Mach disks, and cap shocks.

This study confirms that numerical modeling of these interactions, complemented by simplified analytical and empirical approaches, demonstrates strong agreement with experimental results. This alignment underscores the reliability and accuracy of the developed models in simulating, approximating, and understanding the complex flow behaviors within over-expanded nozzle regimes.

The limited exit-to-throat area ratio of the experimental conical nozzle has led to a relatively small separation bubble [31]. This finding contrasts with the foundational assumptions of Chapman's Free Interaction Theory, which anticipates an FSS-type separation. As a result, a definitive steady-state validation of this model could not be achieved within the constraints of the current experimental configuration. To refine this theoretical assessment, future investigations using alternative nozzle geometries—particularly those that clearly exhibit FSS behavior—are recommended.

Based on the results obtained from this study. The Spalart-Allmaras model delivers enhanced accuracy in predicting shock-wave boundary layer interactions involving mild separation [rodriguez][Ansys].

While the nozzle's original configuration was conical, the presence of the cylindrical probe proved to be non-negligible. This observation reinforces the general preference against intrusive experimental methods in supersonic regimes, given their significant impact on the flow characteristics.

To further advance nozzle flow understanding and design methodologies, it is crucial to rigorously assess and enhance current separation criteria. Moreover, there is a compelling need to innovate

and develop new criteria applicable to advanced nozzle architectures, including those introduced in Chapter 1.

Another important aspect that remains beyond the scope of this study is the inherently unsteady nature of flow separation and the associated turbulence modeling challenges. A more detailed exploration of unsteady interactions and three-dimensional effects would require the implementation of advanced computational approaches, such as Large Eddy Simulation (LES), Detached Eddy Simulation (DES), or Reynolds Stress Transport (RST)-based models.

The scope of this work was limited to the experimental, numerical, and analytical investigation of mean flow properties associated with flow separation in conical over-expanded nozzles. A comprehensive comparison and analysis of the results have been presented. This was preceded by an extensive state-of-the-art review and bibliographical survey of flow separation in over-expanded nozzles, serving as a thorough introduction to the topic.

APPENDIX A. SHOCK / EXPANSION WAVES RELATIONS

Normal Shock Wave Relations

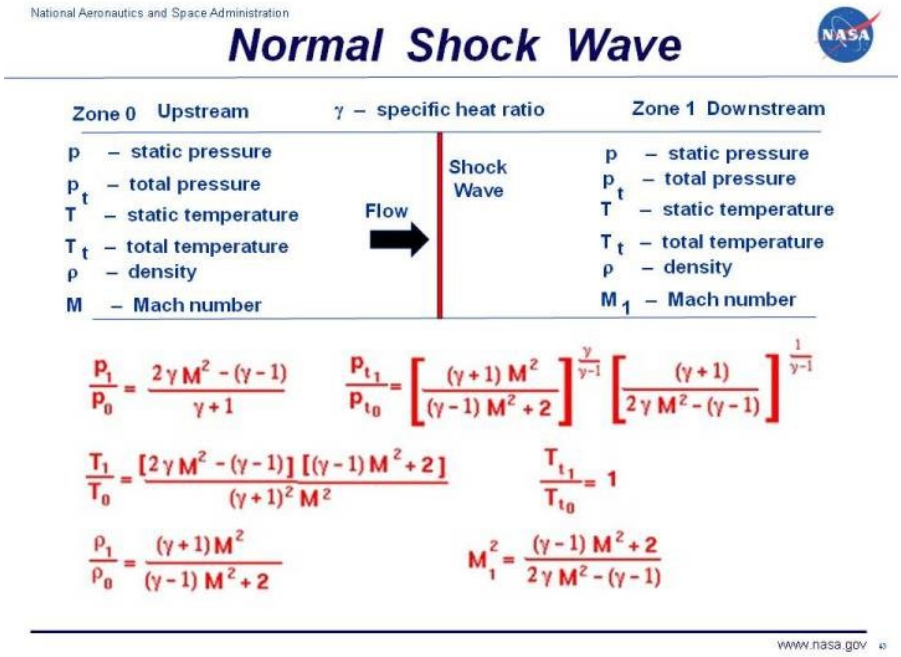

$$\frac{p_1}{p_0} = \frac{2\gamma M^2 - (\gamma - 1)}{\gamma + 1} \qquad \frac{p_{t_1}}{p_{t_0}} = \left[\frac{(\gamma+1)M^2}{(\gamma-1)M^2+2}\right]^{\frac{\gamma}{\gamma-1}} \left[\frac{(\gamma+1)}{2\gamma M^2-(\gamma-1)}\right]^{\frac{1}{\gamma-1}}$$

$$\frac{T_1}{T_0} = \frac{[2\gamma M^2 - (\gamma-1)][(\gamma-1)M^2+2]}{(\gamma+1)^2 M^2} \qquad \frac{T_{t_1}}{T_{t_0}} = 1$$

$$\frac{\rho_1}{\rho_0} = \frac{(\gamma+1)M^2}{(\gamma-1)M^2+2} \qquad M_1^2 = \frac{(\gamma-1)M^2+2}{2\gamma M^2-(\gamma-1)}$$

Oblique shock relations

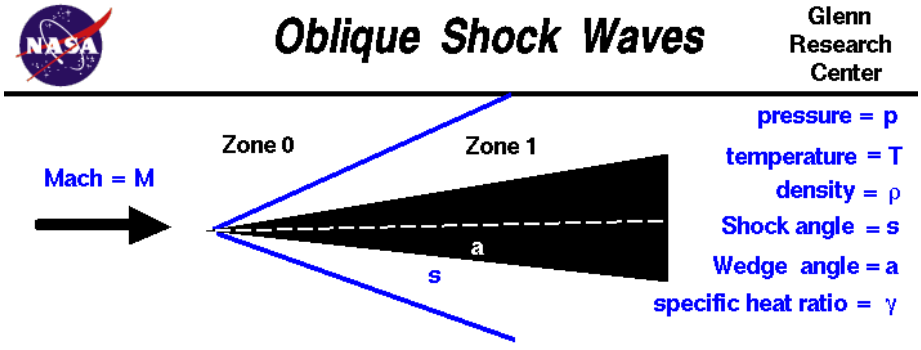

$$\cot a = \tan s \left[\frac{(\gamma+1)M^2}{2(M^2\sin^2 s - 1)} - 1\right] \qquad M_1^2 \sin^2(s-a) = \frac{(\gamma-1)M^2\sin^2 s + 2}{2\gamma M^2 \sin^2 s - (\gamma-1)}$$

$$\frac{T_1}{T_0} = \frac{[2\gamma M^2\sin^2 s - (\gamma-1)][(\gamma-1)M^2\sin^2 s + 2]}{(\gamma+1)^2 M^2 \sin^2 s} \qquad \frac{p_1}{p_0} = \frac{2\gamma M^2\sin^2 s - (\gamma-1)}{(\gamma+1)}$$

$$\frac{p_{t_1}}{p_{t_0}} = \left[\frac{(\gamma+1)M^2\sin^2 s}{(\gamma-1)M^2\sin^2 s + 2}\right]^{\frac{\gamma}{\gamma-1}} \left[\frac{(\gamma+1)}{2\gamma M^2\sin^2 s - (\gamma-1)}\right]^{\frac{1}{\gamma-1}} \qquad \frac{\rho_1}{\rho_0} = \frac{(\gamma+1)M^2\sin^2 s}{(\gamma-1)M^2\sin^2 s + 2}$$

Expansion waves

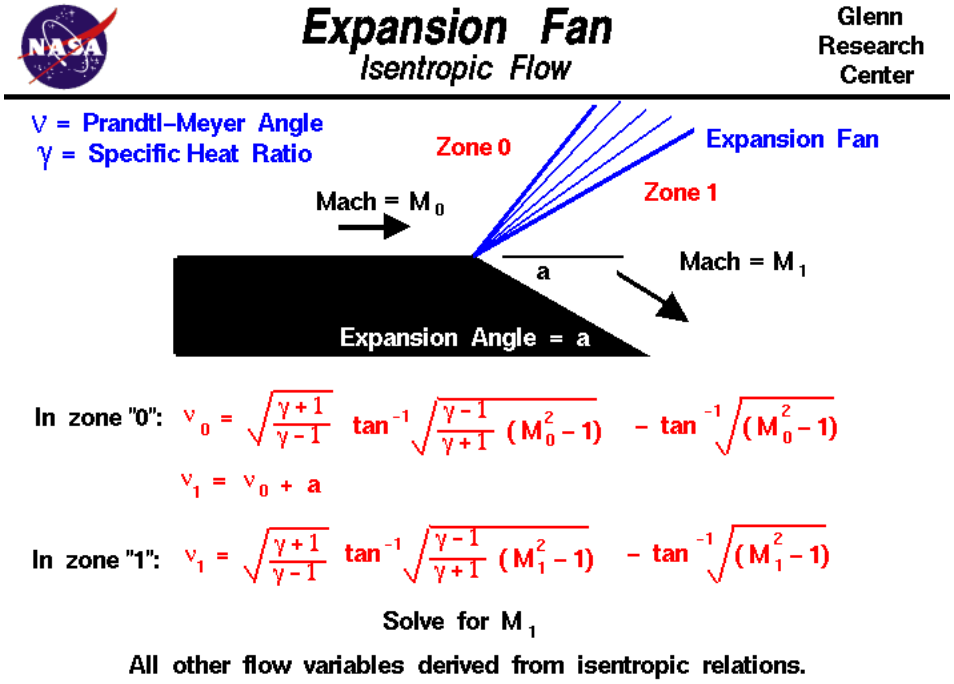

APPENDIX B. THEORICAL STUDY OF THE EXPERIMENTAL CONICAL NOZZLE

Geometrical Characteristics

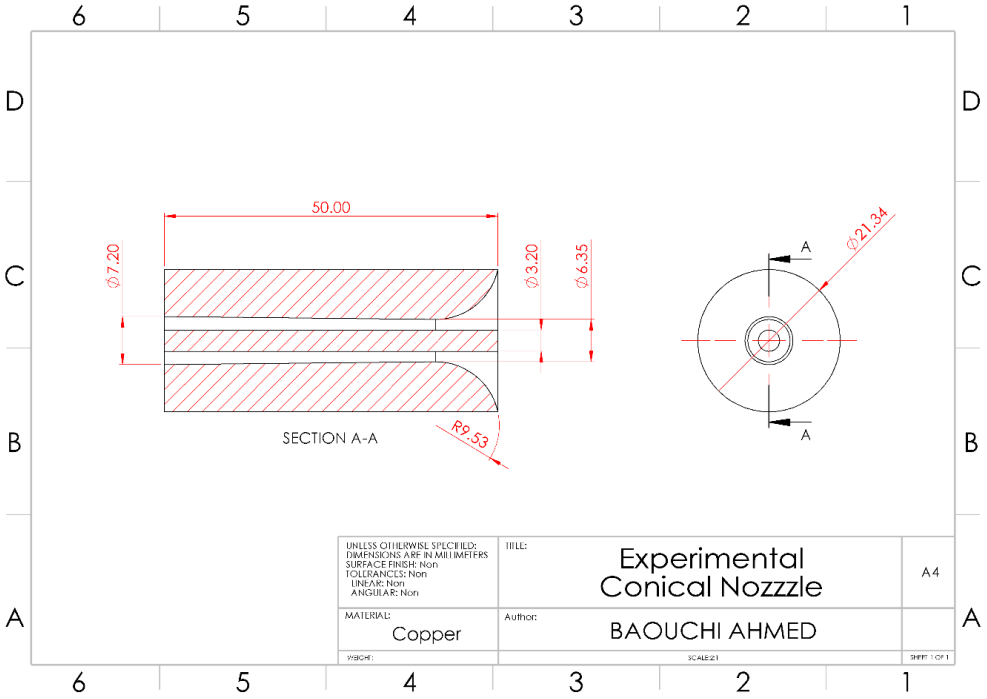

Figure B.1 : Technical drawing of the experimental conical nozzle with the cylindrical probe.

Table B.1 : Nozzle geometrical characteristics.

Inlet Section Area	$498.665\ mm^2$
Throat Section Area	$23.62674025\ mm^2$
Exit Section Area	$32.6725636\ mm^2$
Divergent half Angle	$0.6016°$

- Expression for nozzle section area variation with position

The reference position for length is the nozzle inlet section, all length and area dimensions are based on mm.

Convergent Part,

$$y = \sqrt{19.05x - x^2}$$
$$r = 12.7 - y \qquad \text{(B-1)}$$
$$Section\ Area = \pi \cdot (r^2 - 1.6^2)$$

Divergent Part,

$$r = \frac{7.2 - 6.35}{2 \cdot 40.475}\,(x - 9.525) + 3.175$$
$$Section\ Area = \pi \cdot (r^2 - 1.6^2) \tag{B-2}$$

Intrinsic Nozzle Characteristics

Operating Conditions	
Total Pressure, P_0	6.0 $[bar]$
Total Temperature, T_0	300.0 $[K]$
Mass flow rate, ($\dot{m}$, Eq. (1-21))	0.03316130879 $[kg/s]$

Throat Conditions (relations Table 1.2)	
Temperature, T^*	249.9 $[K]$
Pressure, P^*	3.16968 $[bar]$
Density, ρ^*	4.417177 $[kg/m^3]$
Velocity, U^*	316.9754 $[m/s]$

Exit Conditions (relations Table 1.1)	
Exit Area ratio, A_e/A^*	1.382864
Exit Mach Number, M_e	1.74641
Exit Temperature, T_e	186.3366 $[K]$
Exit Pressure, P_e	1.133105 $[bar]$
Exit Velocity, V_e	477.9133 $[m/s]$
Critical Exit Pressure, P_e^{sonic}	5.129 $[bar]$

Adapted Regime Performance	
Thrust Force, (F_{ad}, Eq. (1-27))	15.84823051 $[N]$
Specific Impulse, (Isp, Eq. (1-29))	48.716952 $[s]$
Thrust Coefficient, (C_T, Eq. (1-32))	1.117958603

All flow field variables follow the isentropic solution across the nozzle, the relations are described in Table 1.1.

Models Comparison

Type of Analysis	1D (Ideal) Theory	Inviscid (Euler) 2D	Viscous Full Solution
Mass flow rate, [kg/s]	0.03316130879	0.033043253	0.032731018
Exit Mach Number, M_e	1.74641034	1.7468278	1.4855325
Thrust Force, [N]	15.84823051	15.79511	14.016029
Specific Impulse, [s]	48.7169517	48.727131	43.651229
Thrust Coefficient, C_T	1.117958603	1.1142114	0.9887123

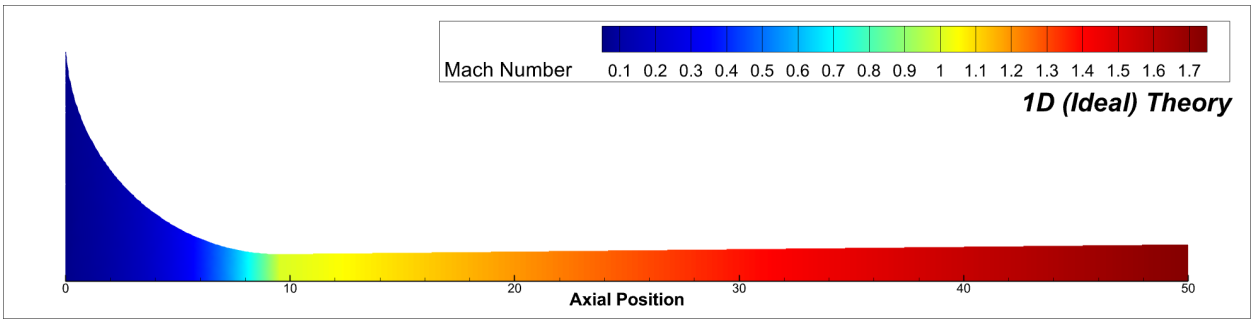

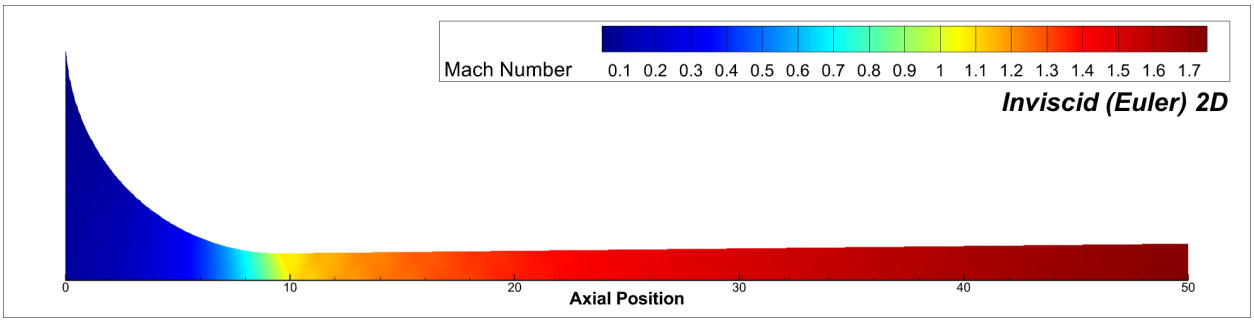

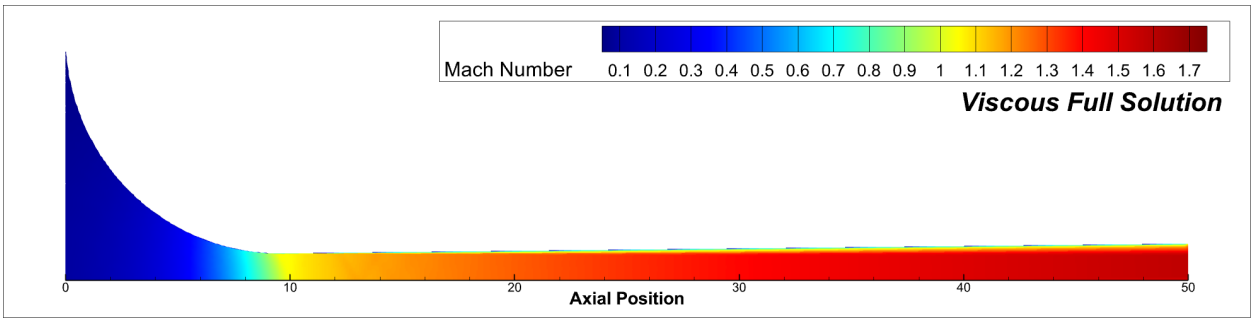

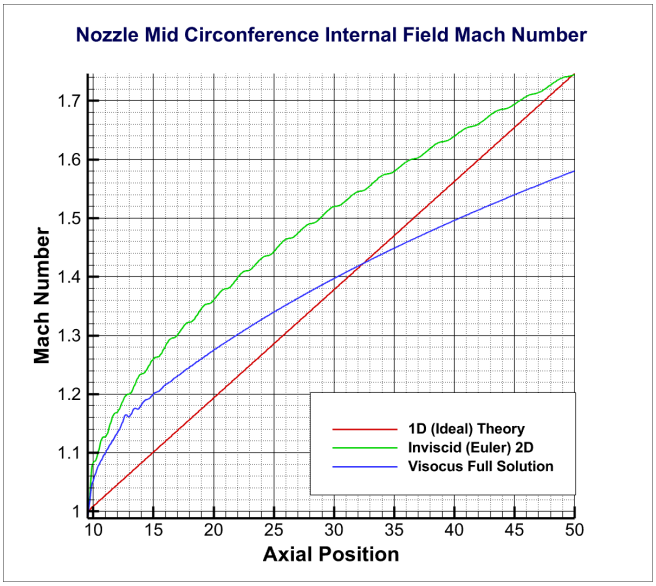

Under-Expanded Calculations

All flow field variations are identical to the adapted regime, unless for performance calculation where losses of flow stream divergence from axial direction at nozzle lips occur. Which are due to the higher outlet pressure P_e of the flow compared to ambient operating pressure.

So, losses can be well estimated by a small rearrangement of the thrust equation as follows,

$$F = \dot{m}\, V_e + (P_a - P_e)\, A_e \qquad \text{(B-3)}$$

All other equations remain the same. The reported analytical calculation is given at the end.

Over-Expanded Calculations

In this part, we will focus on two studies, one of purely 1D (ideal) theory and the other using the free interaction theory.

Ideal Theory analysis

In this theory, the overexpansion is divided into two cases, the first and simpler one, is the case with exit interaction where a match between exit and ambient pressure is reached by a system of oblique shock waves emanating from nozzle lips. And a second case, where there is a formation of a strong normal shock wave inside the nozzle, this will lead to a jump in the evolution of flow parameters along the nozzle. Let's start getting into the application.

Exit oblique shock waves Interaction

In this regime, the nozzle interior is not influenced by these exit interactions but, as earlier, nozzle performance gets triggered. Especially, the thrust force where the high ambient pressure acts against the exit jet, this effect is established using the conventional thrust equation given by Eq. (1-26), repeated here

$$F = \dot{m}_p \, V_e + (P_e - P_a) \cdot A_e \tag{B-4}$$

All other equations remain the same. The reported analytical calculation is given at the end.

Normal shock wave interaction

Returning to Figure 1.8, we said that, if the pressure is reduced below P_a^{sonic} the nozzle becomes "chocked;" i.e., the flow remains sonic at the throat, and the mass flow rate becomes a fixed value, no matter how P_a is reduced bellow P_a^{sonic}. The match in pressure, in the first case, is reached through a normal shock wave standing at position X_{shock} in the divergent portion of the nozzle. The location of the shock is such that, static-pressure-increase across the shock wave, plus the further static pressure increase downstream the shock results precisely in ambient pressure P_a at the exit.

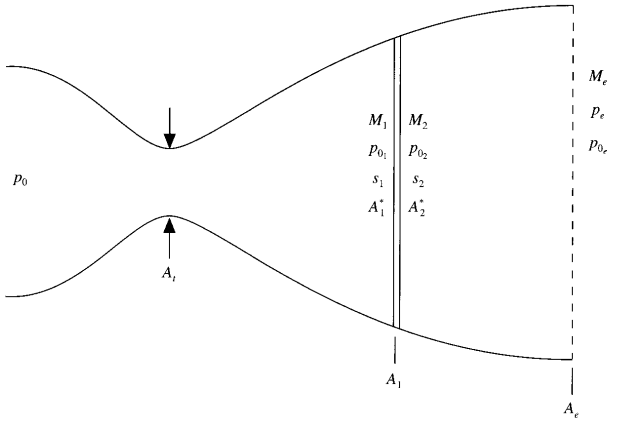

Consider the nomenclature shown above. The normal shock wave is located at area A_1. Conditions immediately upstream of the shock are denoted with a subscript 1, and those immediately downstream of the shock are denoted with subscript 2. The flow from the reservoir, where the pressure is P_0, to station 1 is isentropic (with constant entropy s_1). Hence, the total pressure is constant in this flow; that is, $P_{01} = P_0$. The total pressure decreases across the shock (due to the

entropy increase across the shock). The flow in station 2 downstream of the shock to the nozzle exit is also isentropic (with constant entropy s_2, where $s_2 > s_1$). Hence the total pressure is constant in this portion of the flow, with $(P_0)_e = P_{02}$. Keep in mind that $P_{01} > P_{02}$. For the flow in front of the shock, A_1^* is a constant value, equal to the area of the sonic throat, $A_1^* = A_t$. However, due to the entropy increase across the shock, the value of A^* in the subsonic flow downstream of the shock, denoted A_2^*, takes on the role of the reference value. Indeed, $A_2^* > A_1^*$.

Calculations methodology

For the case where the normal shock wave is standing at the exit plane of the nozzle, the internal flow field is identical to a full-flowing nozzle such that exit conditions are supposed to be the limiting conditions to the shock front. Normal shock jump relations given at Appendix A are used to get flow condition after the shock. The ambient pressure denoted P_a^{sup} which operates after the shock presents the upper limit for this regime. While for every $P_a^{sonic} \leq P_a \leq P_a^{sup}$ the calculations proceed as follows:

Using the equation for mass flow rate (Eq. (1-21)), and noting that the mass flow rate as well as total temperature are conserved across the shock. Then we can write, from the two sides of the shock, that,

$$\frac{\dot{m}}{A_1^*} = \sqrt{\frac{\gamma}{R}} \cdot \frac{P_{01}}{\sqrt{T_0}} \cdot \left(\frac{2}{\gamma+1}\right)^{\frac{\gamma+1}{2(\gamma-1)}}$$

$$\frac{\dot{m}}{A_2^*} = \sqrt{\frac{\gamma}{R}} \cdot \frac{P_{02}}{\sqrt{T_0}} \cdot \left(\frac{2}{\gamma+1}\right)^{\frac{\gamma+1}{2(\gamma-1)}}$$

Thus,

$$P_{01}A_1^* = P_{02}A_2^* \tag{B-5}$$

Keep in mind that A^* is always defined as the sonic throat area; in the supersonic flow ahead of the shock, A_1^* is equal to the actual throat area A_t, because the flow is sonic at A_t, whereas behind the shock A_2^* is the area, the flow behind the shock, would have to be reduced to in order to make it locally sonic. Since the flow behind the shock is always subsonic, then A_2^* never equals the actual physical throat area in the nozzle itself, because the entropy in region 2 is higher than in region 1.

Forming the ratio $P_e A_e/(P_0 A^*)_e$, where $(A^*)_e = A_2^*$, we have

$$\frac{P_e A_e}{P_{0e}\, A_e^*} = \frac{P_e A_e}{P_{02}\, A_2^*} = \frac{P_e A_e}{P_{01} A_1^*} = \frac{P_e}{P_{01}} \frac{A_e}{A_t} \tag{B-6}$$

The terms on the right-hand side are known, because P_e/P_{01} and A_e/A_t are specified.

For the isentropic relations, we can use the relations,

$$\frac{A_e}{A_e^*} = \frac{A_e}{A_2^*} = \frac{1}{M_e}\left[\frac{2}{\gamma+1}\left(1 + \frac{\gamma-1}{2} M_e^2\right)\right]^{(\gamma+1)/(2\gamma-2)} \tag{B-7}$$

and

$$\frac{P_e}{P_{0e}} = \frac{P_e}{P_{02}} = \left(1 + \frac{\gamma-1}{2} M_e^2\right)^{-\gamma/(\gamma-1)} \tag{B-8}$$

By substituting into Eq. (B-6), we solve for M_e. Then, we use the resulting value to solve for P_{02}. Using the value for P_{02}, we form the total pressure ratio across the normal shock. Which is only a function of M_1 in front of the shock, given by (see Appendix A),

$$\frac{P_{02}}{P_{01}} = \left[\frac{(\gamma+1)M_1^2}{(\gamma-1)M_1^2+2}\right]^{\frac{\gamma}{\gamma-1}} \left[\frac{(\gamma+1)}{2\gamma M_1^2-(\gamma-1)}\right]^{\frac{1}{\gamma-1}} \tag{B-9}$$

Then, solving for M_1 we can then get the area section, in somewhat the location, of the shock $A_1(x)$ using area section ratio.

$$\frac{A_1(x)}{A_{t1}} = \frac{1}{M_1}\left[\frac{2}{\gamma+1}\left(1 + \frac{\gamma-1}{2} M_1^2\right)\right]^{(\gamma+1)/(2\gamma-2)} \tag{B-10}$$

All other flow parameters can thus be calculated using isentropic relations in each of the respective regions.

For performance calculations, the same can be said as before, while the thrust is given by,

$$F = \dot{m}\, V_e \tag{B-11}$$

The results of the calculations will be reported at the end.

Free Interaction Theory Application

By combining the 1D ideal theory with the analytical formula of the skin friction coefficient presented in Chapter 4, the practical method for calculating thrust with separation criteria is summarized as follows.

After determining the isentropic nozzle law $P(x)/P_0$ of the adapted nozzle:

1- For a given value of P_a. Find on $P(x)$, the point I such that the free interaction separation criterion (Eqs. (2-14) or (2-18)) applied at this point results in a pressure jump $P_a - P_I$;
2- determine P_{IE} using the Campbell-Farley correlation. To consider the effects of the separated region while in the absence of any completely satisfactory theory, CAMPBELL et FARLEY [7] have established an empirical relation that estimates the average pressure $\overline{P_{IE}}$ in the recovered region, this takes the form:

$$1 - \frac{\overline{P_{EI}}}{P_a}\cos\left(\frac{\theta}{2}\right) = f\left(\frac{P_a}{P_0} \cdot \frac{A_E - A_I}{A^*}\right) \tag{B-12}$$

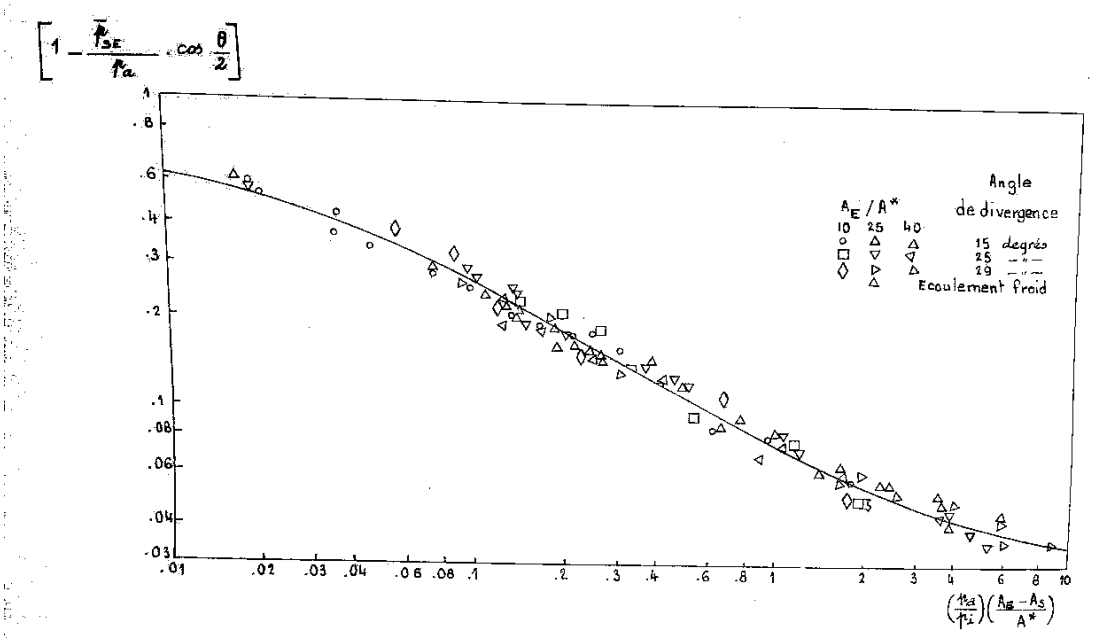

Figure B. 2 : Campbell-Farley correlation function [7].

Where $\overline{P_{IE}}$ is a pressure such that,

$$\overline{P_{IE}} \cdot (A_E - A_I)$$

Become the thrust of the separated region (EI);

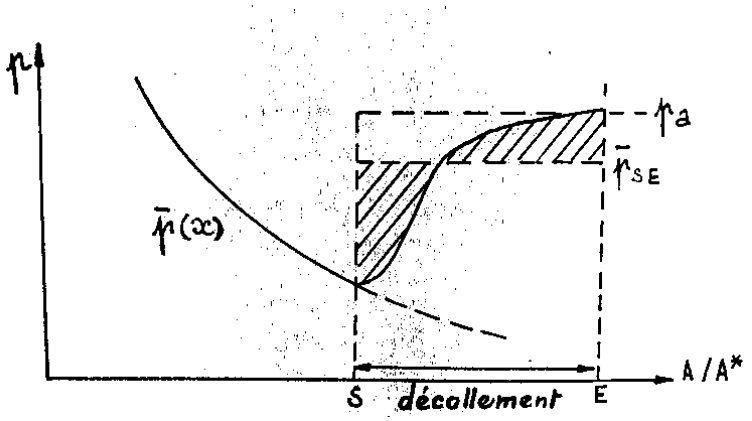

3- Calculate the thrust F up to the separation point using the general method $F_I = \dot{m}\, V_I + (P_I - P_E)\, A_I$;
4- The total thrust is then: $F = F_I + P_{IE}\,(A_E - A_I)$.

All other performance calculations remain the same. It is noted that the estimated pressure jump predicted using the separation criteria should be compared with the pressure jump that would operate from a normal shock wave standing at the separation position. If this last pressure is less than the other, it does mean that separation will not occur and the flow will follow the normal shock wave solution.

Subsonic Calculations

The exact analytical solution of the purely subsonic flow case proceeds as follows. The exit-to-reservoir pressure ratio must be specified; that is, P_e/P_0 is given. Since the total pressure is constant through the nozzle, the value of P_0/P_e defines M_e through Eqs. (1-18), i.e.,

$$\frac{P_0}{P_e} = \left(1 + \frac{\gamma-1}{2}\, M_e^2\right)^{\frac{\gamma}{\gamma-1}} \tag{B-13}$$

Once M_e is known from the solution of Eq. (B-13), the value of A^* can be calculated from Eq. (1.22) as

$$\frac{A_e}{A^*} = \frac{1}{M_e^2}\left[\frac{2}{\gamma+1}\left(1 + \frac{\gamma-1}{2} M_e^2\right)\right]^{(\gamma+1)/(2\gamma-2)} \tag{B-14}$$

where A^* is simply a reference value in this case; A^* is smaller than the throat area A_t,. In turn, with A^* known, the local area divided by A^*, namely, A/A^*, determines the local Mach number M via Eq. (1-22). Finally, this local value of M determines the local values of P_0/P, ρ_0/ρ, and T_0/T from Eqs. (1-18).

For performance, the thrust is given by Eq. (B-11), and the other metrics remain the same.

Results and Analysis

The solutions for different values of $n = P_a/P_e$ or NPR, hence ambient pressure, is studied in the operating conditions of the experimental nozzle. Where performance calculations from the different theories listed above are reported and examined as follows.

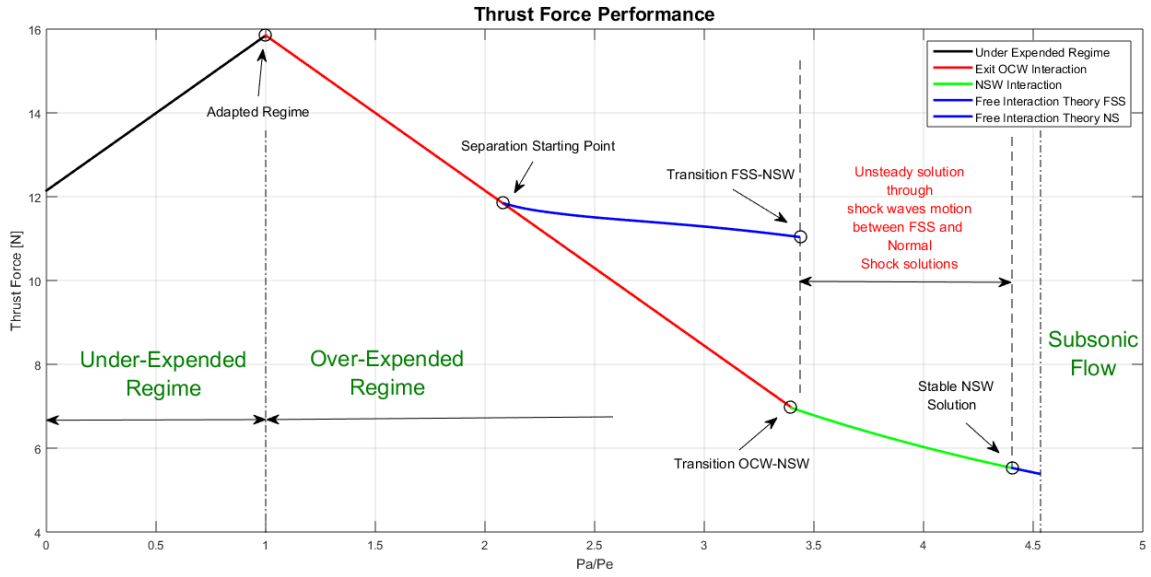

Figure B.3 : Theorical analysis result on thrust force performance of the experimental nozzle.

In Figure B.3, we can see the results for theoretical calculations of nozzle thrust performance. Different regions can be distinguished, from the solution of under-expanded regime, through adapted, and over-expanded regime. While the right portion of the solution defines a subsonic nozzle flow.

In an over-expended regime, the solutions of both ideal unidimensional theory and free interaction theory (FIT) are shown. It has been noted that, for the FIT, it exists a bounded region between $3.44 < P_a/P_e < 4.404$ where the theory doesn't give a coherent solution. It is believed that, it marks the region of an unsteady wave motion as defined in the last section of chapter 2 (Sec. 2.5).

Figure B.4 : Normal shock/Separation position analysis.

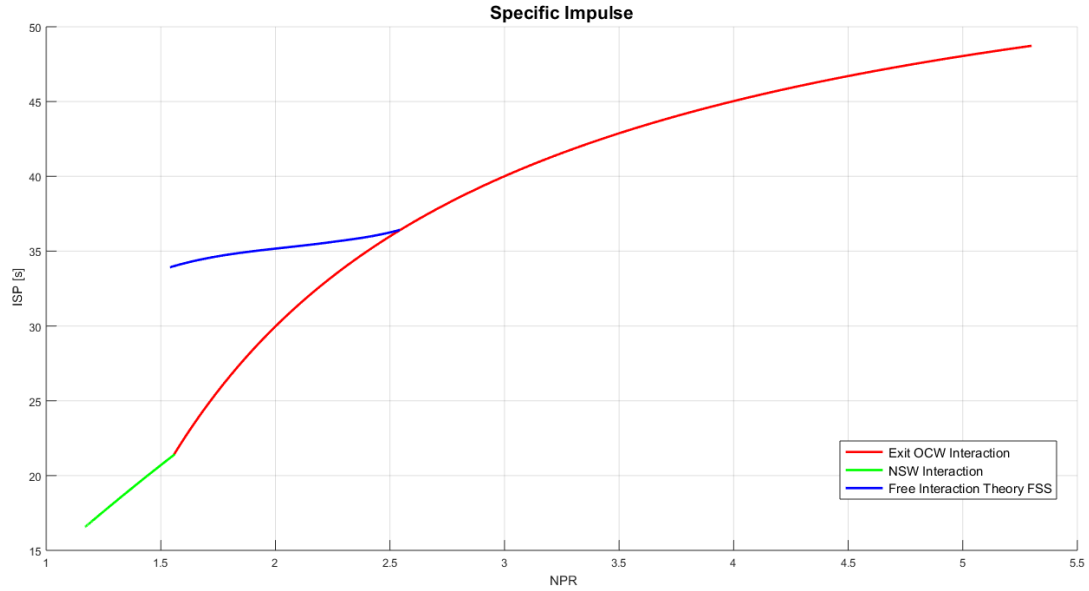

Figure B.5 : Specific impulse analysis results.

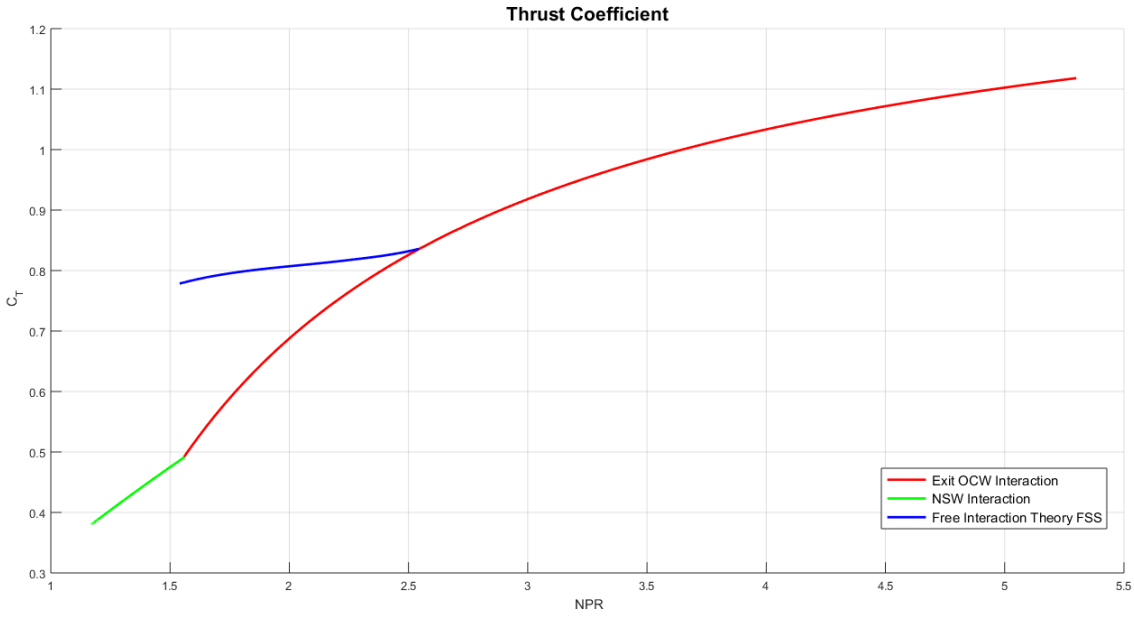

Figure B.6 : Thrust coefficient analysis results.

REFERENCES

[1] J. G. Leishman, “History of Rockets & Space Flight,” eaglepubs.erau.edu, vol. 3, Jan. 2023, doi: https://doi.org/10.15394/eaglepub.2022.1066.n3a.

[2] George Paul Sutton and O. Biblarz, Rocket propulsion elements : an introduction to the engineering of rockets. New York: John Wiley & Sons, 2000.

[3] M. Almqvist, “Semi-Empirical Model for Supersonic Flow Separation in Rocket Nozzles,” Master Thesis, Luleå University of Technology, 2005.

[4] W. Hamaidia, “CONCEPTION A HAUTE TEMPERATURE DES TUYERES SUPERSONIQUES TYPE ANNULAIRE,” PhD Thesis, University of Blida 1, 2020.

[5] John David Anderson, Modern compressible flow with historical perspective. Boston Mcgraw-Hill, 2003.

[6] A. H. SHAPIRO, THE DYNAMICS AND THERMODYNAMICS OF COMPRESSIBLE FLUID FLOW. 1954.

[7] P. CARRIERE, Aerodynamique Interne: Tyere et Jet, Toulouse: Ecole Nationale Superieure de L'Aeronautique et de L'Espace, 1980.

[8] G. Hagemann, H. Immich, T. Van Nguyen, and G. E. Dumnov, “Advanced Rocket Nozzles,” *Journal of Propulsion and Power*, vol. 14, no. 5, pp. 620–634, Sep. 1998, doi: https://doi.org/10.2514/2.5354.

[9] A. BOURGOING, “INSTATIONNARITE ET DISSYMETRIE D’UN ECOULEMENT SUPERSONIQUE DECOLLE DANS UNE TUYERE PLANE,” PhD Thesis, University of Paris 6, 2002.

[10] Compressible Flow, 2025. https://compflow.onlineflowcalculator.com/Anderson/Chapter5/print/, (accessed Jun. 15, 2025).

[11] S. D. Heister, W. E. Anderson, T. L. Pourpoint, and R. J. Cassady, Rocket Propulsion. Cambridge: Cambridge University Press, 2019.

[12] “Resources | Aerodynamics for Students,” *Aerodynamics4students.com*, 2025. https://aerodynamics4students.com/gas-dynamics-and-supersonic-flow/, (accessed Jun. 15, 2025).

[13] Östlund J and Muhammad-Klingmann B, “Supersonic Flow Separation with application to Rocket Engine Nozzles”, Applied Mechanics, Vol 58, 2005.

[14] Malina FJ (1940), Characteristics of the rocket motor based on the theory of perfect gases, Volume 230, J. Frankling Inst., 433-454.

[15] Ahlberg J H, Hamilton S Migdal D and Nilson E N (1961), Truncated perfect nozzles in optimum nozzle design, ARS Journal, 31(5), 614-620.

[16] Rao G V R (1958), Exhaust nozzle contour for optimum thrust, Jet Propulsion, 28(6), 377-382.

[17] Schmucker, R., ‘‘Flow Processes in Overexpanding Nozzles of Chemical Rocket Engines,’’ Technical Univ., TB-7,-10,-14, Munich, Germany, 1973 (in German).

[18] Moelder, A., Gluamhussein, A., Timofeev, E., and Voinovich, P., 1997, ‘‘Focusing of Conical Shocks at the Centreline of Symmetry,’’ Proc. of 21st International Symposium on Shock Waves, Panther Publishing and Printing, Canberra, Paper No. 5601.

[19] Frey, M., Hagemann, G. Status of flow separation prediction in rocket nozzles. 34th AIAA/ASME/SAE/ASEE, Joint Propulsion Conference & Exhibit (July 13-15, 1998, Cleveland, OH), AIAA Paper 98-3619.

[20] P. REIJASSE, “Aérodynamique des tuyères propulsives en sur-détente: décollement libre et charges latérales en régime stabilisé,” PhD Thesis, University of Paris VI, 2005.

[21] A. FERRI, Review of problems in application of supersonic combustion Jour. Roy. Soc. n°68 - pp.575 to 597 - (Sep 1964).

[22] Zukoski, E. E., 1967, ‘‘Turbulent Boundary Layer Separation in Front of a Forward Facing Step,’’ AIAA J., 5(1), pp. 1746–1753.

[23] Johnson, C., and Bushnell, D., 1970, ‘‘Power-Law Velocity Profile-Exponent Variation With Reynolds Number, Wall Cooling, and Mach Number in a Turbulent Boundary Layer,’’ NASA TN D-5753, National Aeronautics and Space Administration, Langley Research Center, Hampton, VA.

[24] Spaid, F., and Frishett, J., 1972, ‘‘Incipient Separation of a Supersonic, Turbulent Boundary Layer, Including Effects of Heat Transfer,’’ AIAA J., 10(7), pp. 915–922.

[25] Herbert, M. V., Herd, R. J. Boundary-layer separation in supersonic propelling nozzles. A.R.C. Report and Memoranda No. 3421, August, 1964.

[26] Hunter, C.A. Experimental, theoretical, and computational investigation of separated nozzle flows. AIAA 98-3107.

[27] D. CHAPMAN, D. KUEHN, H.LARSON, Investigations on separated flows in supersonic and subsonic streams with emphasis on the effect of transition. NACA rep. 1356 (1958).

[28] Erdos, J., and Pallone, A., 1962, ‘‘Shock-Boundary Layer Interaction and Flow Separation,’’ Heat Transfer and Fluid Mechanics Institute Procs., Stanford University Press, Stanford.

[29] P. CARRIERE, Méthode théoriques d’étude des écoulements supersoniques. P.S.T du Ministère de l’Air n° 339 a.

[30] Nave, L. H., and Coffey, G. A., 1973, ‘‘Sea-Level Side-Loads in High Area Ratio Rocket Engines,’’ 9th Propulsion Conference, AIAA Paper No. 73-1284.

[31] M. ARENS and E. SPIEGLER, “SHOCK-INDUCED BOUNDARY LAYER SEPARATION IN OVER-EXPANDED CONICAL EXHAUST NOZZLES,” *AIAA Journal*, vol. 1, no. 3, pp. 578–581, Mar. 1963, doi: https://doi.org/10.2514/3.1598.

[32] Serrin, J.: Mathematical principles of classical fluid mechanics. In: Flügge, S. (ed.) Handbuch der Physik,VIII/1, pp. 125–263. Springer, Berlin (1959).

[33] Buresti, G. A note on Stokes’ hypothesis. Acta Mech 226, 3555–3559 (2015).

[34] Stokes G.G.: On the theories of the internal friction of fluids in motion, and of the equilibrium and motion of elastic solids. Trans. Camb. Philos. Soc. 8, 287–319 (1845).

[35] Rosenhead L.: A discussion on the first and second viscosities of fluids. Proc. R. Soc. Lond. A Mat. 226, 1–69 (1954).

[36] Gad-el-Hak M.: Questions in fluid mechanics: Stokes’ hypothesis for a Newtonian, isotropic fluid. J. Fluid Eng. T. ASME 117, 3–5 (1995).

[37] Markham J.J., Beyer R.T., Lindsay R.B.: Absorption of sound in fluids. Rev. Mod. Phys. 23, 353–411 (1951).

[38] Truesdell C.: On the viscosity of fluids according to the kinetic theory. Zeitschrift für Physik 131, 273–289 (1952).

[39] Rajagopal K.R.: A new development and interpretation of the Navier–Stokes fluid which reveals why the “Stokes assumption” is inapt. Int. J. Nonlinear Mech. 50, 141–151 (2013).

[40] Dukhin A.S., Goetz P.J.: Bulk viscosity and compressibility measurement using acoustic spectroscopy. J. Chem. Phys. 130, 124519 (2009).

[41] Buresti G.: Elements of Fluid Dynamics. Imperial College Press, London (2012).

[42] Emanuel G.: Effect of bulk viscosity on a hypersonic boundary layer. Phys. Fluids A-Fluid 4, 491–495 (1992).

[43] Emanuel G., Argrow B.M.: Linear dependence of the bulk viscosity on shock wave thickness. Phys. Fluids 6, 3203–3205 (1994).

[44] NASA Glenn Coefficients for Calculating Thermodynamic Properties of Individual Species.

[45] F.M. White, Viscous Fluid Flow, 3rd ed., McGraw-Hill, 2006.

[46] R. FRIEDRICH, FUNDAMENTALS OF COMPRESSIBLE TURBULENCE. TU München, Germany.

[47] Favre, A.J. The Equations of Compressible Turbulent Gases, Marseille, Franch, Institut de Mecanique Statistique de la Turbulence, 1965.

[48] CFD Online, Favre averaged Navier-Stokes equations.

[49] Sal Rodriguez, Applied Computational Fluid Dynamics and Turbulence Modeling.

[50] David Apsley, Lecture Notes Turbulence Modeling.

[51] Assessment of Closure Coefficients for Compressible- Flow Turbulence Models, NASA Technical Memorandum 103882.

[52] P. Spalart and S. Allmaras. "A one-equation turbulence model for aerodynamic flows". Technical Report AIAA-92-0439. American Institute of Aeronautics and Astronautics. 1992.

[53] *FLUENT 24 theory's guide.* Fluent Inc, 2024.

[54] D. C.Wilcox. Turbulence Modeling for CFD. DCW Industries, Inc. La Canada, California. 1998.

[55] F. R. Menter. "Review of the SST Turbulence Model Experience from an Industrial Perspective". International Journal of Computational Fluid Dynamics. Volume 23, Issue 4. 2009.

[56] D. C.Wilcox. "Formulation of the k–ω turbulence model revisited". 45th AIAA Aerospace Sciences Meeting. Reno, NV, USA. AIAA Paper 2007–1408. 2007.

[57] F. R. Menter. "Two-Equation Eddy-Viscosity Turbulence Models for Engineering Applications". AIAA Journal. 32(8). 1598–1605. August 1994.

[58] *FLUENT 24 user's guide.* Fluent Inc, 2024.

[59] L. J. Dechant and M. J. Tattar, "Analytical skin friction and heat transfer formula for compressible internal flows," Jan. 1994.

[60] iChrome, "Turbulence Calculator," *iChrome*, Jul. 20, 2016. http://ichrome.com/blogs/archives/342

[61] J. D. Anderson, *Computational fluid dynamics: the basics with applications*. New York: Mcgraw-Hill, 2006.